# Development of pulsed multipole magnet for beam injection in light source

*Author:*
Yao Lu

*Supervisor:*
Assoc.Prof. Mitsuda Chikaori

Doctor of Philosophy

Department of Accelerator Science
School of High Energy Accelerator Science
The Graduate University for Advanced Studies, SOKENDAI

September 2022

SOKENDAI

# Declaration of Authorship

I, Yao Lu, declare that this thesis titled, 'Development of pulsed multipole magnet for beam injection in light source' and the work presented in it are my own. I confirm that:

- This work was done wholly or mainly while in candidature for a research degree at this University.
- Where any part of this thesis has previously been submitted for a degree or any other qualification at this University or any other institution, this has been clearly stated.
- Where I have consulted the published work of others, this is always clearly attributed.
- Where I have quoted from the work of others, the source is always given. With the exception of such quotations, this thesis is entirely my own work.
- I have acknowledged all main sources of help.
- Where the thesis is based on work done by myself jointly with others, I have made clear exactly what was done by others and what I have contributed myself.

Signed: Yao Lu

Date: September 2022

**A dissertation submitted to Department of Accelerator Science,**
**School of High Energy Accelerator Science,**
**The Graduate University for Advanced Studies, SOKENDAI,**
**in partial fulfillment of the requirements for the degree of**
**Doctor of Philosophy**

**Advisory Committee**

| | |
|---|---|
| 1. Prof. MASUZAWA Mika | KEK |
| 2. Prof. MIMASHI Toshihiro | KEK |
| 3. Prof. TAKASHIMA Yoshifumi | Nagoya Univerisity |
| 4. Assoc. Prof. MIYAJIMA Tsukasa | KEK |
| 5. Assoc. Prof. TAKAKI Hiroyuki | KEK |
| 6. Assoc. Prof. MITSUDA Chikaori | KEK |

# *Abstract*

Nowadays, top-up injection has been a standard operation mode in most light sources, which allows a constant current in electron storage ring. The conventional bump injection system cannot suppress the stored beam oscillation completely. To improve the performance of light source, a novel new injection schemes have been proposed, which has a possibility to inject the beam by only one pulsed multipole magnet. The objective of this research was dedicated to studying and developing the pulsed multipole magnet used for beam injection.

KEK-Photon Factory (KEK-PF) first proposed and examined this novel injection scheme. The beam was injected successfully by a Pulsed Sextupole Magnet (PSM). Owning to the nature of the sextupole magnet, the stored beam should be not disturbed because of the nearly zero magnetic field around the center. However, the amplitude of the horizontal stored beam oscillation is 570 µm in the experiment, which is larger than our expectation. This is the starting point of our research to figure out the issue of the stored beam oscillation and develop a new pulsed magnet.

Firstly, a compact pick-up probe has been developed for measuring a pulsed magnetic field with a 3.2 mm × 5.8 mm coil for a magnetic field mapping. It can be used to investigate whether there is an irregular magnetic field at the center and examine the off-axis kick effect of a pulsed multipole magnet. In the PSM measurement, a magnetic field signal with an amplitude of $2.2 \times 10^{-4}$ T was measured clearly by improving the Signal to Noise ratio (S/N) in a high-frequency noise environment, and the longitudinal field structure that contained the magnetic field generated by the eddy current effect was observed, which explains the oscillation of the stored beam in the PSM injection.

Based on the study above, it is concluded that air-core pulsed magnet is a better candidate for the injection in next generation light source. The Ceramics Chamber with integrated Pulsed Magnet (CCiPM) has been developed as a fast air-core dipole kicker. An octupole CCiPM was designed for the beam injection at PF ring. The initial prototype of the CCiPM had a problem about the high inductance (11.15 µH). To solve this issue, a new design was proposed and examined by the simulation. Four conductors were placed on the ceramic chamber. Therefore, the long cable for changing the direction of the current was not used in the new design. Then OPERA was used to evaluate the magnetic field and optimize the busbar structure that can produce undesirable magnetic field at the center. If the current is 3000 A, the integrated magnetic field field at center is less than 10 µT · m and the off-axis ($x$=15 mm) integrated field is 11.1 mT · m in the simulation.

The prototype of the octupole CCiPM was fabricated successfully. The inductance is only 1.45 µH. To examine the mechanical performance, an offline test bench was constructed. A heating-cycle baking was performed to make a severe operation environment that is similar with an accelerator ring. The vacuum was $1.0 \times 10^{-7}$ Pa in the end, and vacuum leakage did not occur. In the current excitation test, the peak current can reach to 2800 A. The DC and pulsed magnetic fields have been measured, and the results are discussed. Finally, the CCiPM was installed in the PF ring. The current operation condition is reported.

# *Acknowledgements*

I would like to express my gratitude to those who encouraged and supported me during my doctoral research.

First and foremost, I want to thank my esteemed supervisor, Dr. Chikaori Mitsuda, who supported and gave me many valuable suggestions in the past three years. Your guidance not only influenced my attitude towards scientific research but also helped me develop a lot of good habits in daily life. I also want to express my great appreciation to my sub-supervisor, Dr. Tsukasa Miyajima, thanks for your encouragement and fruitful advice to me.

I would like to give my wholehearted thanks to many people in Accelerator Division VI. My research work cannot be carried out without your assistance. I am really grateful to Dr. Hiroyuki Takaki, Dr. Takashi Obina, Dr. Yukinori Kobayashi, Dr. Kentaro Harada, Dr. Toru Honda, Mr. Takashi Nogami, and Mr. Takashi Uchiyama. Thanks for making contributions to my research experience, and I learned a lot of things from the communication in the past three years.

I also want to express my sincere gratitude to Dr. Mika Masuzawa and Dr. Etienne Forest for your strong and warm supports.

Many thanks to my friends, Di Wang, Baiting Du, Xiuqing Xu, Yuki Abe, and Kotaro Takahashi, for leaving many good memories and enriching my life in Japan.

Finally, I want to give my thanks to my parents, teachers, and friends in China. Particularly, I must thank Mr. Yu who continuously helps recover my health.

# Contents

# List of Figures

# List of Tables

# Abbreviations

| | |
|---|---|
| **ALS** | Advanced Light Source |
| **APS** | Advanced Photon Source |
| **BESSY** | Berlin Electron Storage Ring Society for Synchrotron Radiation |
| **BPM** | Beam Position Monitor |
| **BT** | Beam Transport |
| **CCiPM** | Ceramics Chamber with integrated Pulsed Magnet |
| **CH** | CHannel |
| **DC** | Direct Current |
| **ELF** | ELectromagnetic Field analysis |
| **ESRF** | European Synchrotron Radiation Facility |
| **GPIB** | General Purpose Interface Bus |
| **GeV** | Giga electron Volt |
| **GUI** | Graphical User Interface |
| **HER** | High Energy Ring |
| **IHEP** | Institute of High Energy Physics |
| **KEK** | High Energy Accelerator Research Organzation |
| **LCR** | inductance (L), capacitance (C), and resistance (R) |
| **LER** | Low Energy Ring |
| **LINAC** | LINear particle ACcelerator |
| **LNLS** | Brazilian Synchrotron Light Laboratory |
| **MBA** | Multi-Bend Achromat |
| **NMR** | Nuclear Magnetic Resonance |
| **PEEK** | PolyEther Ether Ketone |
| **PF** | Photon Factory |
| **PF-AR** | Photon Factory Advanced Ring |

**PMM** Pulsed Multipole Magnet

**PQM** Pulsed Quadrupole Magnet

**PSM** Pulsed Sextupole Magnet

**POM** Pulsed Octupole Magnet

**SAD** Stragetic Accelerator Design

**SLS** Swiss Light Source

**SOLEIL** French National Synchrotron Facility

**S/N** Signal-to-Noise ratio

**UVSOR** Ultraviolet Synchrotron Orbital Radiation Facility

**YAG** Yttrium Aluminum Garnet

# Chapter 1

# Introduction

## 1.1 Top-up Operation in Light Source

Light source is a type of circular particle accelerator in which electrons may be kept circulating. Photons are emitted when the electrons are accelerated radially, which is called synchrotron radiation [1]. It can be produced in a light source by using bending magnets and undulators as shown in Fig. 1.1, which is a powerful tool to probe the nature, required with widely tunable frequency range from infrared to hard X-ray. Because electrons are stored in a closed loop, a light source is also known as a storage ring.

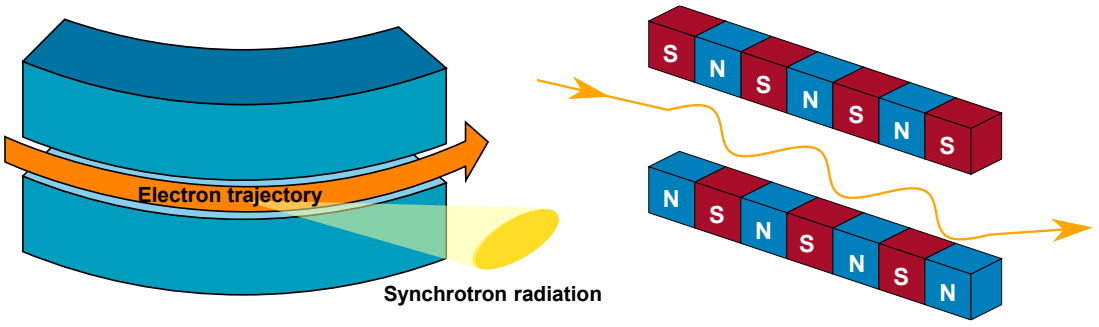


FIGURE 1.1: Synchrotron radiation from bending magnet and undulator.

Consequently, a light source can be considered as a glorious service station to support scientific researches like physics, chemistry, biology and medical science. Accelerator researchers always aims at improving the performance of light source such as brilliance, spectral range, time structure, and radiation power, which is closely related to the quality of stored beam.

At first, a light source had two separate operation status——injection and storage. Injection status is that an electron beam is injected into the storage ring until its current reaches to a designed value. Then the beam is stored stably and gradually loses as a result of the synchrotron radiation, which is called storage status. When the current is lower than a threshold, the beam is injected again. The number of injection times is usually two or three in one day. Under such an operation mode, users could not perform experiments during injection status. Furthermore, the strength of photon flux is not stable.

Therefore, accelerator researchers tried to optimize the performance of a light source that the current can be stable, and synchrotron radiation experiment can be performed without a break. The basic idea is that after current reaches the designed value, a little bit of electron beam is injected continuously to keep a stable current value. It is so called "top-up operation".

The top-up operation was firstly tested at SORTEC-1 in 1990 [2]. After many years of efforts, APS realized the top-up operation for user experiments in 2001 [3]. Nowadays, top-up operation becomes the standard mode of operation in most light sources [4]. In top-up operation, the light source can nearly keep a constant beam current to overcome beam lifetime limitations and provide a constant photon flux that can achieve a thermal equilibrium at the beamline. Users do not need to stop experiments because of the refilling of beam. But frequent injection brings new problems that will be explained in next section.

## 1.2 Conventional Bump Injection System

Up to now, pulsed bump injection system is widely used in existing electron storage rings. A local orbit bump is generated around injection point by several dipole kickers. The system usually consists of two, three, or four kickers. Fig. 1.2 shows a schematic view

of a most general four bump kickers injection system that can adjust orbit displacement and angle easily. The stored beam orbit can be bumped to a desired transverse position that is near to the injection beam from the septum magnet. Because of being kicked by K3 and K4, the injection beam will have a small betatron oscillation around the stored beam orbit and finally merge with the stored beam due to damping of the injection oscillation. The bump injection is an off-axis injection system that the stored beam and injection beam keep circulating within the aperture of a ring.

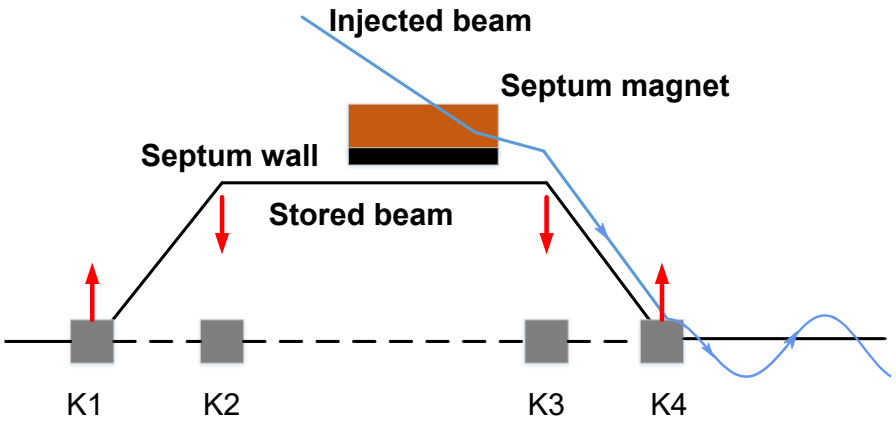


FIGURE 1.2: Schematic view of a bump injection system.

In an ideal and linear dynamic case, a bump orbit is closed to each stored bunch so that stored beam oscillation does not appear [5]. However, non-linearity of sextupole magnetic field exists in bump orbit, which has possibility to cause perturbation on stored bunch. Moreover, some hardware issues such as magnetic field errors, non-similarity of pulse shape of four kickers, and leakage field of septum will also have a negative impact on the bump orbit, which induce stored beam oscillation. The excited oscillation effectively enlarges emittance of stored beam and modulates photon flux intensity.

To reduce stored beam oscillation in bump injection, the injection system is contentiously being upgraded in many aspects such as optimization on strength of sextupole magnet [6], improvement of pulsed power source [7], and application of an counter kicker to suppress oscillation [8, 9]. However, after many years of efforts in different facilities, perturbation on stored bunch centroid is still way above 10% beam size [10].

## 1.3 New Injection Proposals for Next Generation light source

It is known that brilliance is an important parameter of a light source. To increase brilliance, a much smaller beam emittance is required. In next generation light sources, Multi-Bend Achromat (MBA) lattice is usually applied to achieve tiny beam emittance [11]. Because of the lattice characteristics, dynamic aperture becomes narrow and free space of straight section is sometimes limited, which raise difficulty for a bump injection. Sometimes bump injection system is even impossible to be constructed in a ring. Besides the beam size becomes much smaller. Users might be more sensitive to the stored beam oscillation. Thus, a new injection system that is superior to bump injection is desired for next generation light source.

Now there are mainly two potentially new injection schemes based on ultra-fast stripline kickers and a pulsed multipole magnet. Theoretically, they both have possibilities to realize a transparent injection that stored beam is not disturbed during injection. The basic concepts are explained in this section.

Generally, a stripline kicker can generate a ultra-short pulse voltage signal that is only several nanoseconds [12]. If the pulse width is shorter than the gap of timing between two bunches in the stored bunch train, the stored beam will no be disturbed. The injection beam is kicked by electric field rather than magnetic field. The schematic view of injection by stripline kicker is shown in Fig. 1.3.

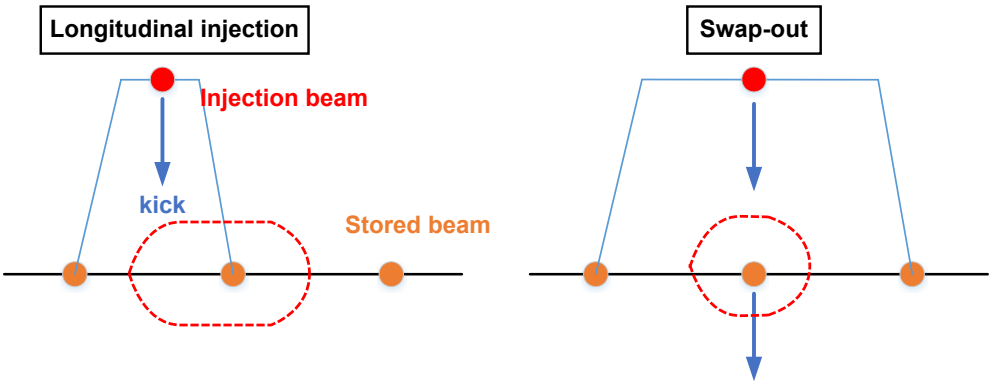


FIGURE 1.3: Schematic view of injection by stripline kicker.

Rigorously, there are two conditions when injection beam is kicked by stripline kicker. One is that the injection beam is kicked into the gap between two stored bunches and

performs synchrotron oscillation. The red dash line means the separatrix of longitudinal acceptance. Then the injection beam merges with one stored bunch due to damping. In this case, the stored beam is not disturbed, which is called "longitudinal injection". However, if the longitudinal aperture of the ring is too narrow, which is too severe to generate a short pulse by a stripline kicker, the injection beam must be kicked to replace one stored bunch that is extracted after the injection. This type belongs to "swap-out injection".

The injection by stripline kicker is an on-axis injection system that allows a much smaller dynamic aperture and is compatible with different gaps of insertion devices. But due to the weak kick strength, the number of kicker is often more than one. The total length of the kicker is usually about 3 m from some available designs [13–15].

As for the injection by a pulsed multipole magnet, the magnet is often installed at downstream of injection point. The installation position needs careful physics considerations. For simplicity, injection beam is regarded as a single particle because it is far from closed orbit of ring. After entering the ring, injection beam experiences a betatron oscillation. The transverse motion of injection beam can be analyzed in a normalized phase plane. The action variable is assumed to be constant, and the phase gradually increases during the propagation of injection beam, which is shown in Fig. 1.4 [5]. When the beam comes to the pulsed multipole magnet, it will experience a kick to reduce the oscillation amplitude. Fig. 1.5 shows a schematic view of the injection beam trajectory. Finally, the injection beam keeps circulating and can be stored in the ring. This is the basic mechanism of Pulsed Multipole Magnet (PMM) injection.

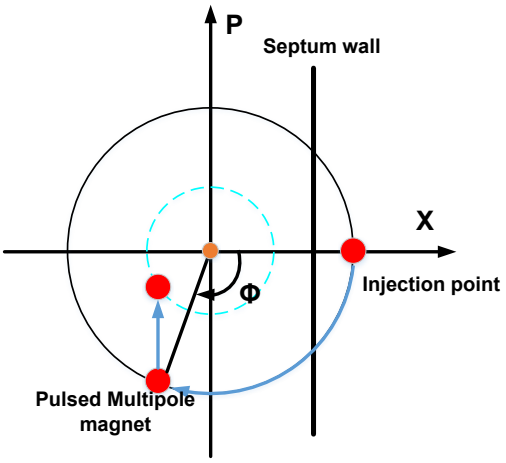


FIGURE 1.4: Transverse injection beam motion in a normalized phase plane.

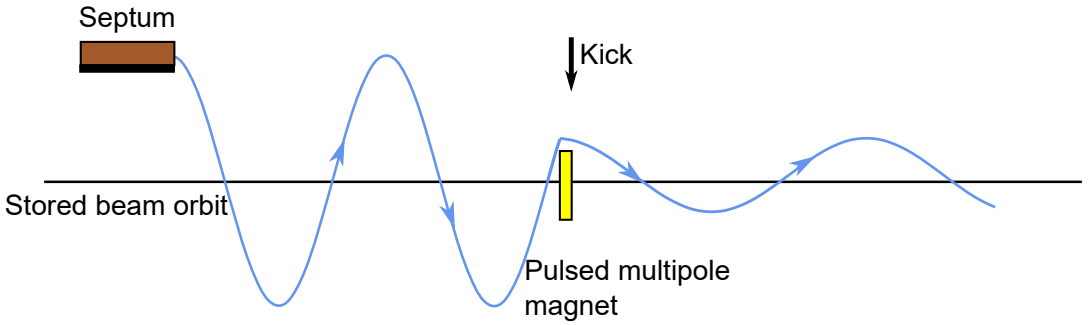


FIGURE 1.5: Trajectory of the beam injected by one pulsed multipole magnet.

Pulsed multipole magnet can provide a nonlinear distribution of magnetic fields which has a maximum value off axis where the injection beam arrives and an nearly zero value around the center where the stored beam passes. Therefore, the oscillation of the stored beam is expected to be negligible. One magnet is usually enough to perform the injection. Hence, the system can be very compact and be controlled easily.

According to the description above, each scheme has its own advantages and disadvantages. The injection by stripline kickers is not limited by the dynamic aperture but needs long straight section. In PMM injection, there is only one magnet so that free space is not a problem in the design of a ring. However, it requires a relatively large horizontal dynamic aperture. Owing to the nature of multipole magnet, the position where the injection beam is kicked cannot be close to the center. Otherwise, the magnet cannot provide enough kick effect because the off-axis magnetic field is weak. The

application of these new schemes needs not only continuous development of hardware but also delicate physics design of the ring.

In this thesis, the research work is about PMM injection, which is mainly based on the previous researches at KEK-PF. Several tests of PMM injection were performed with different pulsed multipole magnets. Some achievements were obtained such as a successful beam injection and top-up operation. However, the perturbation on stored beam is an unknown issue in experiments. In a recent experiment by a pulsed sextupole magnet, the stored beam oscillation reached 4 mm. Detailed contents are shown in next Chapter.

# Chapter 2

# Overview of Pulsed Multipole Magnet Injection

The PMM injection was firstly proposed and tested at KEK-PF. This chapter mainly focuses on achievements and remaining issues in PMM injection experiments at KEK-PF. Additionally, experiment results in other facilities are also introduced. Based on the information and a preliminary analysis of skin depth, it is supposed that eddy current effects were present in the past experiments.

## 2.1 Magnetic Field of Accelerator Magnets

Before introducing the research about PMM injection, it is necessary to give the magnetic field equations of accelerator magnets. It is assumed that the designed orbit of stored beam is a circle. Therefore, the physics parameters are discussed in a curvilinear coordinate, which is shown in Fig. 2.1. $r_0$ is the radius of curvature.

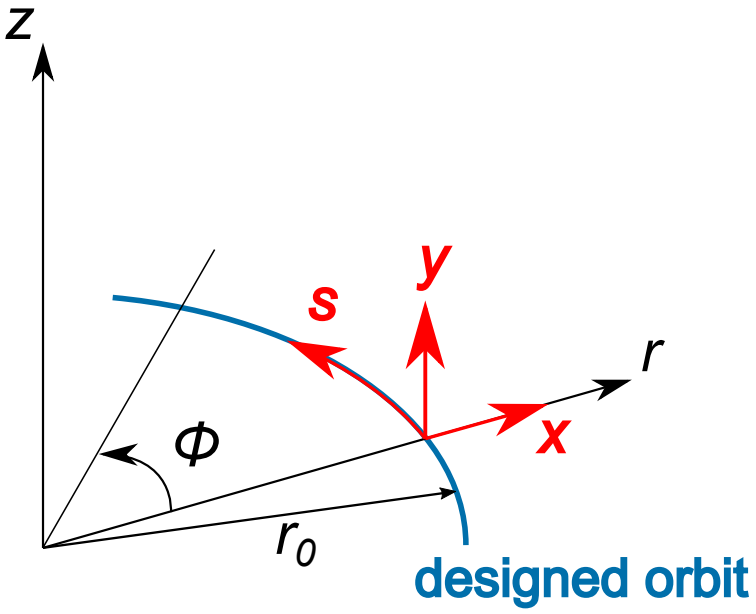


FIGURE 2.1: Coordinate system of electron particle in a ring.

Two useful formulas in a curvilinear coordinate are as follows:

$$\nabla A = \frac{\partial A}{\partial r}\vec{e_r} + \frac{1}{r}\frac{\partial A}{\partial \phi}\vec{e_\phi} + \frac{\partial A}{\partial z}\vec{e_z} \tag{2.1}$$

$$\nabla \cdot \boldsymbol{A} = \frac{1}{r}\frac{\partial r A_r}{\partial r} + \frac{1}{r}\frac{\partial A_\phi}{\partial \phi} + \frac{\partial A_z}{\partial z} \tag{2.2}$$

Because the variable $(x, y, s)$ in a local coordinate is very convenient to describe the particle motion in a ring. Some parameters are defined as

$$\begin{aligned} h &= \frac{1}{r_0} \\ hs &= \phi \\ 1 + hx &= hr \end{aligned} \tag{2.3}$$

Then the gradient and divergence are rewritten as

$$\nabla A = \frac{\partial A}{\partial x}\vec{e_x} + \frac{1}{1+hx}\frac{\partial A}{\partial s}\vec{e_s} + \frac{\partial A}{\partial y}\vec{e_y} \tag{2.4}$$

$$\nabla \cdot \boldsymbol{A} = \frac{1}{1+hx}\frac{\partial (1+hx)A_x}{\partial x} + \frac{1}{1+hx}\frac{\partial A_s}{\partial s} + \frac{\partial A_y}{\partial y} \tag{2.5}$$

Charge and current are not present in the pipe of ring. From Maxwell's equations, the magnetic field satisfies:

$$\nabla \cdot \boldsymbol{B} = 0 \tag{2.6}$$

And the magnetic scalar potential $V$ is given by

$$\nabla \cdot (-\nabla V) = 0 \tag{2.7}$$

According to Eq. 2.4 and Eq. 2.5, Eq. 2.7 becomes

$$\frac{\partial^2 V}{\partial x^2} + \frac{h}{1+hx}\frac{\partial V}{\partial x} + \frac{1}{(1+hx)^2}\frac{\partial^2 V}{\partial s^2} + \frac{\partial^2 V}{\partial y^2} = 0 \tag{2.8}$$

Fringe field is neglected here, and only transverse field is taken into consideration, the scalar potential $V$ should obey

$$\left\{\frac{\partial^2}{\partial x^2} + \frac{\partial^2}{\partial y^2} + \frac{h}{1+hx}\frac{\partial}{\partial x}\right\} V = 0 \tag{2.9}$$

For a large accelerator ring like the PF ring whose circumference is 187 m, the radius of curvature is big so that $h$ is ignored. Then the solution is

$$\begin{aligned} V &= Real\left\{\sum_{n=1}^{\infty}\frac{(-a_n + ib_n)}{n}(x+iy)^n\right\} \\ &= -\frac{a_n}{n}Real\{(x+iy)^n\} - \frac{b_n}{n}Imag\{(x+iy)^n\} \end{aligned} \tag{2.10}$$

The components of $\boldsymbol{B}$ are calculated as

$$B_x = -\frac{\partial V}{\partial x} \qquad B_y = -\frac{\partial V}{\partial y} \tag{2.11}$$

Then the magnetic field in the midplane ($y = 0$) is given by:

$$B_x = \sum_{n=1}^{\infty} a_n x^{n-1} \qquad B_y = \sum_{n=1}^{\infty} b_n x^{n-1} \tag{2.12}$$

where $b_n$, $a_n$ are called $2n$th multipole coefficients with normal dipole $b_1$, skew dipole $a_1$, normal quadrupole $b_2$, skew quadrupole $a_2$, normal sextupole $b_3$, skew sextupole $a_3$, etc.

In a ring, most magnets are normal type. Electrons mainly experience magnetic field

in the midplane and perform betatron oscillation. According to Eq. 2.12, $B_y$ in the midplane is a line distribution for a normal quadrupole magnet, and it is a parabolic distribution for a normal sextupole magnet.

## 2.2 PMM Injection at KEK-PF

The layout of accelerator complex in KEK Tsukuba campus is shown in Fig. 2.2. PF operates two storage rings: the 2.5 GeV PF ring and 6.5 GeV PF Advanced Ring (PF-AR) [16]. Several PMM injections were conducted by different pulsed magnet in these two storage rings. The detailed information is summarized in this section.

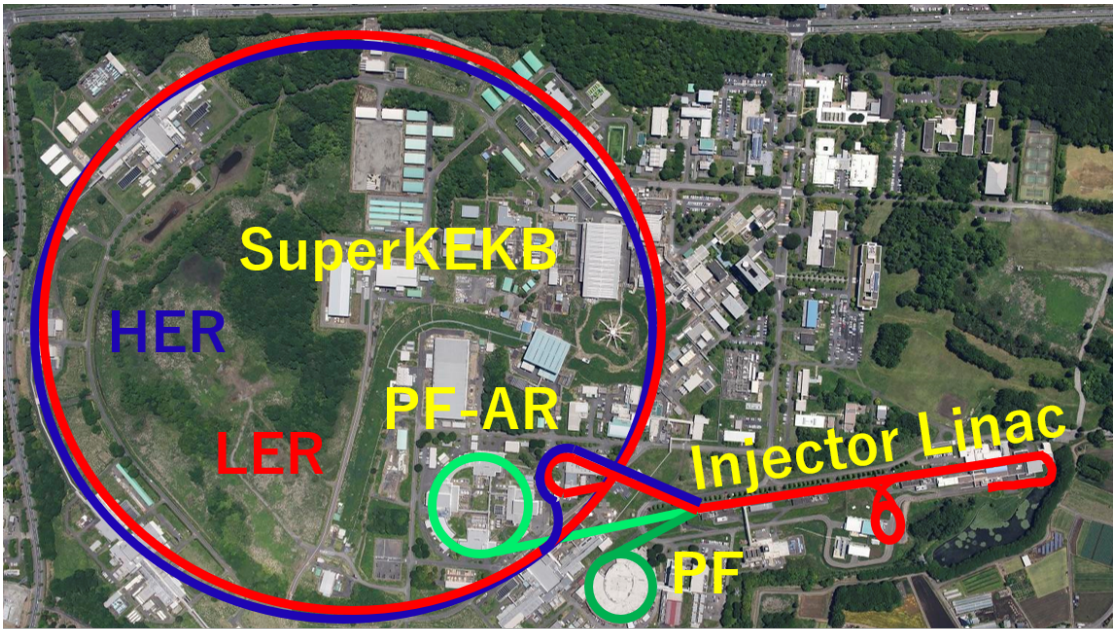


FIGURE 2.2: Accelerator complex in KEK Tsukuba campus.

TABLE 2.1: Main parameters of PF-ring and PF-AR.

| Parameter | PF ring | PF-AR |
|---|---|---|
| Energy[GeV] | 2.5 | 6.5 or 5 |
| Circumference[m] | 187 | 377 |
| Current[mA] | 450 | 50 |
| Emittance[nm · rad] | 35 | 293 |
| Beam lifetime[h] | 22 | 22 |

### 2.2.1 Pulsed Quadrupole Magnet Injection

The first PMM injection is demonstrated by a Pulsed Quadrupole Magnet(PQM) injection at PF-AR [17]. PF-AR is a unique synchrotron radiation light source dedicated to single-bunch operation for a pulsed X-ray. The PQM was installed at the downstream of the injection point, which is close to the septum magnet. The beam was injected successfully, which proved the feasibility of PMM injection.

The comparison of the beam profiles between the bump and PQM injection is shown in Fig. 2.3. The oscillation of the stored beam's centroid is greatly reduced in PQM injection. However, there is a beam size oscillation problem in PQM injection. As shown in Fig. 2.3, the beam size changes turn by turn after being kicked by the PQM. Hence the PQM injection was not used for top-up operation. More efforts are required in PMM injection.

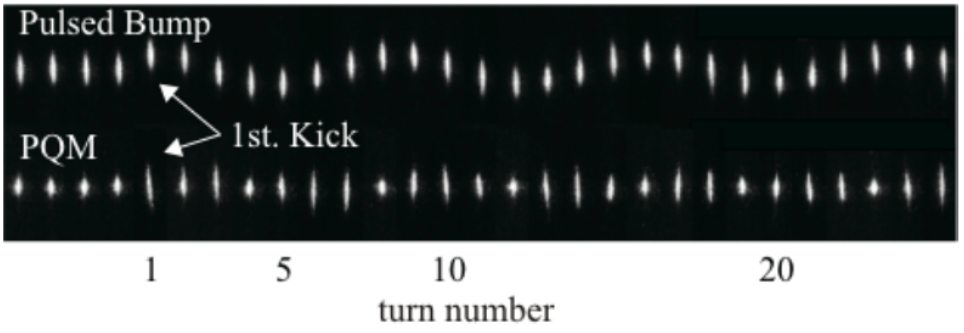


FIGURE 2.3: Comparison of the beam profiles between different injections at PF-AR.

The reason of the beam size oscillation is that the PQM that cannot provide a nearly zero magnetic field at the center. Therefore, the stored beam suffered a perturbation that modulated the beam size.

### 2.2.2 Pulsed Sextupole Magnet Injection

To solve the beam size oscillation problem, a Pulsed Sextupole Magnet (PSM) was proposed to replace the PQM. It is evident that magnetic field around center of PSM is smaller than that of PQM if they have a same off-axis magnetic field. A schematic view is shown in Fig. 2.4.

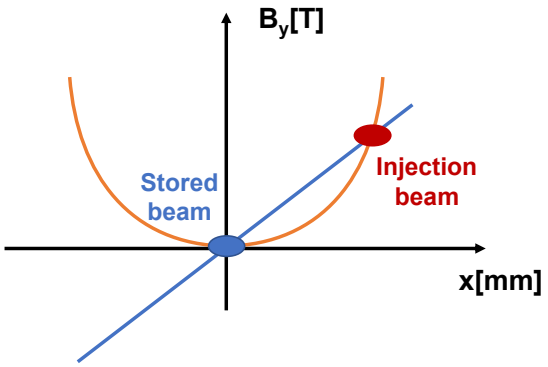


FIGURE 2.4: Horizontal magnetic field distribution of PQM and PSM in the midplane.

The PSM injection was performed at the PF ring [18]. The layout of the injection part is shown in Fig. 2.5. The PSM is located at the downstream of Undulator02 by a careful physical design. According to the design of the PSM injection [19], the injection beam from the LINAC experiences a large betatron oscillation. When it arrives at the entrance of the PSM, the injection beam is kicked by the PSM, and the betatron oscillation amplitude is much reduced. Owing to damping, the beam is stored in the ring finally.

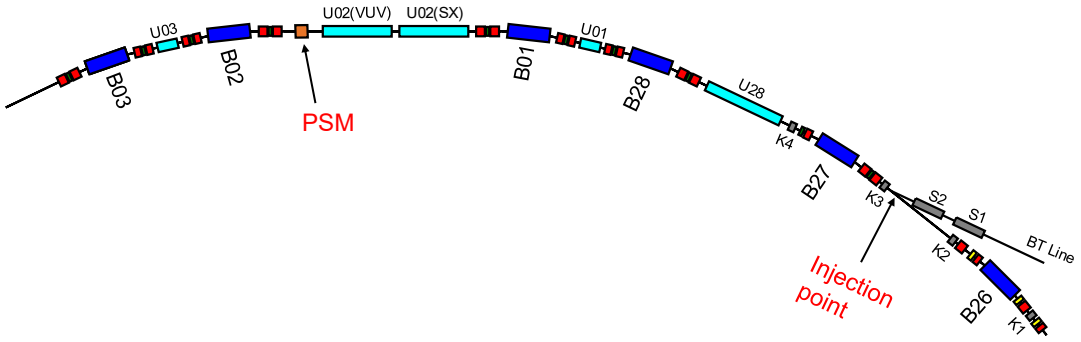


FIGURE 2.5: Layout of the injection part at the PF ring.

The initial design of the PSM is a sextupole magnet with a circular aperture. The cross-sectional view of the PSM with magnetic flux is shown in Fig. 2.6. The diameter of the aperture is 66 mm.

The first PSM injection was conducted in 2008. The beam was also injected successfully. A smaller horizontal stored beam oscillation was observed, which is 180 µm in contrast to a 850 µm amplitude oscillation in the bump injection. The stored beam profiles in the PSM injection are shown in Fig. 2.7. The problem of the beam size oscillation was released as expected.

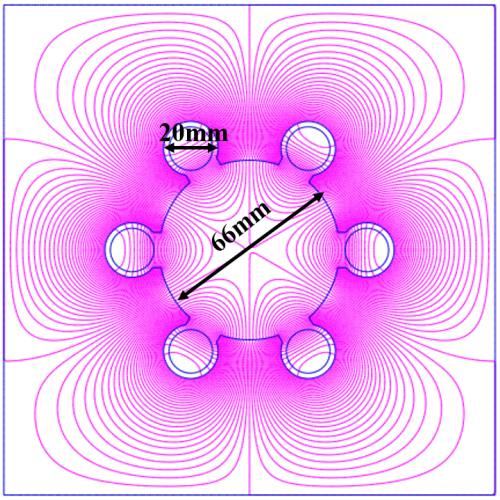


FIGURE 2.6: Cross-sectional view of the initial PSM with magnetic flux.

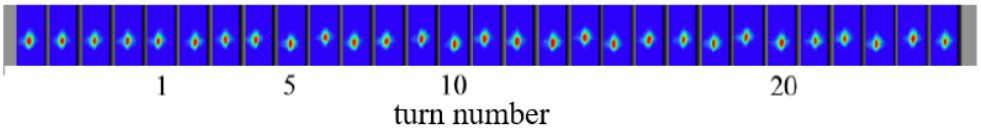


FIGURE 2.7: Beam profiles in the first PSM injection at the PF ring.

Because of the good stored beam property, the PSM injection was operated in top-up mode at PF ring. It demonstrated that a long and stable operation was achieved by PMM injection. However, the injection efficiency is only about 40%, which is a main problem in the experiment. It is noted that the injection in 2008 is a two-turn kick injection. After upgrading the power source to perform a one-turn kick injection, the horizontal oscillation amplitude became 570 µm

The narrow horizontal aperture of PSM is a possible reason that limits the injection efficiency. To increase the injection efficiency, a new PSM with a larger horizontal aperture was made to replace the initial PSM. The cross-sectional view of the upgraded PSM with magnetic flux is shown in Fig. 2.8. For simplicity, the initial PSM is named PSM1, and the upgraded one is named PSM2.

The magnetic field property of PSM2 is almost similar with that of PSM1. The main difference is the aperture shape. The aperture shape of PSM2 is rectangular, and the width becomes 80 mm.

However, after the installation of PSM2, large stored beam oscillation was observed in

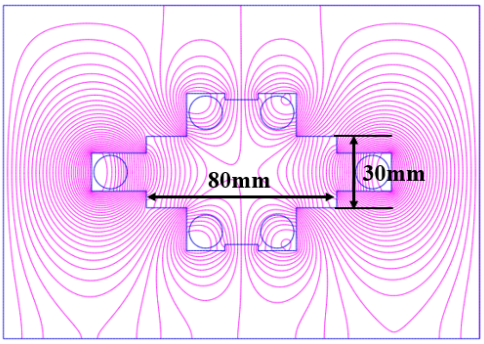


FIGURE 2.8: Cross-sectional view of PSM2 with magnetic flux.

the injection experiment, which had 4 mm amplitude. The BPM data at the downstream of Undulator-2 is shown in Fig. 2.9. It seems that a large perturbation was present in PSM2 injection. The comparison between PSM1 and PSM2 is shown in Table 2.2. More issues need to be investigated in the future.

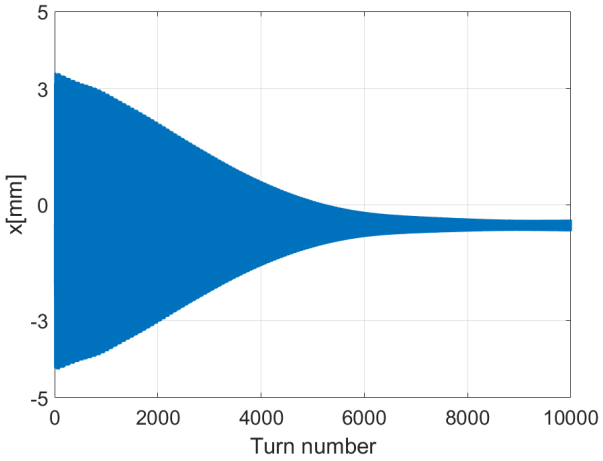


FIGURE 2.9: BPM data of the stored beam centroid in PSM2 injection.

TABLE 2.2: Comparison between PSM1 and PSM2.

| | PSM1 | PSM2 |
|---|---|---|
| Horizontal aperture[mm] | 66 | 80 |
| Magnet length[mm] | 300 | 300 |
| Lamination steel thickness[mm] | 0.15 | 0.15 |
| Designed peak current[A] | 3000 | 2500 |
| Horizontal stored beam oscillation amplitude | 180 µm (2.4µs)<br>570 µm (1.2µs) | 4 mm (1.2µs) |

## 2.3 Researches at Other Facilities

Owing to the successful experiment of PSM1 injection, PMM injection scheme was established and distributed to other facilities. PMM injection schemes were proposed immediately by some facilities such as MAX-IV [20], ESRF [21], LNLS [22], ALS [23], SLS [24], IHEP [25].

In Japan, UVSOR and Aichi Synchrotron Radiation Center also showed interests in PSM injection and made prototypes to perform experiment. Their PSMs are also rectangular shape. In the PSM injection at UVSOR [26], the stored beam oscillation appeared, and the amplitude was about 2 mm at first. Then the magnetic field around the center was compensated by electromagnetic interference sheets to reduce magnetic field distortion, then the oscillation amplitude was reduced less than 200 µm. In the PSM injection at Aichi synchrotron radiation center [27, 28], stored beam oscillation also reached to several millimeters in the PSM injection, but the magnetic field at the center cannot be optimized easily.

In addition, researchers at BESSY II developed an air-core pulsed magnet for PMM injection in 2011 [29]. A nonlinear magnetic field is generated in the midplane of magnet. Thus, the air-core pulsed magnet is named nonlinear kicker. The beam was injected successfully in their experiment and horizontal stored beam oscillation was reduced to 60 µm. The magnet is quite different from PSM or PQM which are iron-core pulsed magnet.

The cross-sectional view of a nonlinear kicker model and the shape of magnetic field in midplane is shown Fig. 2.10. The distribution of conductor is a rectangular shape. The direction of current flow and the aperture of chamber are marked. The basic design of a nonlinear kicker is that vertical aperture should be as small as possible. Then a strong magnetic field can be obtained in the midplane. Because the magnetic field in an air-core magnet only depends on the distance to conductors and strength of current.

The nonlinear kicker model realized a smaller stored beam oscillation (60 µm) compared with the value in the PSM injection at the PF ring. The design is now widely chosen by other facilities like SOLEIL [30], ALS [31], and SIRIUS [32] for development of PMM injection in next generation light source.

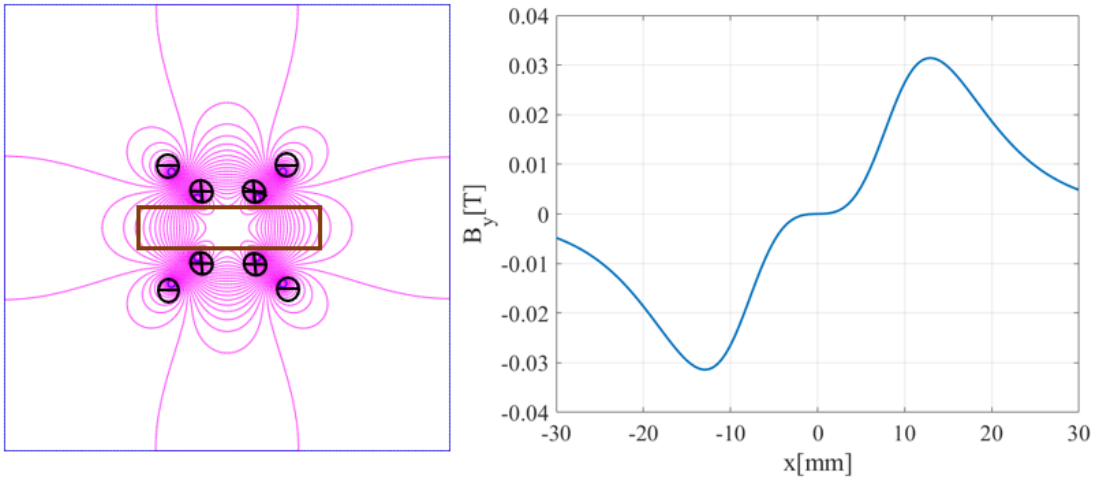


FIGURE 2.10: Cross-sectional view of a nonlinear kicker model and $B_y$ in midplane.

## 2.4 Problems of the PSM Injection by Iron-core Magnet

According to the summary of some PSM injection experiments at PF, UVSOR, and Aichi synchrotron radiation center, irregular magnetic field was possibly present at the center in the PSM injection at PF ring. It is probably caused by eddy current effect, because the excitation current of the PSM has a short pulse width that is only 1.2 µs. The eddy current effect is relatively strong due to the high-frequency magnetic field

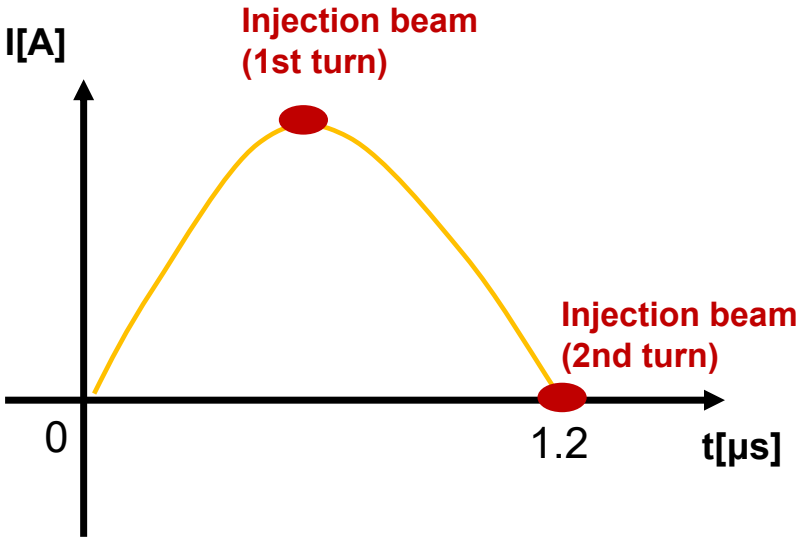


FIGURE 2.11: Timing between the excitation current and injection beam.

The timing of the excitation current and injection beam is shown in Fig. 2.11. The circumference of the PF ring is 187 m indicating the revolution period of one bunch is 624 ns. The shape of the pulsed current from power source is a half-sine wave. To realize

a one-turn injection, the pulse width had better be 1.2 μs that is twice longer than one revolution period. Therefore, the injection beam receives a strongest kick effect from the magnet at the first turn and does not suffer a kick at the second turn.

To suppress the generation of the eddy current, the PSM was made of silicon lamination steel whose thickness is 0.15 mm. The performance of lamination steel is evaluated by skin depth, which is relevant to eddy current. The equation of skin depth is given by

$$\delta = \sqrt{\frac{\rho}{\pi f \mu_r \mu_0}} \tag{2.13}$$

where $f$ is the frequency of external magnetic field, $\mu_0$ is the magnetic permeability of vacuum, $\mu_r$ is the relative permeability, and $\rho$ is the electrical resistivity.

The material properties of silicon lamination steel depend on the silicon content. The relative permeability and resistivity are assumed to be 4000 and $4.72\times10^{-7}$ Ω·m [33]. If $f$=416 kHz that corresponds to the frequency of the output current in one-turn kick condition, the skin depth is 0.008 mm that is less than the thickness of one lamination steel. In general, the lamination thickness must be less than skin depth at the operating frequency to attain the high inductance value [34]. Although thin lamination steel was used to reduce the eddy current effects, it cannot suppress the generation of eddy current completely due to the short pulse width of output current.

In addition, there is a 5 μm thickness titanium coating inside the ceramic chamber, which preserves the conductivity for the wall current. Fig. 2.12 shows the circular ceramic chamber of PSM1 and titanium coating inside of the duct. Although titanium is adopted as a low conductivity material for the eddy current suppression, the magnetic field penetrates the coating perpendicularly, which means it cannot prevent the generation of eddy current.

From the information in former sections and analysis above, eddy current effects were possibly present in PSM injection at PF ring. According to some PSM injection results, the effects of the bore shape and magnet type are unknown. After installing the PSM2, a large stored beam oscillation appeared in experiment. The shape of aperture may be a major reason. However, the aperture of the PQM and that of the nonlinear kicker are both rectangular. There was no problem of large stored beam oscillation in the

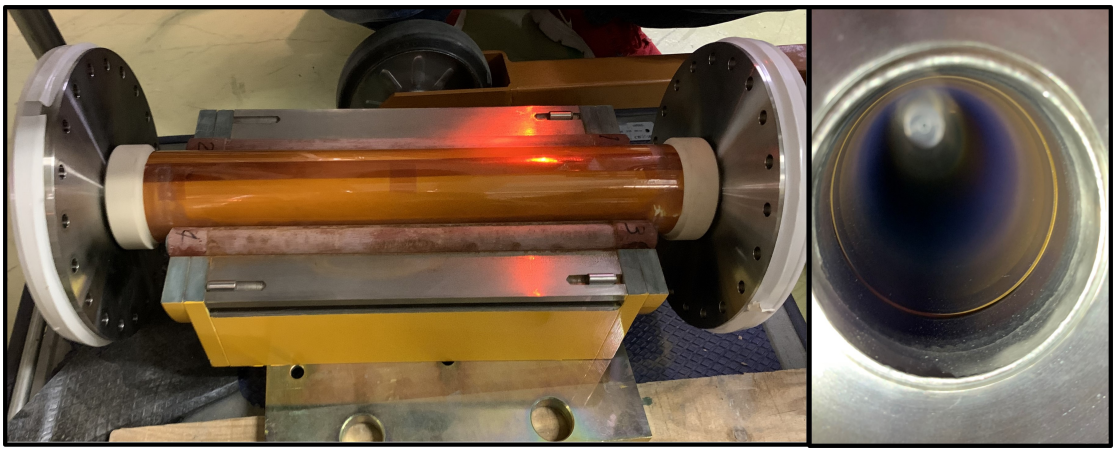

FIGURE 2.12: Ceramic chamber and titanium coating inside of the duct in PSM1.

experiments. A precise pulsed magnetic field measurement is necessary for investigating these issues.

Although the lamination steel and titanium coating are supposed to generate the eddy current, it is difficult to figure out the influence of each element in a beam injection experiment, because eddy current effects of different elements mix and act on stored beam at the same time. If their eddy current effects are separated, it can help us understand the results in previous injection experiments.

# Chapter 3

# Investigation by a Pulsed Magnetic Field Mapping

An irregular magnetic field was possibly present in the PSM injection. To investigate this issue, the pulsed magnetic field should be measured precisely. A small pick-up probe was developed as a supportive technique and was used to measure the PSM1. The experiment setup and results of the PSM measurement are presented in this chapter.

## 3.1 Technique of Magnetic Field Mapping

### 3.1.1 General Search Coil

Thus far, search coil has been the only convenient tool for measuring a pulsed magnetic field [35]. In general, a long coil with a large area is used to measure the integrated magnetic field of a dipole magnet [36, 37]. The off-axis integrated field of PSM1 for kicking the injection beam was also measured with a long coil to examine the strength of the kick effect. However, the long coil is not capable of magnetic field mapping to provide a detailed magnetic field distribution. In some cases, a short coil with numerous turns to enhance the signal is used to measure a magnetic field in small areas [38, 39]. The

designed current of the PSM1 is an approximate half-sinusoid with a 1.2 µs width. If a normal short coil is used, the Signal-to-Noise ratio (S/N) is relatively large when the coil measures a high-frequency magnetic field with a pulse width in the microsecond range because of electromagnetic noise in the measurement circuit and a small induced voltage signal. In addition, a general short coil has a thickness because of its large number of turns. Hence, it is not appropriate to measure the magnetic field in a multipole magnet that varies along the magnetic field direction.

### 3.1.2 Concept and Design of a Compact Pick-up Probe

In general, a search coil can be represented as a circuit in which the primary voltage is generated by an induced electromotive force. The output voltage is fed to a load measured with a voltmeter or oscilloscope via a transmission line. The transmission line can also generate a voltage signal that disturbs the signal generated by the main field component. To reduce the interference of the transmission line, a background coil is introduced in the design of the probe. The circuit diagram of the compact pick-up probe is shown in Fig. 3.1.

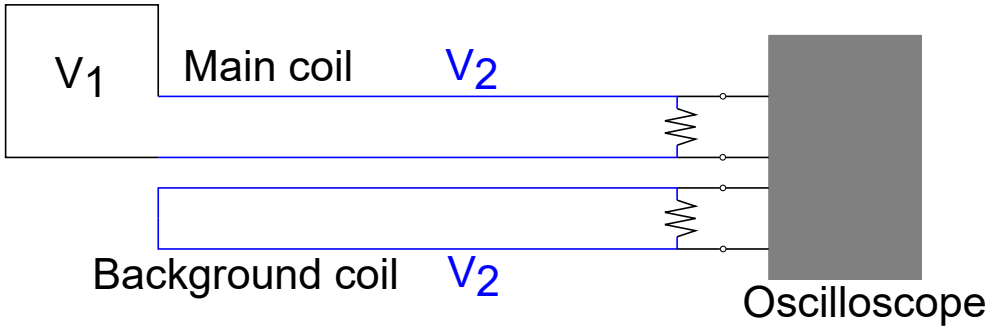


FIGURE 3.1: Circuit diagram of the compact pick-up probe.

The parameter $V_1$ is the voltage induced in the effective area, and $V_2$ is the voltage induced in the transmission line. At the end of the circuit, there is a load measured with an oscilloscope to acquire the voltage. The impedance of the load should be much larger than that of the coil to extract the voltage signal. To reduce the impedance of the transmission line and the contamination of electromagnetic noise, it is typically a shielded twisted-pair cable. The measuring voltages of the main coil $V_m$ and background coil $V_{bg}$ are $V_1 + V_2$ and $V_2$, respectively. Therefore, the effective voltage signal is given

by

$$V_1 = V_m - V_{bg} = -\frac{d\phi}{dt} \tag{3.1}$$

where $\phi$ is the magnetic flux of the effective area. If the coil is fixed, the induced voltage $V_1$ can be expressed as

$$V_1 = -\frac{d\phi}{dt} = -\frac{d}{dt} N \iint_S \mathbf{B} \cdot \mathbf{n} dS \tag{3.2}$$

where $N$ is the number of turns, $\mathbf{B}$ is the magnetic field, $\mathbf{n}$ is the normal unit vector of the area and $S$ is the area of the main coil.

The most critical parameters of the main coil are the height, width, length, and number of turns. Some aspects of the design of the main coil should be considered. First, the strength of the magnetic field component of a multipole magnet varies in the direction of the magnetic field. For a precise measurement of the magnetic field, the coil should be wound in one layer with a single-strand copper wire. Second, the width should be small because the magnetic field of a multipole magnet varies in the vertical and horizontal directions. Third, the length should also be short to enable the longitudinal magnetic field, whose strength varies because of the fringe field, to be distinguished. Fourth, the turn number should be sufficient to ensure an adequate induced voltage. However, if the number of turns is large, the mutual inductance will increase, which is not favorable for extracting a correct voltage signal; a high number of turns will also result in a large volume of the probe.

The strength of Earth's magnetic field (30 μT) is used to determine the area of the main coil. If the frequency of the magnetic field is regarded as 500 kHz corresponding to a 1 μs half-sine wave. To excite a voltage signal with an amplitude of 1 mV, the effective area of the main coil should be larger than 10.6 $mm^2$. Because the minimum scale of the oscilloscope used in our measurement is 1 mV. Then an appropriate effective area is several dozen square millimeters. A sketch of the probe designed on the basis of these considerations is shown in Fig. 3.2 (a). The number of turns is 3, the maximum width and length of the main coil are 3.2 and 5.8 mm, respectively, and the thickness of the copper wire is 0.1 mm, which is the same as the gap between the two wires. Table 3.1 gives the parameters of the main coil in each turn. Therefore, the total effective area is 40.88 $mm^2$.

Fig. 3.2 (b) shows a side view of the probe. The printed-circuit-board (PCB) was used to produce the coils. The probe has two identical boards and can measure horizontal and vertical pulsed magnetic fields simultaneously. A photograph of the probe is shown in Fig. 3.2 (c), the coaxial cable feeds into an aluminum tube that shields against high-frequency magnetic fields and is twisted together to create a cancelling effect to eliminate the electromagnetic interference. The length of the cable is 700 mm.

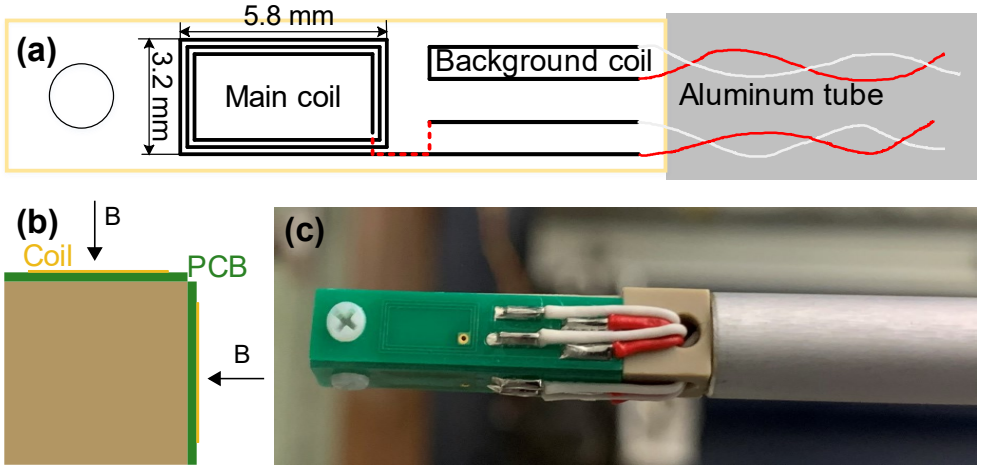


FIGURE 3.2: (a) Schematic top view, (b) front side view, (c) picture of the compact pick-up probe.

TABLE 3.1: Parameters of the main coil in each turn.

| Number | Width[mm] | Length[mm] | Area[mm$^2$] |
|---|---|---|---|
| 1 | 2.2 | 4.8 | 10.56 |
| 2 | 2.6 | 5.2 | 13.52 |
| 3 | 3.0 | 5.6 | 16.80 |

Because of the short width and length, the magnetic field component is assumed to be uniform in the measuring area of the main coil. In the measurement, the coil is fixed to be perpendicular to the magnetic field. Then the induced voltage is calculated as

$$V_1(t) = -\frac{d}{dt} N \iint_S B_0 \sin \omega t dS = -\frac{d}{dt}(N B_0 S \sin \omega t) \tag{3.3}$$

where $B_0$ is the peak pulsed magnetic field value, $\omega$ is the angular frequency of the half-sine current. If the voltage signal $V_1(t)$ is integrated, the peak value of the integral signal $F_m$ corresponds to the peak pulsed magnetic field which is given by

$$B_0 = \frac{F_m}{S} \tag{3.4}$$

## 3.2 Investigation for the issue of the PSM1

### 3.2.1 Basic Idea

It is very hard to derive an analytical solution of the eddy current in a complex model like a sextupole magnet. An experimental method is a feasible way to survey eddy current effects of components by measuring and comparing DC and pulsed magnetic fields. The PSM1 was decided to be measured. The difference between the DC and pulsed magnetic field was expected to give some clues. The PSM2 cannot be measured because it was still installed in PF ring at that time.

The photograph of PSM1 is shown in Fig. 3.3. The experimental coordinate is marked, which helps illustrate the measurement results. The origin of the coordinate is located at the magnet center. The current is supplied via the busbar. The arc copper conductor changes the current direction to generate a sextupole magnetic field.

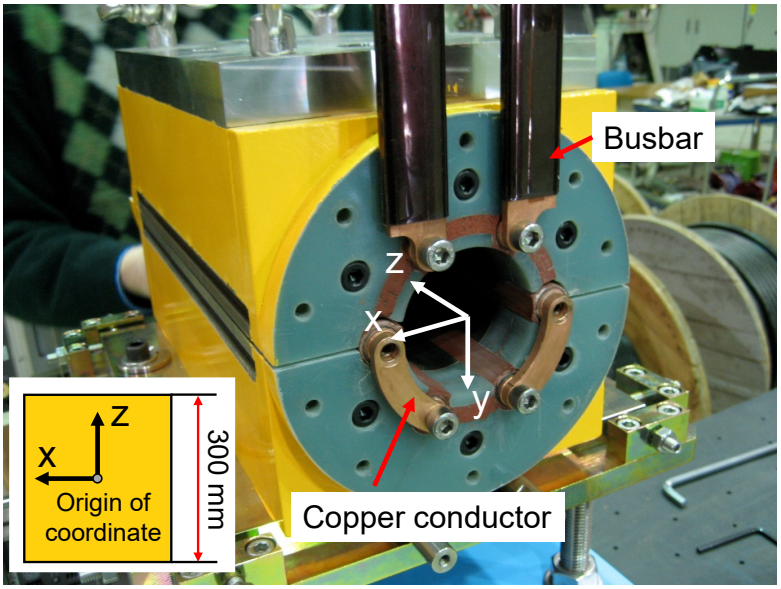


FIGURE 3.3: Photograph of PSM1.

Some basic parameters of PSM1 are shown in Table 3.2. According to the physical design, the injection beam arrives at the PSM1 where the off-axis $x$=15 mm and $y$=0 mm. Therefore, the pulsed magnetic field in the midplane of the PSM1 should be measured.

The DC magnetic field was measured with a Hall probe. Regarding accuracy, currently available Hall probes can achieve output error as low as 1%. Although the accuracy of a Hall probe is lower than that of a harmonic coil or a Nuclear Magnetic Resonance (NMR)

sensor [40]. It is a very convenient tool and can measure the magnetic field directly. In the measurement, the Hall probe (model: STF99-04-02, item number: 129937) was bought from F.W. Bell company [41].

TABLE 3.2: Basic parameters of PSM1

| Parameter | Value |
|---|---|
| Length of iron-core | 300 mm |
| Turn of the coil | 1 |
| Designed peak current | 3000 A |
| Designed pulse width | 1.2 μs |
| Designed integrated field strength | 0.12 mT·m ($x$=15 mm, $y$=0 mm) |
| Inductance | 2.9 μH |

### 3.2.2 Experimental Setup

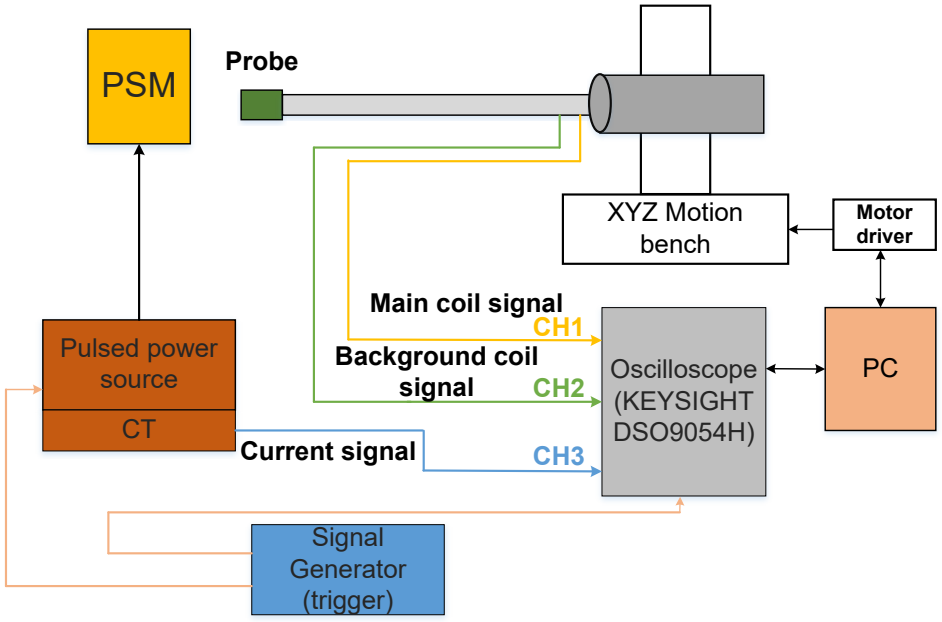


FIGURE 3.4: Diagram of pulsed magnetic field measurement system.

A diagram of the pulsed magnetic field measurement system is shown in Fig. 3.4. In the measurement, the probe is fixed on a high strength and lightweight arm made of carbon nanotubes. Three stepper motors adjust the position of the probe in the $x$, $y$, and $z$ directions. The PSM is excited by the power source, and the current is monitored by a Current Transformer (CT) to calibrate the absolute magnetic field strength. The pulse width of the current is 1 μs, which is approximately the same as the current width in

the injection experiment. In the measurement of PSM1, the peak value was 180 A. For safety in the measurement, a higher current was not supplied. The current had a jitter less than 2 % error. The oscilloscope (KEYSIGHT DSO9054H) receives three signals and mathematically manipulates the raw signals, which is favorable for the calculation [42].

The DC magnetic field measurement system is similar except for the probe. The supplied current was 15 A to prevent magnet overheating. The Hall probe was connected to a gaussmeter (Model 9500) made by F.W. Bell company, which was linked to the PC by GPIB interface. The background magnetic field was also measured. The background data subtracted from the main field data gives the magnetic field generated by PSM1.

In the measurement, the step size of the arm is 1 mm along the horizontal $x$ axis, and 2 mm along the longitudinal $z$ axis.

A program has been constructed to perform magnetic field mapping. The GUI screenshot is shown in Fig. 3.5, which is developed by Python script. Although the pulsed magnetic field is only measured in the midplane of PSM1, the program can perform a 3D mapping measurement. The current location of the probe is observed in the panel. In addition, the measurement can be temporarily stopped if some accidents happen. Because of the wide measurement region, the amplitude of signal can change significantly during the whole measurement. Refreshing the display of oscilloscope is necessary in the program to pick a correct peak value of the signal.

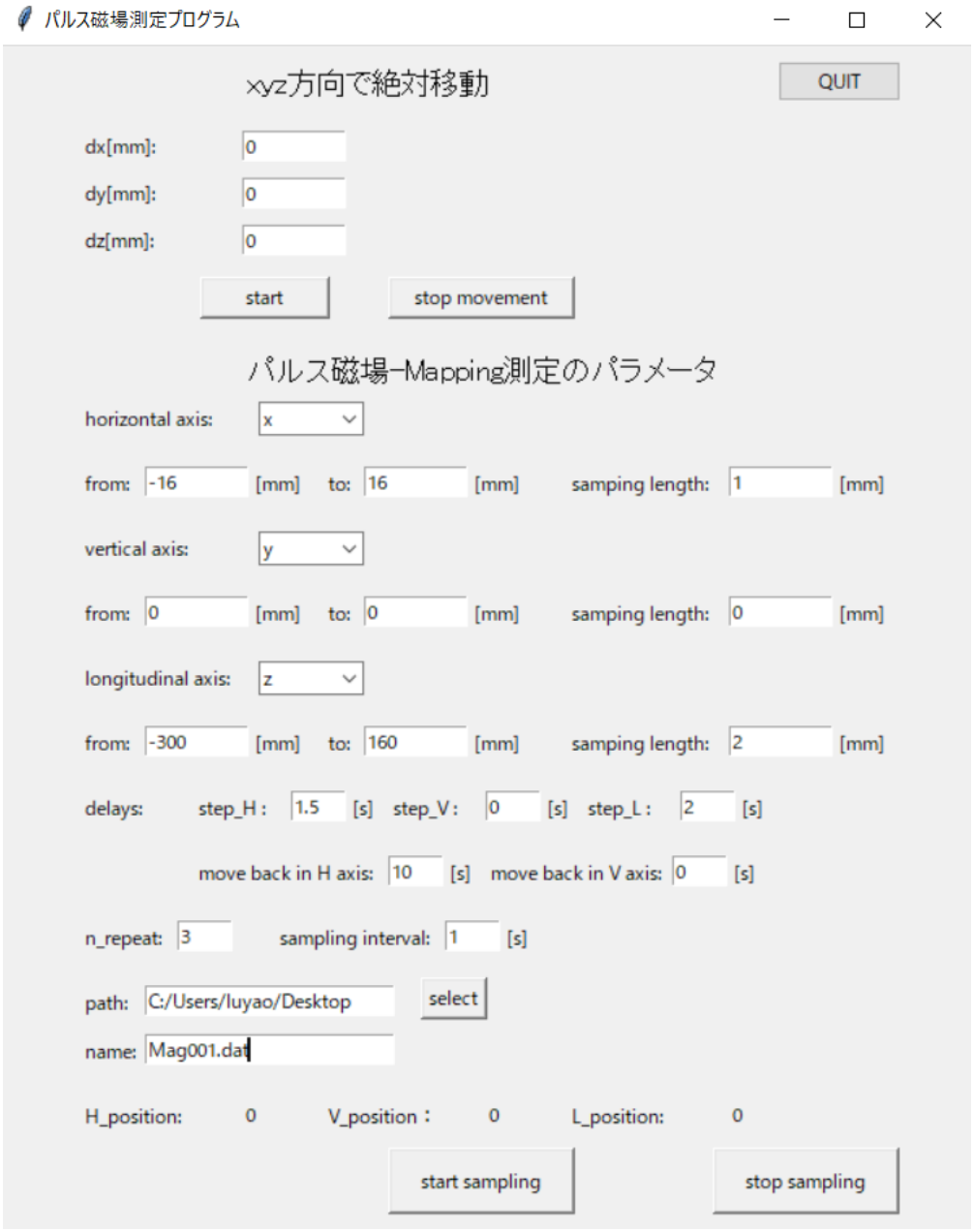


FIGURE 3.5: The GUI screenshot of mapping measurement.

To evaluate the eddy current effect of the titanium coating, the pulsed magnetic field was measured without the chamber at first. Then the chamber was inserted into the magnet, and the measurement was carried out again. It can help us understand the measurement result better because the effect of the coating is separated. The photograph of measuring PSM1 with and without the chamber is shown in Fig. 3.6.

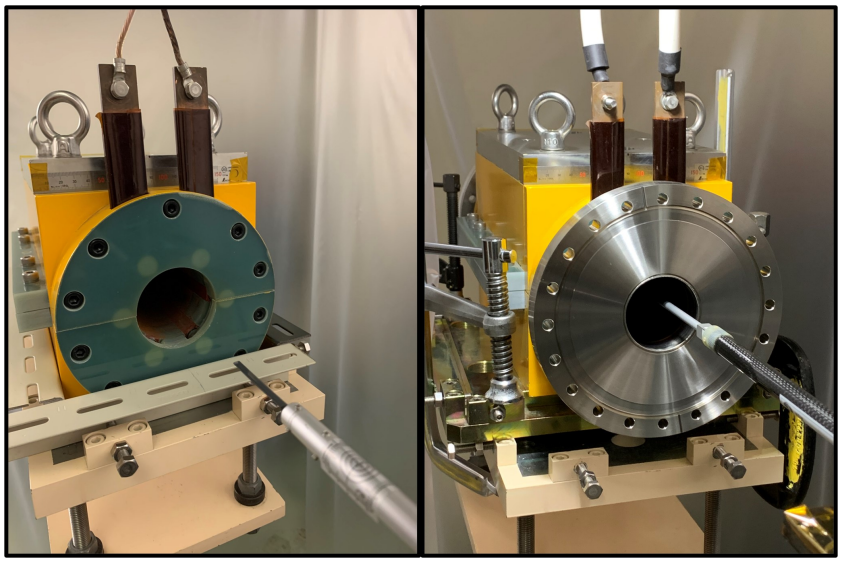

FIGURE 3.6: Photograph of measuring PSM1 with and without the chamber.

### 3.2.3 Performance Test and Error Estimation of the Probe

To examine the performance of the probe, we moved the probe to $(x, y, z) = (16,0,0)$ to measure the pulsed magnetic field. Fig. 3.7 shows a screenshot of the signals in the oscilloscope.

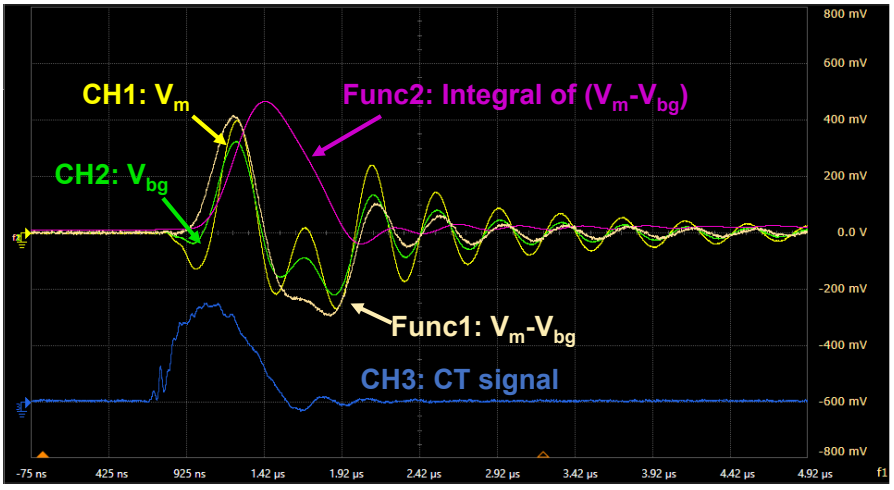


FIGURE 3.7: Screenshot of signals in the oscilloscope.

Fig. 3.8 shows the waveforms extracted from the oscilloscope. Parameters $V_m$ and $V_{bg}$ are voltage signals from the main coil and the background coil, respectively. If the $V_m$ signal is integrated, the shape of the integral signal is deformed, and the peak value is 166 nV·s. However, if the $(V_m - V_{bg})$ signal is integrated, the integral signal exhibits a smooth and a half-sine wave shape. The peak value becomes 114 nV·s. In Fig. 3.9,

the integral signal of $(V_m - V_{bg})$ is compared with the current signal from the CT. The waveform of the integral of $(V_m - V_{bg})$ is almost identical to the current signal. In Fig. 3.9, the peak value appears at 1.40 µs. Therefore, in the measurement, the integral signal at the specific timing $t_0$= 1.40 µs was selected for measuring a bidirectional pulsed magnetic field.

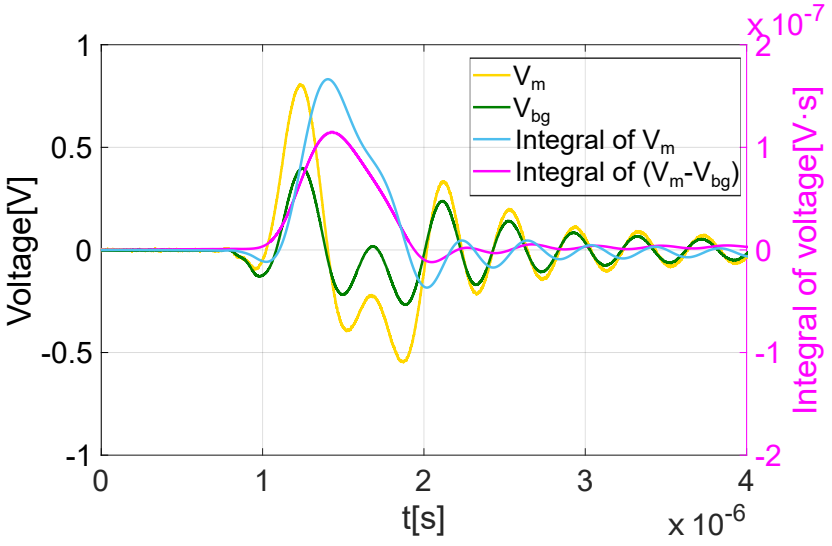


FIGURE 3.8: Raw signals at $x$ =16 mm ($y, z$=0 mm).

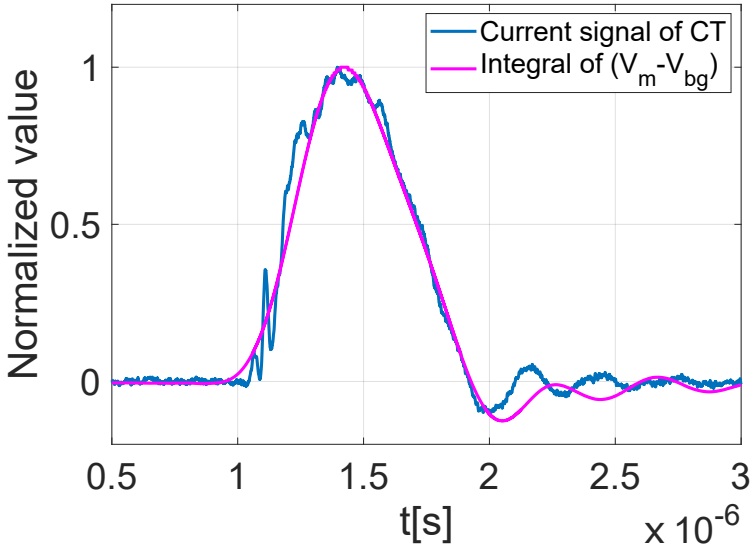


FIGURE 3.9: Comparison between the CT signal and integral signal of $(V_m - V_{bg})$.

The resolution power of the probe is mainly limited by the noise signal introduced by electromagnetic noise into the circuit. Even if the probe measures a zero-magnetic-field region outside the PSM1, the integral signal of $(V_m - V_{bg})$ is a noise signal with a 1.2 nV·s maximum amplitude. According to Eq.3.4, the noise level is $2.9 \times 10^{-5}$ T.

Therefore, if the measuring peak field is not greater than $2.9 \times 10^{-5}$ T, the probe is not capable of detecting the signal generated by the magnetic field. If the measuring peak magnetic field is sufficiently strong, like the result in Fig. 3.9, the influence of this systematic error is less than 1.1%. In addition, the calculation of the effective area also introduces a systematic error into the measurement. If the average width (2.6 mm), length (5.2 mm) and turn number are used, the effective area becomes 40.56 $mm^2$. The difference compared with the data in Table 3.1 is 0.32 $mm^2$, which leads to a 0.8% error ratio. Some error sources in the pulsed magnetic field measurement are summarized in Table 3.3.

TABLE 3.3: Error estimations in the measurement.

| Error source | Value |
|---|---|
| Jitter of the CT signal | $< 2\%$ |
| Repetition error | $< 5.7 \times 10^{-5}$ T |
| Area of the coil | $< 1\%$ |
| Electromagnetic noise | $\approx 2.9 \times 10^{-5}$ T |

## 3.3 Alignment before Measurement

### 3.3.1 General Alignment Methods and Misalignment Problem

To measure magnetic field correctly, a precise alignment is essential before the measurement. The bubble level was used to reduce the tilt. As shown in Fig. 3.10, two bubbles were put on the magnet. The error of tilt is less than 0.05 mrad. The tilt of XYZ motion bench was also adjusted by the bubble level.

The alignment in the vertical direction was performed by a Wild N3 shown in Fig. 3.11. Therefore, the sensor of the Hall probe and coil of the pick-up probe can be located in the midplane of PSM1.

As for the alignment in the longitudinal direction, a general way is to move the probe above the top of the magnet. Then the alignment line of the magnet is adjusted to be parallel with the probe on both sides. However, the XYZ motion bench has a limitation of $y$ axis. The position of the probe cannot be higher than the height of the magnet. To solve this issue, we used a theodolite to do the longitudinal alignment. The basic concept is that the view of the theodolite is adjusted to be parallel with the trajectory

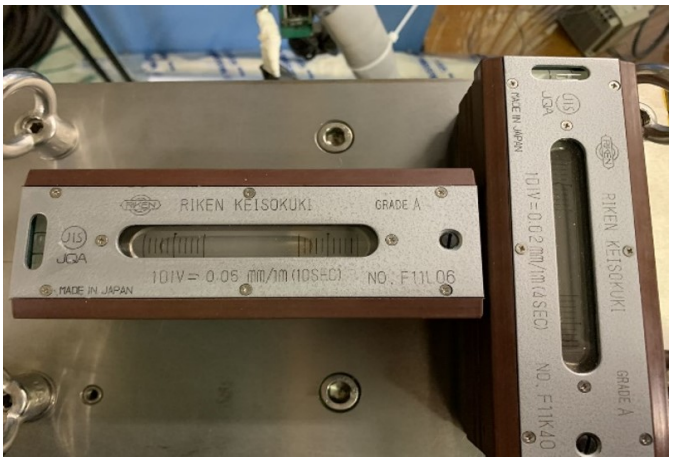


FIGURE 3.10: Bubble level alignment for adjusting tilt.

FIGURE 3.11: Wild N3 for alignment in the vertical direction.

of the probe. Then the magnet is moved carefully to make the alignment line parallel with the sight line of the theodolite.

Measuring the longitudinal magnetic field distribution is a good method to check whether the alignment in the longitudinal direction is effective or not. It can be evaluated by the flatness of magnetic field. The longitudinal distribution of the DC magnetic field at $x$=5 mm ($y$=0 mm, $-150 \leq z \leq 150$ mm) was measured. The magnetic field data in PSM1 is shown in Fig. 3.12. Visibly, such a flatness of magnetic field is unacceptable in the measurement.

The assembly of PSM1 cannot be the reason for generating such a magnetic field, because PSM1 performed PMM injection successfully. After careful consideration, it is found that there was a misalignment between the theodolite and the probe. The support of theodolite could not be moved smoothly along horizontal direction at that time. So the sight line of theodolite was very hard to be parallel with the probe when we used the theodolite to track the trajectory of the probe. Furthermore, it is also difficult to see the alignment line clearly at the end part of the magnet by the theodolite, which may

easily produce an error. The misalignment in the longitudinal direction must be solved, otherwise the measurement is not reliable.

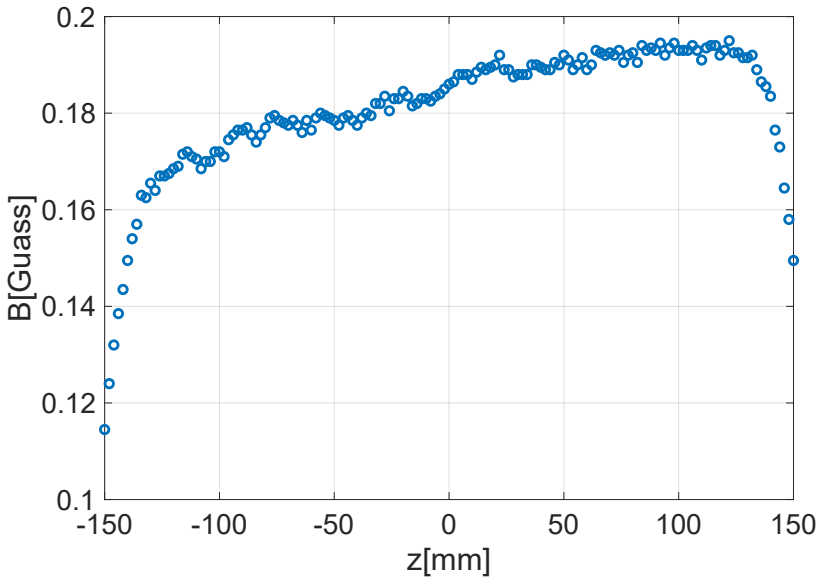


FIGURE 3.12: Initial longitudinal magnetic field distribution at $x$ =5 mm.

### 3.3.2 Magnetic Field Based Alignment

A magnetic field-based alignment method was proposed to improve the precision. It is assumed that the magnetic field of PSM1 is ideal. if a horizontal distribution is measured by the probe, the center of the magnet is located at the position where magnetic field is zero. Therefore, the measurement result can give the relative distance between magnet center and probe.

The horizontal distributions at $z$=-150, 0, 150 mm ($y$=0 mm) were measured. The center of the magnet can be estimated from the fitting curves. The result is shown in Fig. 3.13.

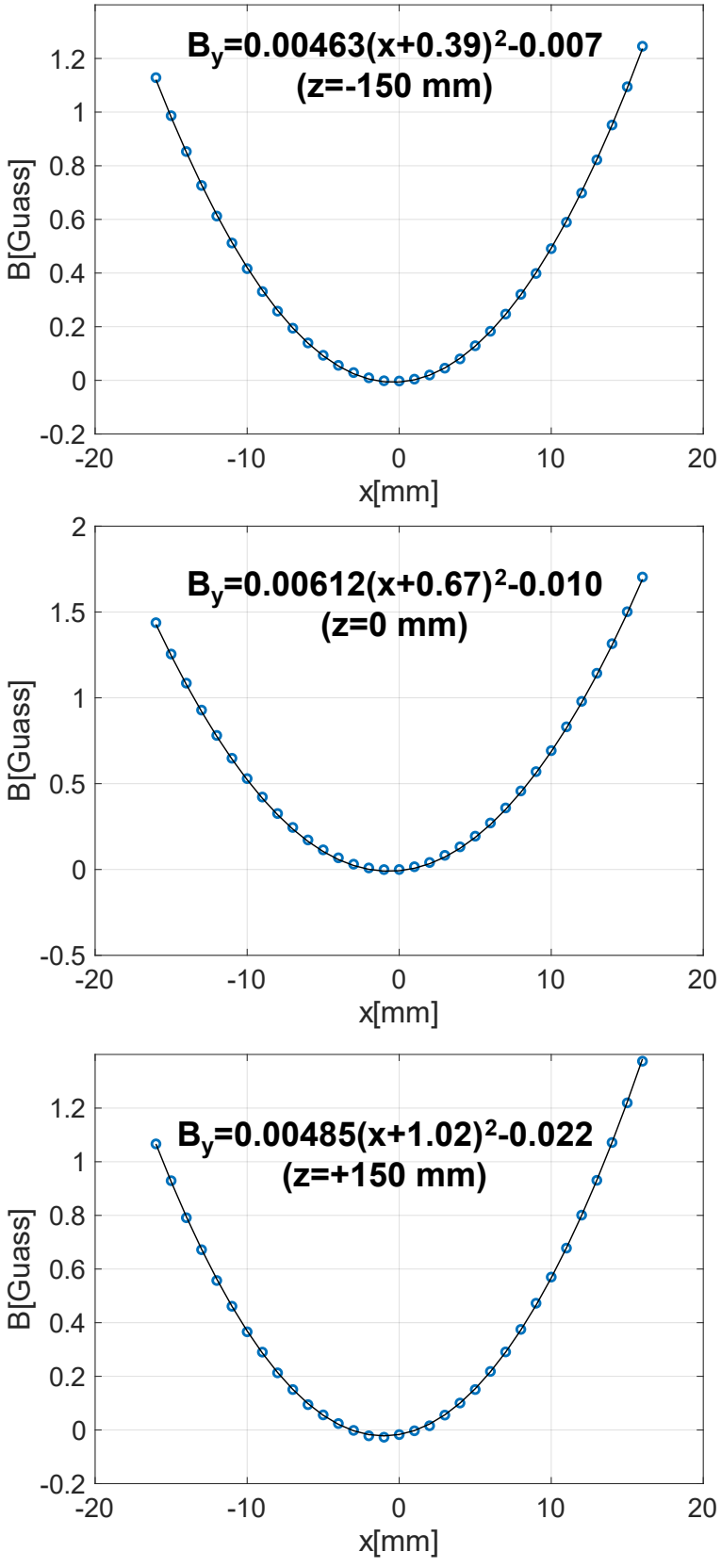


FIGURE 3.13: Horizontal magnetic field distributions at $z$=-150, 0, 150 mm ($y$=0 mm) before the alignment.

It can be seen that the distance between the magnet center and probe gradually becomes large if the longitudinal position is increased. On the basis of the measurement results, a sketch of misalignment situation is shown in Fig. 3.14. The red line is the estimated trajectory of the probe. If a longitudinal distribution with a positive off-axis value is measured, obviously, the magnet field will be gradually stronger when the probe is inserted deeply, which is agree with the result in Fig. 3.12.

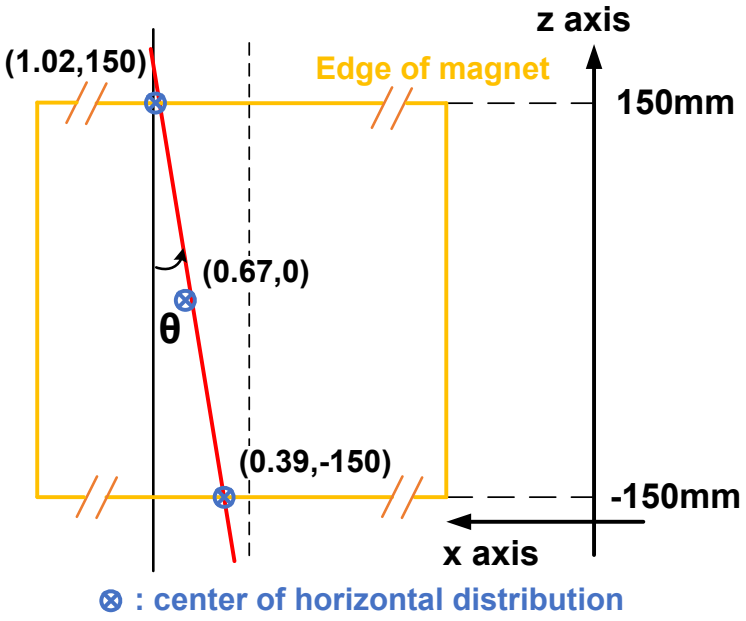


FIGURE 3.14: Sketch of the misalignment between the magnet and probe.

According to the sketch, the alignment was performed as follows: Firstly, the magnet should be parallel with the probe by adjustment. Because the deviation is negligible compared with the length of PSM1, the $\theta$ is almost equal to the horizontal deviation of probe in PSM1. The end part of PSM1 can be fixed and the other side is moved about 0.6 mm towards negative x direction. Then the distance between probe and magnet center would be about 1 mm. The probe was moved 1 mm towards negative x direction so that the trajectory of the probe nearly coincided with the center line of magnet.

Because the magnet is adjusted manually, it is necessary to measure the horizontal distributions again and repeat the magnetic field based alignment to improve the alignment precision. The final horizontal distributions is shown in Fig. 3.15.

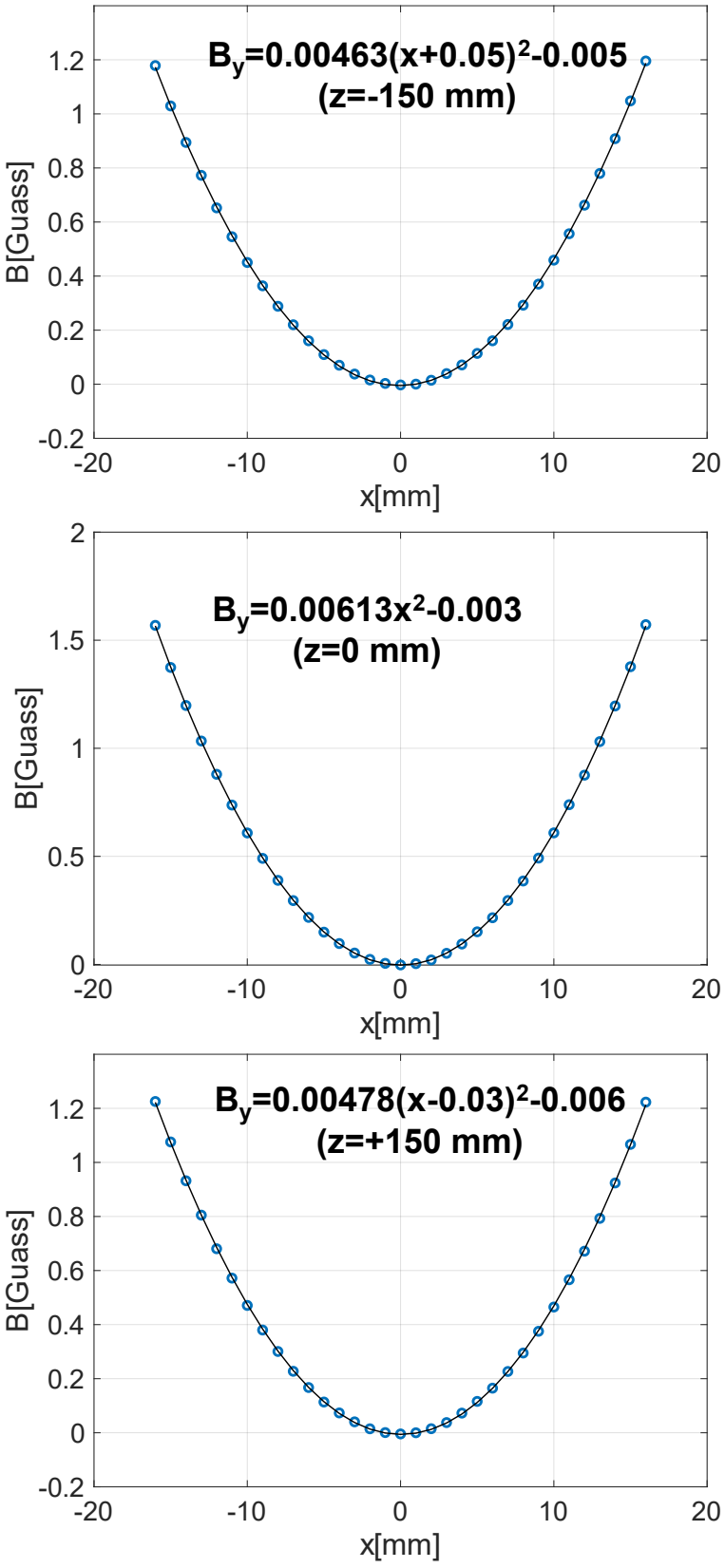


FIGURE 3.15: Horizontal magnetic field distributions at $z$=-150, 0, 150 mm ($y$=0 mm) after the alignment.

From the fitting curves, the deviation between magnet and probe is much reduced. When the probe moves from the entrance to the end of PSM1, the horizontal deviation is only 0.08 mm.

Then the longitudinal distribution at x=5 mm was measured again, which is compared with the former result in Fig. 3.16. After alignment, the flatness of the magnetic field is improved clearly.

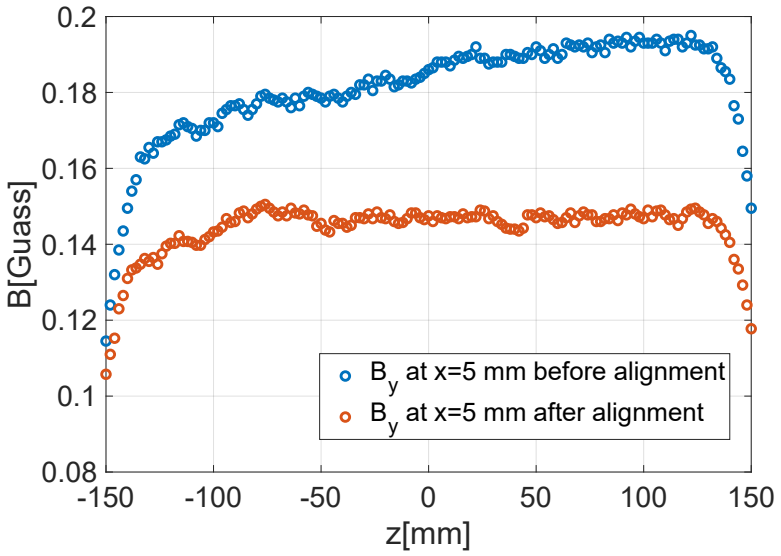


FIGURE 3.16: Comparison of the longitudinal magnetic field distributions at $x$=5 mm.

## 3.4 Magnetic Field Measurement Results

To examine the integrated field strength and the parabolic distribution of a sextupole magnet, we conducted general magnetic field mapping of PSM1 without the chamber installed. For comparison with the pulsed magnetic field, the DC magnetic field was normalized under the condition of a 180 A current which was the peak value of the pulsed current.

### 3.4.1 General Magnetic Field Mapping

Figure 3.17 shows the magnetic field mapping in the longitudinal direction at $x$=15 mm ($y$=0 mm, $-300 \leq z \leq 300$ mm) where the injection beam passes. The value of the integrated voltage signal at $t$=$t_0$ was used for measuring a bidirectional pulsed magnetic

field. The error bar shows the repetition error in the pulsed magnetic field measurement, which is less than $5.7 \times 10^{-5}$ T. The shape of the normalized DC magnetic field distribution is consistent with the shape of the pulsed magnetic field. As shown in Fig. 3.3 and Fig. 3.17, the busbar breaks the symmetry of the current flow. Therefore, the magnetic field is negative around $z$=-200 mm, but not around $z$=200 mm.

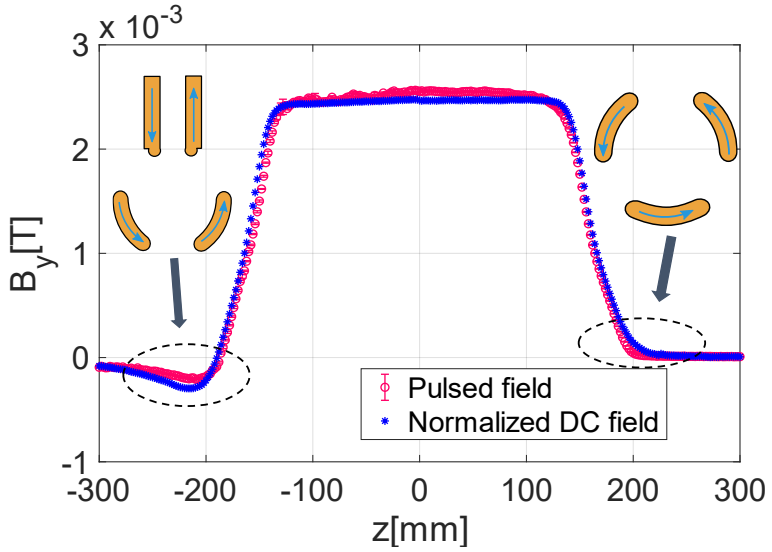


FIGURE 3.17: Longitudinal magnetic field distributions ($x$=15 mm, $y$=0 mm, $-300 \leq z \leq 300$ mm).

As shown in Fig. 3.18, the normalized DC magnetic field is a parabolic line that coincides with the nature of a normal sextupole magnet. However, the pulsed field distribution has an offset around the center, which indicates the presence of an irregular and opposite pulsed magnetic field $B_y$.

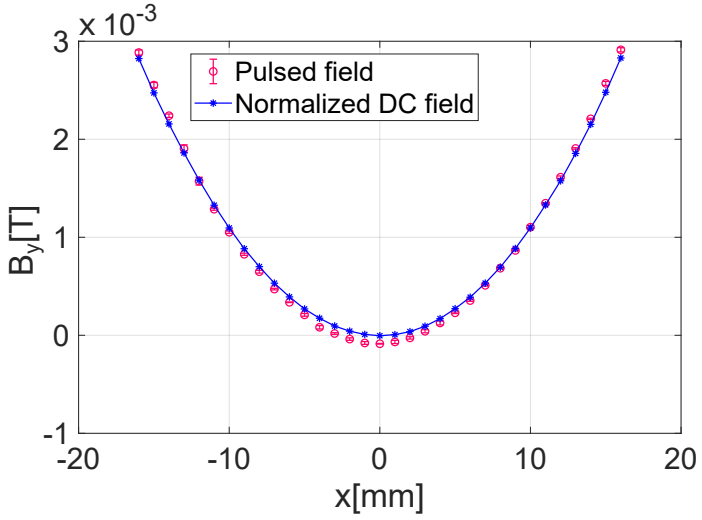


FIGURE 3.18: Horizontal magnetic field distributions ($-16 \leq x \leq 16$ mm, $y$=0 mm, $z$=0 mm).

### 3.4.2 Longitudinal Magnetic Field Mapping at $x$=0 mm

To investigate the opposite pulsed magnetic field $B_y$ around the center, we conducted the mapping along the longitudinal center axis. In the measurement, the minimum value of the integrated voltage signal was used to calculate the peak value of the negative magnetic field, which differs from the result of the measurement performed by selecting the value at $t = t_0$.

The longitudinal magnetic field distributions ($x, y$=0 mm, $-300 \leq z \leq 300$ mm) are shown in Fig. 3.19. Outside the PSM1, the pulsed magnetic field strength at $z$=-200 mm is $2.2 \times 10^{-4}$ T, which is less than the normalized DC magnetic field strength of $3.2 \times 10^{-4}$ T. Inside the PSM1, the opposite magnetic field strength is $1.2 \times 10^{-4}$ T at the center. The pulsed magnetic field is clearly stronger at the end of the iron core.

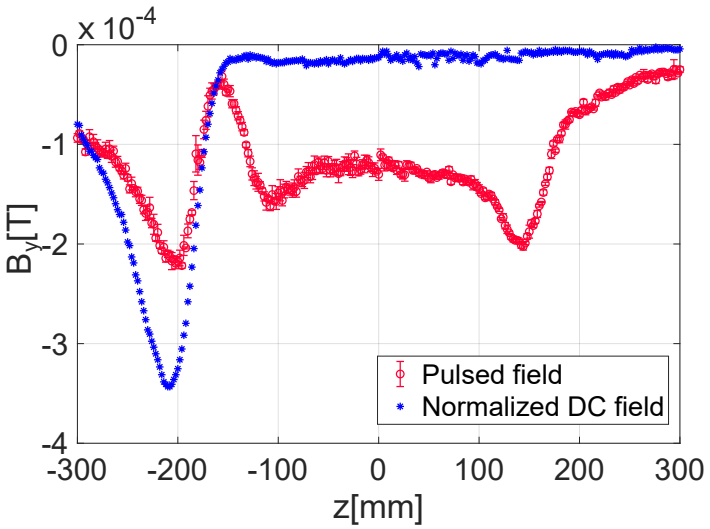


FIGURE 3.19: Longitudinal magnetic field distributions ($x, y$=0 mm, $-300 \leq z \leq 300$ mm ).

The waveform of the integrated voltage signal demonstrates that the $B_y$ inside PSM1 is mainly generated by the eddy current effect of the iron core. Figure 3.20 shows the signals at $z$=-200 and 0 mm ($x, y$=0 mm). However, the peak pulsed magnetic field at $z$=-200 mm is smaller than the normalized DC magnetic field. The eddy current effects around the end of PSM1 can decrease the main field component. At $z$=-200 mm, the shape is a clear half-sine shape and the peak timing appears at 1.44 µs, which is similar to the peak timing in Fig. 3.9. This result indicates that the dominant component of the measured magnetic field is the main field. However, the signal at the center of the magnet is a nearly full-sine wave. The peak timing $t_e$ is 1.20 µs. It is a typical eddy-current

magnetic field shape that opposes the change of the main field. Consequently, the peak timing of the eddy-current magnetic field is earlier than that of the main magnetic field.

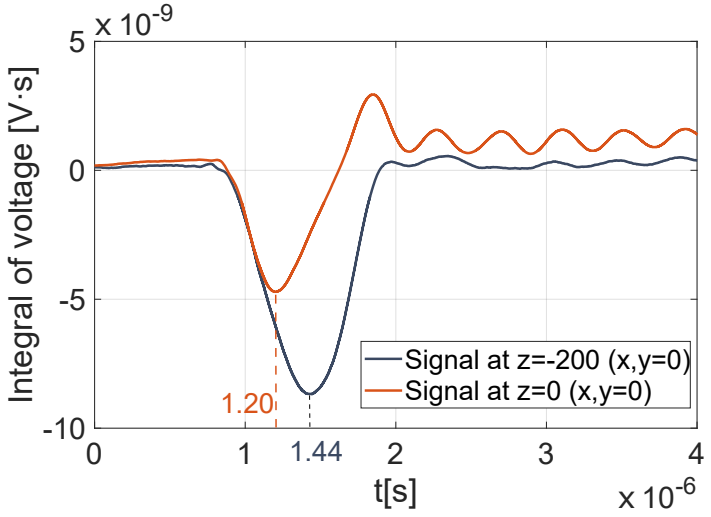


FIGURE 3.20: Integrated voltage signals at $z$=-200 and 0 mm ($x, y$=0 mm).

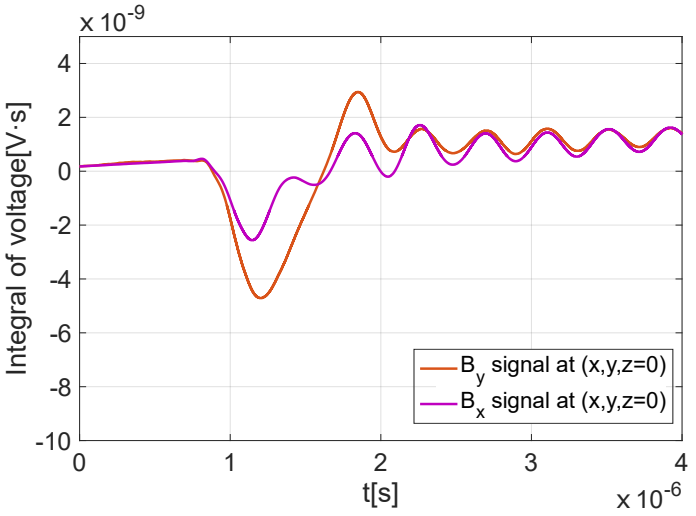


FIGURE 3.21: Integrated voltage signal of the $B_y$ and $B_x$ ($x, y, z$=0 mm).

The eddy-current magnetic field $B_y$ in the vertical direction was observed at the center, and the horizontal $B_x$ at the center of the magnet was also measured. As shown in Fig. 3.21, the integrated voltage signal of the $B_x$ was measured at the magnet center. However, the shape of the $B_x$ signal is not a typical integrated voltage signal with a full-sine or half-sine shape. Because the strength of the $B_x$ is very small, which results in a low S/N and a deformed integrated voltage signal. The minimum value of the $B_x$ signal is 2.2 nV·s which is less than the value of the $B_y$ signal (4.7 nV·s). We extracted the minimum value to calculate the $B_x$ for comparison with the $B_y$, which is shown in Fig. 3.22. The strength of the $B_x$ is clearly much weaker than that of the $B_y$.

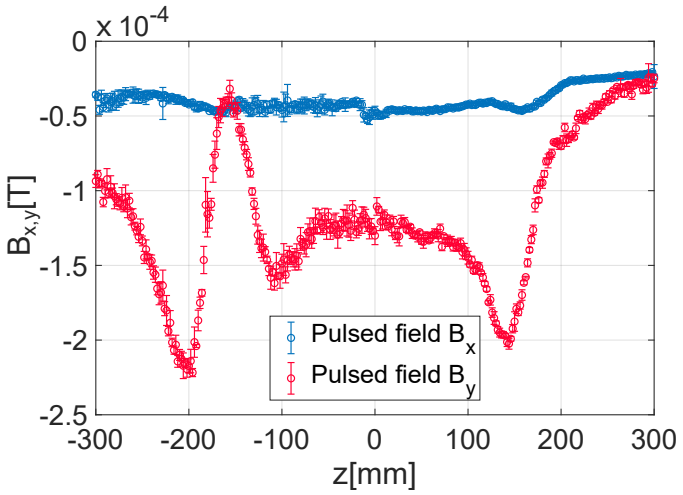


FIGURE 3.22: Longitudinal distribution of the $B_y$ and $B_x$ ($x, y$=0 mm, $-300 \leq z \leq 300$ mm).

### 3.4.3 Measurements with the Chamber Installed

Then the magnetic fields of PSM1 was measured with the chamber installed. As shown in Fig. 3.23, the pulsed magnetic field with the chamber is compared with the result without the chamber at the center of the magnet ($y, z$=0 mm). The off-axis magnetic field at $x$=15 mm is slightly reduced. Therefore, the effect of the titanium coating hardly influences the kick effect to the injection beam. The magnetic field around the center should be checked carefully, because the stored beam is much sensitive to the strength of magnetic field.

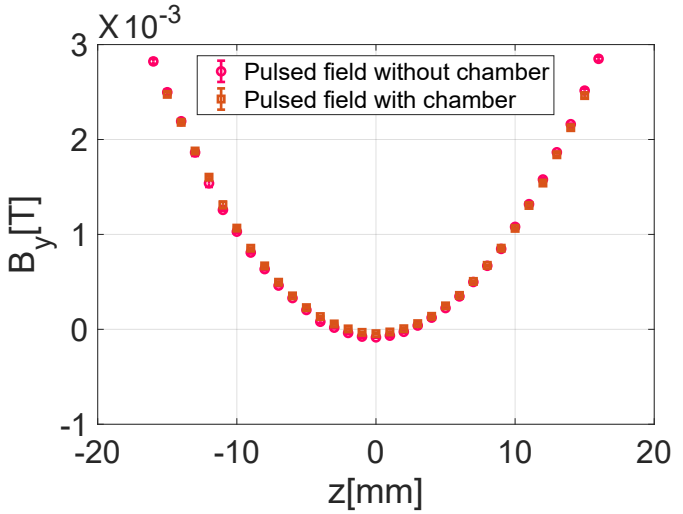


FIGURE 3.23: Horizontal pulsed magnetic field distributions at the center.

The longitudinal distribution at the center was measured again. In the measurement, it was found that the joint between the chamber and the flange was a magnetic material,

which was made from Kovar. The effect of the Kovar to the pulsed magnetic field should also be considered.

The layout of the measuring objects is shown in Fig. 3.24 (a). The thickness of the flange was 22 mm, and the edge was located at $z$=-250 mm. Therefore, the position of the Kovar is approximately at $z$=-228 mm. First, the DC magnetic field of the center longitudinal distribution was measured. From the difference curve shown in Fig. 3.24 (b), the peak point is at $z$=-226 mm, which is near the Kovar joint. Inside the iron core, the value of the difference is almost zero. It is concluded that the Kovar joint influences the DC magnetic field, whereas the titanium coating does not affect the DC magnetic field because it is nonmagnetic.

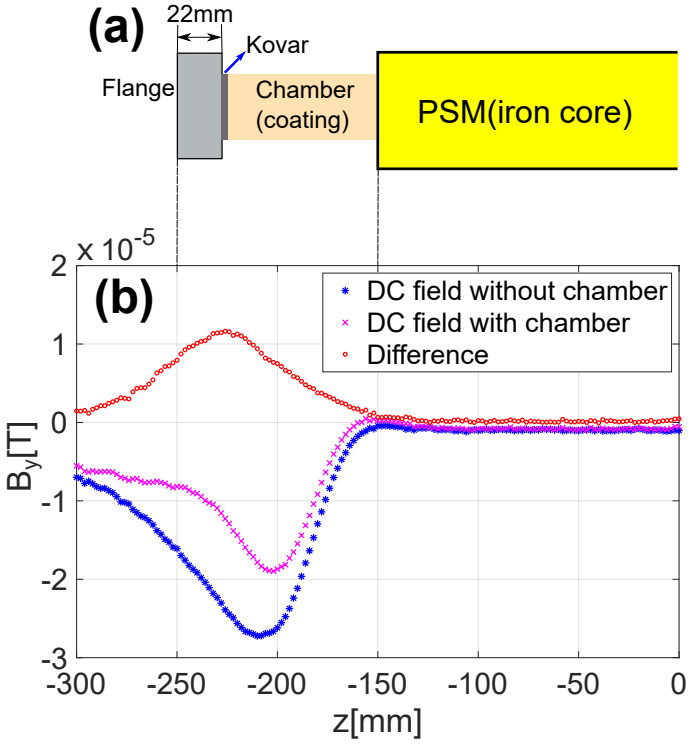


FIGURE 3.24: (a)Layout of the measuring objects. (b)Comparison of the longitudinal distributions of the DC magnetic field ($x, y$=0 mm, $-300 \leq z \leq 0$ mm; difference = (value with chamber) − (value without chamber)).

The result of the pulsed magnetic field $B_y$ is shown in Fig. 3.25. Inside the PSM, the difference is less than $2.7 \times 10^{-5}$ T, which is smaller than the systematic error of $2.9 \times 10^{-5}$ T caused by the electromagnetic noise. Therefore, we considered that the titanium coating did not generate an irregular magnetic field inside the PSM. Because of the symmetric external magnetic field and the circular shape, the eddy-current magnetic field may be compensated at the center.

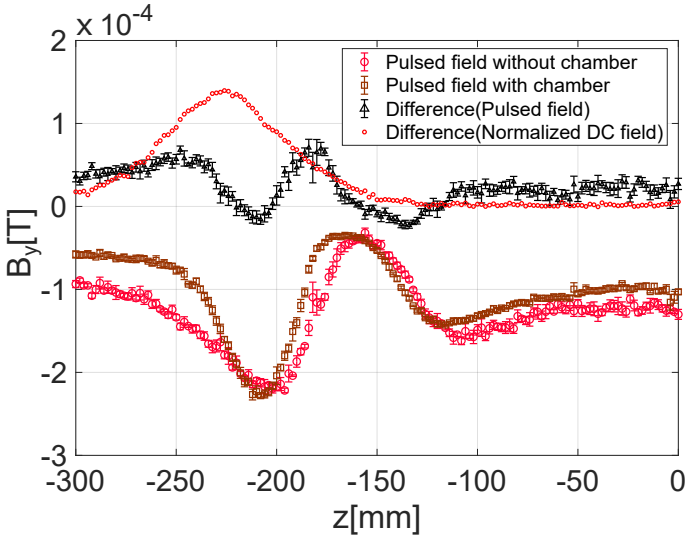


FIGURE 3.25: Comparison of the longitudinal distributions of the $B_y$ ($x, y$=0 mm, $-300 \leq z \leq 0$ mm; difference = (value with chamber) - (value without chamber); the scale of the DC field changed because of the current normalization).

Outside the PSM ($-300 \leq z \leq -150$ mm), the shape of the difference curve (pulsed field) differs from that of the normalized DC magnetic field. From $z$=-300 to -250 mm, the pulsed magnetic field with the chamber installed is smaller than the pulsed field without the chamber. However, the difference (pulsed field) at $z$=-226 mm is $1.9 \times 10^{-5}$ T, which is much smaller than the corresponding normalized DC magnetic field ($1.4 \times 10^{-4}$ T). If the distribution of the difference (pulsed field) is identical to the distribution of the difference (normalized DC field), the effect of the Kovar joint on the pulsed magnetic field can be examined. However, the current measurement result cannot provide information about whether the Kovar affects the pulsed magnetic field. Another irregular magnetic field was present from the eddy current effect of the coating because the external magnetic field is not symmetric outside the PSM. We considered that a pulsed magnetic field generated by the eddy current of the coating outside the PSM was overlapped with the effect of the Kovar. Hence, the effect of the Kovar on the pulsed magnetic field cannot be examined directly in our experiment.

To evaluate whether there is an irregular magnetic field that can induce vertical stored beam oscillation, the longitudinal distribution of $B_x$ was also measured with the chamber installed. Fig. 3.26 shows the pulsed magnetic field result in the $x$ direction. The pulsed magnetic fields with and without the chamber installed are approximately $5.0 \times 10^{-5}$ T. The difference curve of the pulsed magnetic field is close to zero. Therefore, the eddy current effect of the Kovar joint and the titanium coating in the $x$ direction is too weak

to be detected by the probe. From the result, we concluded that an irregular $B_x$ did not appear, which proved that there was no issue of the vertical stored beam oscillation in the operation.

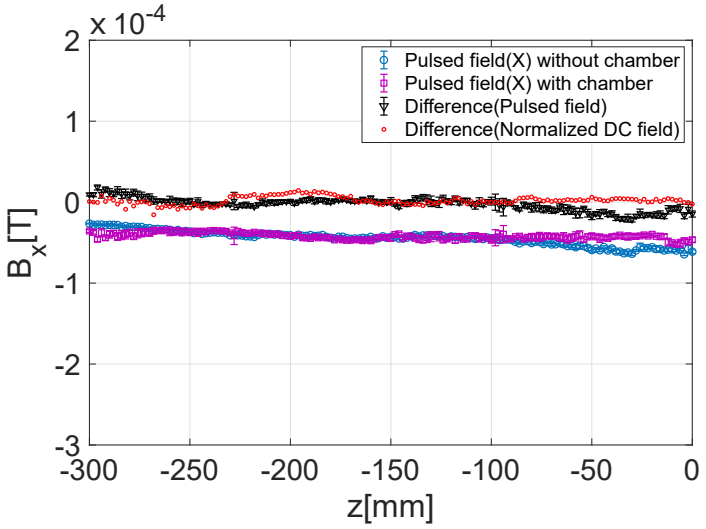


FIGURE 3.26: Comparison of the longitudinal distributions of the $B_x$ ($x, y$=0 mm, $-300 \leq z \leq 0$ mm; difference = (value with chamber) - (value without chamber)).

## 3.5 Discussion

To investigate the irregular magnetic field at the center of PSM1, a compact pick-up has been developed. The performance of the pick-up probe was examined by comparing the pulsed and DC magnetic fields. In the measurement, even the integrated voltage signal generated by an amplitude of $2.2 \times 10^{-4}$ T magnetic field was measured clearly. Furthermore, the eddy-current signal of the $B_y$ was observed at the center of PSM1, which proved the presence of the eddy-current magnetic field generated by the iron core. From the measurement result, it is concluded that the irregular pulsed magnetic field at the center of PSM1 consists of the eddy-current magnetic field and the field component generated from the busbar structure.

In the measurement, the pulsed magnetic field distribution slightly differs from the result of the normalized DC magnetic field, which can be distinguished from Fig. 3.17 and Fig. 3.18. Although some error sources of the pick-up probe are summarized. The difference may also be caused by the eddy current effect of the iron core. For example, the pulsed magnetic field outside the PSM1 is weaker than the normalized DC magnetic

field in Fig. 3.17. Some reports show that in the AC magnetic field measurement of dipole magnet, the eddy current effect of the lamination steel is strong due to the $B_z$ components of the fringe field, which can reduce the side magnetic field [43, 44]. Analogously, the fringe field of PSM1 may induce the eddy current that affects the strength of the magnetic field. In Fig. 3.19, the eddy-current magnetic field is stronger at the end of PSM1, which shows the hypothesis is reasonable.

Although, some properties of the pulsed magnetic field were measured by this pick-up probe. The results need to be investigated in the future. The eddy-current $B_x$ field is much weaker than eddy-current $B_y$ field in the measurement, which confirms that there was no issue about the vertical stored beam oscillation in the PSM1 injection. However, the mechanism of the phenomenon cannot be explained now. As for the Kovar, a detailed study of the effect of the Kovar on a pulsed magnetic field is necessary. Using a chamber without titanium coating is a possible way to observe the effect of the Kovar clearly in pulsed magnetic field measurement.

# Chapter 4

# Understanding of the Eddy Current Effect of the Iron Core and Coating

To gain a further understanding about PMM injection, simulations about the stored beam oscillation and transient magnetic field are performed to understand the previous results. These analyses give an idea of designing a pulsed magnet for PMM injection.

## 4.1 Estimation of Stored Beam Oscillation from the Eddy-current Magnetic Field in PSM1

To estimate the stored beam oscillation, the way of generating a natural stored bunch distribution is introduced. Then the stored beam oscillation induced by the perturbation is observed in SAD [45] by particle tracking.

### 4.1.1 Generation of a Stored Bunch Distribution

The property of stored beam depends on the parameters of electron storage ring and is not associated with injection beam. Based on the beam envelope theory [46], the distribution of a stored bunch satisfies:

$$\Sigma = M\Sigma M^T + B \tag{4.1}$$

where $M$ is the one-turn transfer matrix evaluated around the closed orbit, $B$ represents the excitation of the oscillation by radiation, $\Sigma$ is the beam distribution matrix. The computation detail is given in Appendix A.

In a case that the phase space of particle is described by six variables $v = (x, p_x, y, p_y, z, \delta)$, where $x$ and $y$ are the horizontal and vertical position from the reference orbit, $p_x$ and $p_y$ are their canonical conjugate momenta, $\delta$ is the deviation of the momentum from the reference, and $z$ is its conjugate variable, then the $\Sigma$ in a specific position is given by

$$\begin{aligned} \Sigma &= \langle \boldsymbol{u}\boldsymbol{u}^T \rangle \\ \boldsymbol{u} &= \boldsymbol{v} - \boldsymbol{v}_0 \end{aligned} \tag{4.2}$$

where $\boldsymbol{v}_0$ is the particle motion at the closed orbit.

One matrix $D = AC$ can be found to diagonalize the $M$ [47]. The $A$ matrix is a decoupling matrix explained in Appendix B using a different method compared with Teng-Edwards Parametrization [48], and $C$ is a phasor matrix expressed as

$$C = \begin{bmatrix} \frac{\sqrt{2}}{2} & \frac{\sqrt{2}}{2} & & & & \\ -i\frac{\sqrt{2}}{2} & i\frac{\sqrt{2}}{2} & & & & \\ & & \frac{\sqrt{2}}{2} & \frac{\sqrt{2}}{2} & & \\ & & -i\frac{\sqrt{2}}{2} & i\frac{\sqrt{2}}{2} & & \\ & & & & \frac{\sqrt{2}}{2} & \frac{\sqrt{2}}{2} \\ & & & & -i\frac{\sqrt{2}}{2} & i\frac{\sqrt{2}}{2} \end{bmatrix} \tag{4.3}$$

After mathematical manipulation, Eq. 4.1 becomes

$$D^{-1}\Sigma(D^T)^{-1} = \{D^{-1}MD\}\{D^{-1}\Sigma(D^T)^{-1}\}\{D^T M^T (D^T)^{-1}\} + D^{-1}B(D^T)^{-1} \tag{4.4}$$

For simplicity,

$$\begin{aligned} \Lambda &= D^{-1}MD = D^{T}M^{T}(D^{T})^{-1} \\ Q &= D^{-1}B(D^{T})^{-1} \\ \sigma &= D^{-1}\Sigma(D^{T})^{-1} \end{aligned} \tag{4.5}$$

Then Eq. 4.4 is given by

$$\sigma = \Lambda\sigma\Lambda + Q \tag{4.6}$$

Because $\Lambda$ is

$$\Lambda = \begin{bmatrix} e^{-i\mu_1-\alpha_1} & & & & & & \\ & e^{i\mu_1-\alpha_1} & & & & & \\ & & e^{-i\mu_2-\alpha_2} & & & & \\ & & & e^{i\mu_2-\alpha_2} & & & \\ & & & & e^{-i\mu_3-\alpha_3} & & \\ & & & & & e^{i\mu_3-\alpha_3} \end{bmatrix} \tag{4.7}$$

where $\mu_1$, $\mu_2$, and $\mu_3$ are three tunes in horizontal, vertical, and longitudinal direction, $\alpha_1$, $\alpha_2$, and $\alpha_3$ are values of damping time in each direction. Due to the feature of diagonal matrix, the elements in $\sigma$ are calculated as

$$\sigma_{ij} = \frac{Q_{ij}}{\Lambda_{ii}\Lambda_{jj}} \tag{4.8}$$

It is assumed a ring does not operate near a integer, a half-integer or a coupling resonance and values of damping time are very small. Therefore, only $\sigma_{12}$, $\sigma_{21}$, $\sigma_{34}$, $\sigma_{43}$, $\sigma_{56}$, and $\sigma_{65}$ contribute to the $\sigma$ matrix and other components are nearly equal to zero.

$$\sigma_{i,i+1} = \sigma_{i+1,i} = \frac{Q_{i,i+1}}{2\alpha_i} = \varepsilon_i \qquad i = 1, 2, 3 \tag{4.9}$$

where $\varepsilon_i$ is the equilibrium emittance in each plane. The right part of Eq. 4.4 is

$$(AC)^{-1}\Sigma(C^T A^T)^{-1} = \begin{bmatrix} & \varepsilon_1 & & & & \\ \varepsilon_1 & & & & & \\ & & & \varepsilon_2 & & \\ & & \varepsilon_2 & & & \\ & & & & & \varepsilon_3 \\ & & & & \varepsilon_3 & \end{bmatrix} \tag{4.10}$$

It can be proved that a natural bunch distribution in a ring can be generated by three equilibrium emittances and decoupling matrix $A$. If the one-turn matrix $M$ is symplectic, the decoupling matrix $A$ is also nearly symplectic, which satisfies

$$A^T S A = S \tag{4.11}$$

where $S$ is a $6 \times 6$ symplectic matrix given by

$$S = \begin{bmatrix} & 1 & & & & \\ -1 & & & & & \\ & & & 1 & & \\ & & -1 & & & \\ & & & & & 1 \\ & & & & -1 & \end{bmatrix} \tag{4.12}$$

Based on Eq. 4.3, Eq. 4.6, and Eq. 4.11, a new equation is

$$\Sigma = (A)diag(\varepsilon_1, \varepsilon_1, \varepsilon_2, \varepsilon_2, \varepsilon_3, \varepsilon_3)(A^T) \tag{4.13}$$

From Eq. 4.13, it can also be found that

$$(AC)^{-1}\Sigma S(AC) = diag(-i\varepsilon_1, i\varepsilon_1, -i\varepsilon_2, i\varepsilon_2, -i\varepsilon_3, i\varepsilon_3) \tag{4.14}$$

Therefore, the matrix $D$ can diagonalize not only the one turn matrix $M$ but also $\Sigma S$.

It is trivial to generate a normalized beam distribution without coupling, which satisfies

$$\Sigma_{nor} = diag(\varepsilon_1, \varepsilon_1, \varepsilon_2, \varepsilon_2, \varepsilon_3, \varepsilon_3) \tag{4.15}$$

if the particle number is $N$, the quadratic moments of normalized beam distribution are given by

$$\langle v_a v_b \rangle = \frac{1}{N} \sum_{i=1}^{N} (v_a^{(i)} v_b^{(i)}) \tag{4.16}$$

Then the $A$ acts on motions of each particle, a new distribution is given by

$$(\langle v_a v_b \rangle)_{new} = \frac{1}{N} \sum_{i=1}^{N} \sum_{c,d} (A_{ac} v_c^{(i)} A_{bd} v_d^{(i)}) \tag{4.17}$$

Finally, the new beam distribution is

$$\Sigma_{new} = A \Sigma_{nor} A^T \tag{4.18}$$

Eq. 4.18 is consistent with Eq. 4.13, which proves that the $\Sigma_{new}$ in Eq. 4.18 is a stored bunch distribution in a ring.

### 4.1.2 Simulation of the Stored Beam Oscillation

The natural stored bunch distribution at the injection point is computed in SAD. The equilibrium beam distribution matrix at the injection point of the PF ring can be is given by

$$\begin{bmatrix}
6.4416\text{E}{-7} & & & & & \\
5.7233\text{E}{-8} & 8.5778\text{E}{-9} & & & & \\
-1.83\text{E}{-19} & -6.61\text{E}{-21} & 1.319\text{E}{-34} & & & \\
-1.48\text{E}{-19} & -1.22\text{E}{-20} & 6.632\text{E}{-35} & 3.681\text{E}{-35} & & \\
-6.430\text{E}{-8} & -3.21\text{E}{-10} & 1.790\text{E}{-19} & 1.344\text{E}{-19} & 8.0394\text{E}{-5} & \\
3.5914\text{E}{-7} & 1.8380\text{E}{-8} & -1.53\text{E}{-19} & -1.02\text{E}{-19} & -1.213\text{E}{-8} & 5.3827\text{E}-8
\end{bmatrix}$$

From SAD, the horizontal emittance is $3.455 \times 10^{-8}$ m $\cdot$ rad, vertical emittance is $3.194 \times 10^{-35}$ m $\cdot$ rad, and longitudinal emittance is $6.577 \times 10^{-6}$ m. Therefore, the

normalized beam distribution satisfies:

$$\begin{aligned} < X^2 > =< P_x^2 >= \varepsilon_x \\ < Y^2 > =< P_y^2 >= \varepsilon_y \\ < Z^2 > =< \triangle^2 >= \varepsilon_z \\ < V_i V_j > = 0 \quad (i \neq j) \end{aligned} \tag{4.19}$$

where $V = (X, P_x, Y, P_y, Z, \triangle)$ are six variables in a normalized phase space.

A Gaussian distribution was used to produce the array to represent particle motions in normalized phase space. A normalized bunch distribution was generated in SAD, which is shown in Fig. 4.1.

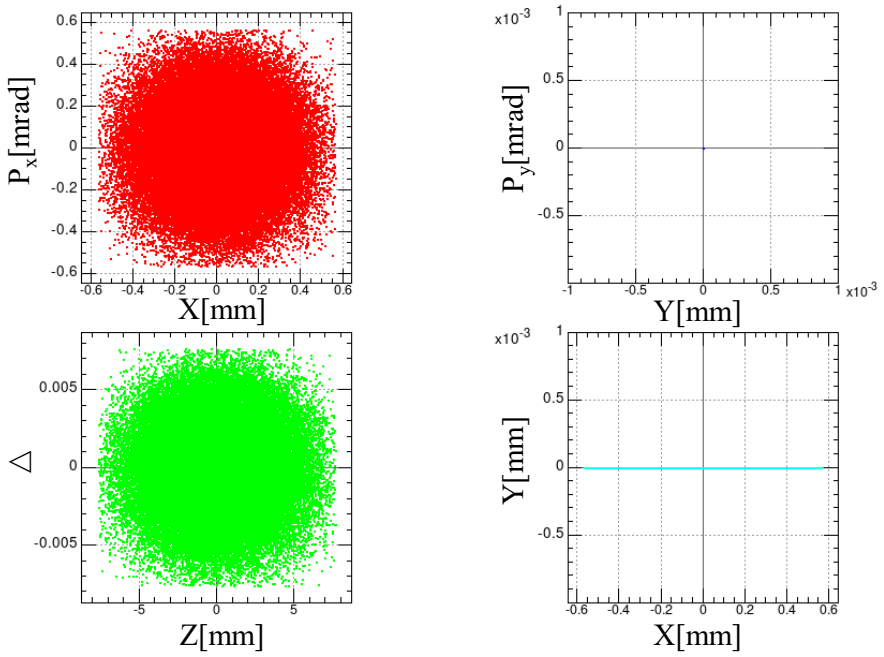


FIGURE 4.1: A normalized natural bunch distribution at injection point.

The number of particles is 100000. The vertical phase space only contains one point due to a zero vertical emittance. Because in beam envelope calculation, there is no quantum fluctuation components in vertical direction if the closed orbit does not have a vertical distortion. In addition, space charge effect is also ignored.

From the beam distribution at the injection point, one decoupling matrix $A$ can be found. Then the $A$ acts on particle motions on the normalized phase plane, which is given by

$$\begin{bmatrix} x \\ p_x \\ y \\ p_y \\ z \\ \delta \end{bmatrix} = \begin{bmatrix} 3.42 & 0 & 0 & 0 & -3.5\text{E}{-3} & 0.19 \\ 0.38 & 0.29 & 0 & 0 & -1.7\text{E}{-4} & 9.7\text{E}{-3} \\ 0 & 0 & 0 & 0 & 0 & 0 \\ 0 & 0 & 0 & 0 & 0 & 0 \\ 0.136 & 0.195 & 0 & 0 & 3.50 & 0 \\ -1\text{E}{-7} & 1.7\text{E}{-6} & 0 & 0 & -5.3\text{E}{-3} & 0.29 \end{bmatrix} \begin{bmatrix} X \\ P_x \\ Y \\ P_y \\ Z \\ \triangle \end{bmatrix} \tag{4.20}$$

After the transformation, a natural bunch distribution in the real space is shown in Fig. 4.2.

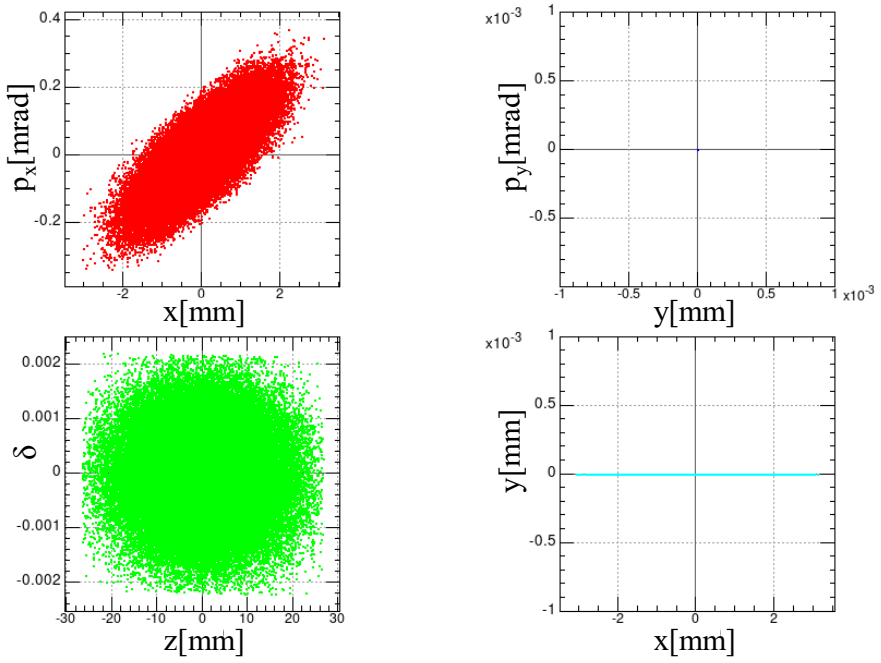


FIGURE 4.2: A natural bunch distribution at the injection point.

Then the perturbation is calculated from the measurement result, and it is assumed that the PMM injection is a one-turn kick, the perturbation from the pulsed magnet will only influence the stored beam at the first turn. The perturbation in PSM1 injection is calculated from previous magnetic field result. If the peak magnetic pulsed field in Fig. 3.19 is normalized under the condition of the designed current (3000 A), the integrated magnetic field is 1.17 mT · m. It is assumed that the magnetic field is uniform around the center, which is treated as a dipole kick in simulation. The strength parameter of a dipole magnet defined in SAD is given by

$$K_0 = \frac{BL}{B_0\rho} = \frac{0.3}{P[\text{GeV/c}]} B[\text{T}]L[\text{m}] \tag{4.21}$$

where $B_0\rho$ is the magnetic rigidity, $P$ is the momentum of the particle, $L$ is the length of the magnet, and $B$ is the magnetic field strength. Therefore, $BL$ is equal to the integrated magnetic field.

The natural bunch was tracked and received the kick from PSM1 at the first turn. The stored beam was observed in the tracking at the BPM33 in which is the upstream of the Undulator-16. The layout is show in Fig. 4.3

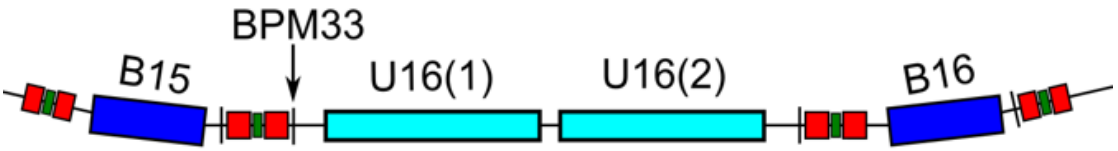


FIGURE 4.3: Optics layout around Undulator-16 of the PF ring.

The centroid of the beam is observed until 50th turn, which is calculated as

$$\bar{x} = \frac{\sum(x_i - x_0)}{N} \tag{4.22}$$

where $x_0$ is the closed orbit at the BPM33, $x_i$ is the position of one single particle, and $N$ is the particle number.

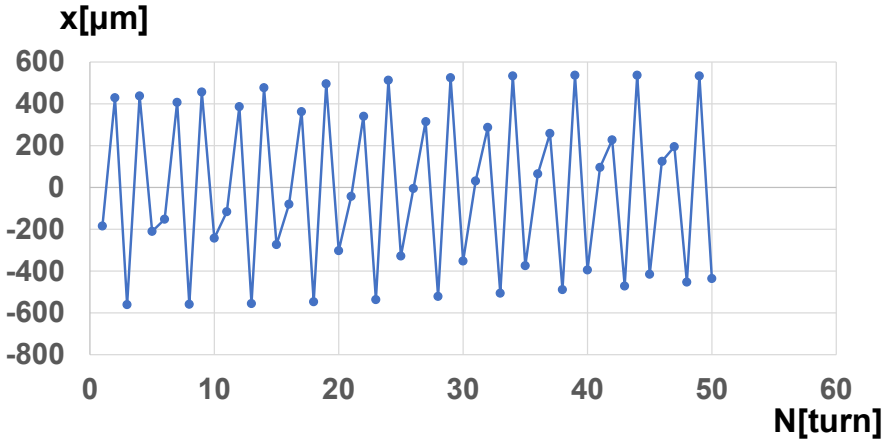


FIGURE 4.4: Horizontal beam oscillation at the BPM33.

As shown in Fig. 4.4, the oscillation amplitude is 560 μm, which is consistent with the measurement result (570 μm) observed in the one-turn kick injection. Therefore, it is concluded that the eddy current effect of the iron-core results in the stored beam oscillation in the PSM1 injection.

## 4.2 Eddy Current Effect of Coating in Different Magnets

In previous measurement of PSM1, the eddy current effect of the titanium coating hardly influences the pulsed magnetic field on the stored beam orbit. From the analysis in previous section, the eddy current effect of iron core can generate horizontal stored beam oscillation with an amplitude of several hundred micrometers. But the stored beam oscillation reached to 4 mm in the PSM2 injection. Therefore, the eddy current effect of the lamination steel is not the primary reason. To understand previous experiment results, the eddy current effects of the titanium coating in the PSM1, PSM2 and nonlinear kicker are examined by simulation.

The eddy current effect can be simulated with ELF/MAGIC [49]. It is a software based on boundary element method. ELF/MAGIC is not capable of defining an anisotropic material so that the eddy current effect of lamination steel cannot be simulated. In the simulation, the iron core is defined by a magnetic element without conductivity. Only the eddy current effect of titanium coating is examined in the simulation. The titanium coating is defined by a conductive material whose resistivity is $4.2 \times 10^{-8}\ \Omega \cdot \mathrm{m}$.

As shown in Fig. 4.5, the model of PSM1, PSM2 and a nonlinear kicker are constructed in ELF/MAGIC. The conductor model is a cuboid, not a cylinder that corresponds to real model, because it is difficult to create a circular element in the software. The specific color of conductor represents different current flow direction. For simplicity, the busbar structure is ignored in the simulation. The B-H curve of the lamination steel is shown in Fig. 4.6. The data is loaded by processor of ELF/MAGIC. As for the nonlinear kicker, it is an air-core magnet and does not have iron core. The coating of PSM1 is a circular shape. The PSM2 and nonlinear kicker have a rectangular coating. Thickness is set as 5 µm.

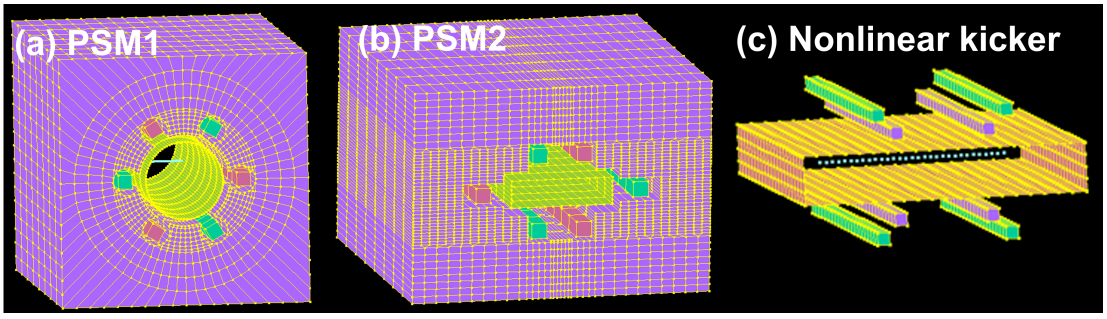


FIGURE 4.5: Magnet models in ELF/MAGIC. (a) PSM1. (b) PSM2. (c) Nonlinear kicker.

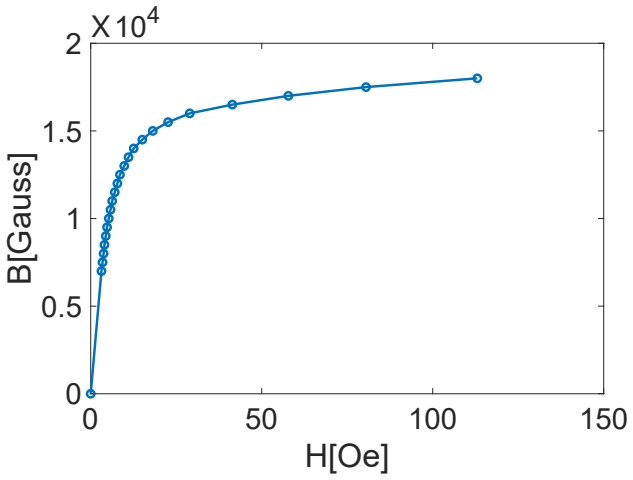


FIGURE 4.6: B-H curve of lamination steel.

The applied current in the simulation is a half-sine pulse shape, and the peak value is 3000 A, which is shown in Fig. 4.7. The pulse width is 1.2 µs and consists of 20 steps. The total number of simulation step is 30.

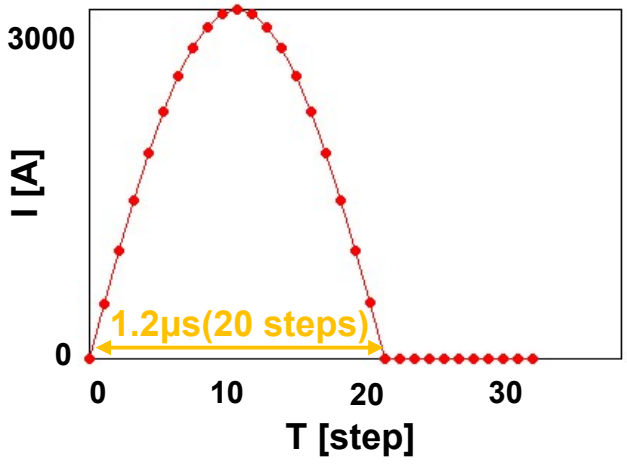


FIGURE 4.7: Applied current in the simulation.

Time evolution of the $B_y$ at the center is observed in the simulation. The magnetic field without coating is compared with that with coating to examine the eddy current effect.

From the time evolution of the $B_y$ in PSM1 at $x$=0 mm shown in Fig. 4.8, the magnetic field remained zero at the center after adding the coating. The simulation result is consistent with the measurement in Fig. 3.25 that showed the circular coating hardly influences the magnetic field inside PSM1. It may be because that the shape of the coating is symmetric; thus, the magnetic field generated by the eddy current of the titanium coating is compensated at the center.

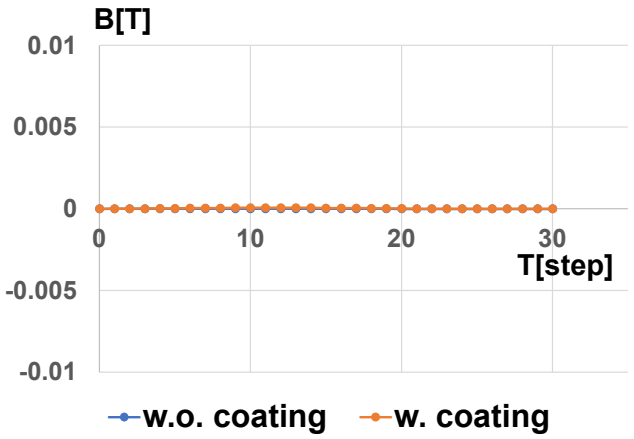


FIGURE 4.8: Time evolution of $B_y$ in PSM1 at $x$=0 mm.

As for the result of PSM2 and nonlinear kicker, they both have a rectangular coating, but the eddy current effect of the coating is different. Fig. 4.9 (a) shows that there is a peak pulsed magnetic field that is about -0.01 T at the center. In the measurement of the PSM1 shown in Fig. 3.19, the eddy-current magnetic field is $1.2 \times 10^{-4}$ T at the center when the peak pulsed current is 180 A. After normalizing the value under the condition of a 3000 A current, the eddy-current magnetic field is $2 \times 10^{-3}$ T. The strength of the peak magnetic field generated by the titanium coating in PSM2 is five times as much as the magnetic field generated by lamination steel in the measurement. Therefore, the titanium coating in rectangular shape is the main reason that induced a 4 mm stored beam oscillation in the PSM2 injection.

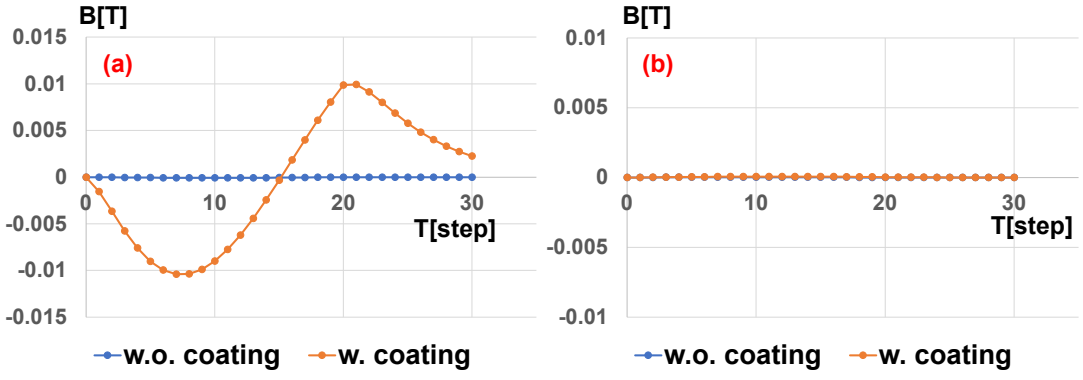


FIGURE 4.9: Time evolution of $B_y$ at $x$=0 mm. (a) PSM1. (b) Nonlinear kicker.

As shown in Fig. 4.9 (b), magnetic field does not appear at the center of the nonlinear kicker after adding the titanium coating. Therefore, there was no problem of the stored beam oscillation in the experiment of nonlinear kicker.

TABLE 4.1: Eddy-current magnetic fields generated by the coating at $x$=0 mm.

| Magnet | Peak value of $B_y$[T] |
|---|---|
| PSM1 | 0 |
| PSM2 | $1.2 \times 10^{-4}$ |
| Nonlinear kicker | 0 |

The eddy-current magnetic fields generated by several coatings are shown in Table 4.1 According to the simulation and experimental results, the eddy current effect of the rectangular coating is closely related to the order of the magnetic field. If the transverse magnetic field in the midplane is symmetric like the sextupole field, the eddy current effect of the coating generates large magnetic field distortion at the center. If it is antisymmetric like the quadrupole or octupole fields, then the effect is negligible.

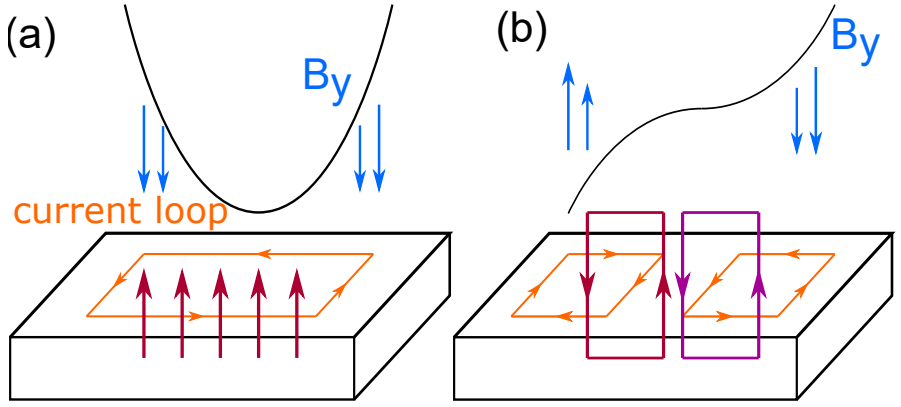


FIGURE 4.10: Schematic view of the eddy current effect of an rectangular coating. (a)Sextupole magnetic field. (b) Octupole magnetic field.

The phenomenon can be understood by a schematic view. In Fig. 4.10 (a), the external magnetic field is sextupole magnetic field. A big eddy-current loop is generated on the surface of a rectangular coating. An undesirable magnetic field is present at the center. However, the external magnetic field is octupole magnetic field in Fig. 4.10 (b). The direction of the eddy-current loop is different on each side of the coating. The eddy-current magnetic fields are compensated at the center.

However, if we choose a circular chamber, the magnetic field at the center is not distorted no matter what kind of multipole field is present.

## 4.3 Requirements for the Pulsed Magnet

The perturbation on stored beam is analyzed by the previous measurement and simulation. Estimations from our measurement show that the eddy current effect of the lamination steel cannot induce a stored beam oscillation in PF ring with an amplitude of 4 mm. However, in PSM2 injection experiment, a large stored beam oscillation was observed, which was possibly due to the eddy current effect of the rectangular coating. To better understand the impact of coating, the eddy current effects of coating in PSM1, PSM2, and the nonlinear kicker model were simulated with ELF/MAGIC. The simulation results show that the eddy current effect of the titanium coating is not only associated with the shape but also the type of magnetic field, which is summarized in Table 4.2. On the basis of the previous researches, the experimental results of different pulsed magnet can be understood.

TABLE 4.2: Eddy current effect of titanium coating related to the shape and magnet.

| | **Magnet order** | |
|---|---|---|
| **Titanium coating** | Odd (e.g. Quadrupole) | Even (e.g. Sextupole) |
| Circular shape | Negligible | Negligible |
| Rectangular shape | Negligible | Large |

From our research, if PMM injection is applied in next generation light source, an air-core pulsed magnet should be used as a suitable design because of the eddy current effects of the iron core. The design of the busbar structure should also be considered carefully. As for the chamber, if it is a circular shape, the eddy current effect of the titanium coating is trivial and magnetic field distortion does not arise along the center axis because of the compensation. However, to expand the horizontal physical aperture, sometimes a rectangular chamber is preferred. In this case, the transverse magnetic field in the midplane must be antisymmetric for magnetic field distortion not to appear at the center. An octupole magnetic field is superior because a quadrupole magnet cannot give a nearly zero region around the center and a magnet with higher order is hard to design.

In Appendix C, the perturbation on the stored beam in the PF ring by different pulsed magnet is discussed by a simulation. It shows that a Pulsed Octupole Magnet (POM)

is superior compared with a PQM or PSM and has a possibility to realize a transparent injection.

# Chapter 5

# Ceramics Chamber with Integrated Pulsed Magnet

It is concluded that air-core pulsed magnet is superior for PMM injection in next generation light source. In this chapter, an air-core pulsed magnet named Ceramics Chamber with Integrated Pulsed Magnet (CCiPM) is introduced, which has a potential application for PMM injection.

## 5.1 Introduction of CCiPM

Conventional iron-core pulsed dipole kicker has some disadvantages such as a limitation of repetition rate, eddy current induced by iron core and internal coating, saturation effect of the magnetic field in magnet pole and so on. An air-core type magnet has a possibility to solve these problems. The development of CCiPM was conducted as a new air-core magnet for fast dipole kicker [50]. The structure of CCiPM is very compact and simple, which has only three parts: a cylindrical ceramics chamber, copper conductor, and flanges. Fig. 5.1 shows the design figure of a CCiPM.

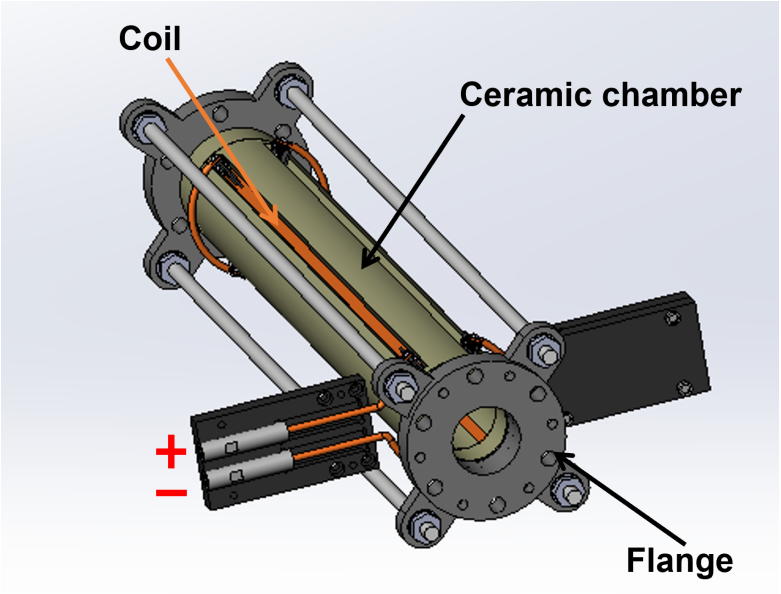


FIGURE 5.1: Design figure of CCiPM as a dipole kicker.

The four copper conductors are embedded in the ceramic chamber. Small metal blocks are brazed at the end of the conductors. Then the current direction can be arranged easily by the arc conductor, and a closed loop can be made. if the direction and position of the current flow are designed properly, different magnetic field can be generated.

The overview of CCiPM has been introduced. Then some detailed information is explained for the components of CCiPM. The special characteristic of CCiPM is the embedment of the coil. There are two proposals for embedding the coil. As shown in Fig. 5.2 (a), there is a groove to hold down the coil, which is similar with the design of a nonlinear kicker. In this case, a high vacuum tightness of the chamber can be achieved. To obtain a mechanical strength of the ceramic, the thickness of the ceramic is 10 mm. It indicates that the distance between the coil and center becomes longer. Therefore, the design is not easy to generate a strong magnetic field. The other proposal is shown in Fig. 5.2 (b), which is chosen for the CCiPM. A hole is dug through the ceramic. The coil and ceramic are welded by brazing, which keeps a vacuum seal for the chamber. In this design, the coil can be as near as possible to the center. The magnetic field can be stronger. However, the design has some challenges. The vacuum tightness mainly depends on the quality of the brazing between the coil and ceramic. The component that determines the mechanical strength is not the thickness of the ceramic but the coil.

The material of the coil is oxygen-free copper with a excellent electrical conductivity.

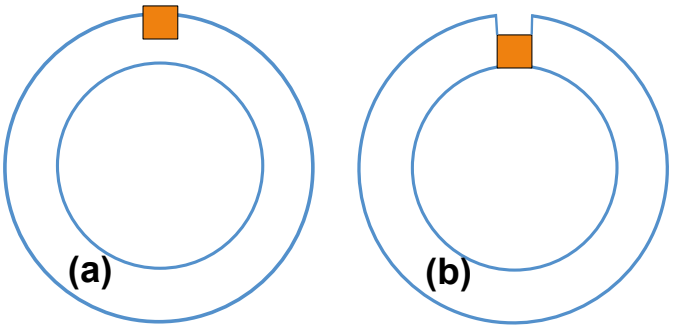


FIGURE 5.2: Proposals for embedding the coil. (a) A groove to hold the coil. (b) Dig through the ceramic, and combine the coil with the ceramic by brazing process.

Because of the high temperature during the brazing, the oxygen-free copper can be free from hydrogen embrittlement. The brazing process for the ceramic and coil used silver brazing that has a melting point around 800 °C.

During the brazing with a high temperature, the shape of the ceramic and coil may change because of the thermal expansion. The linear thermal expansion coefficients of ceramic and oxygen-free copper are $7.2 \times 10^{-6}$ m/(m °C) and $17.0 \times 10^{-6}$ m/(m °C), respectively. Because the length of the coil embedded in the ceramic is 324 mm, the difference between the length of the coil and ceramic can reach to 2.5 mm during the brazing. Therefore, there are residual stresses in the ceramic-metal assembly after the brazing process. The coil's shape should be considered carefully to reduce the residual stress and have an enough brazing area.

As shown in Fig. 5.3, there are two models of the coil's shape. The coil that has a sector shape can release the residual stress from the analysis [51]. However, it is very hard to cut such a hole for the ceramic because of the 10 mm thickness. From the aspect of manufacturing, the coil of the CCiPM is rectangular shape. If the thickness of the ceramic can be reduced to 5 mm, the sector shape can be used.

To change the current direction, the joint between the coil and lead wire should be designed. Figure 5.4 shows the schematic view of the CCiPM's joint. The metal block and coil are brazed together. The round copper bar is fixed on the metal block by the bolt, which has a strong mechanical strength. Otherwise, if there is a gap between the bar and metal block induced by some external forces, an electrical breakdown may easily occur and cause damage to the joint. The length between the two joints is 290 mm. Because the residual stress is strong at the end of the coil, which may deform the joint, the position of the joint is not located at the end of the coil. It brings a disadvantage

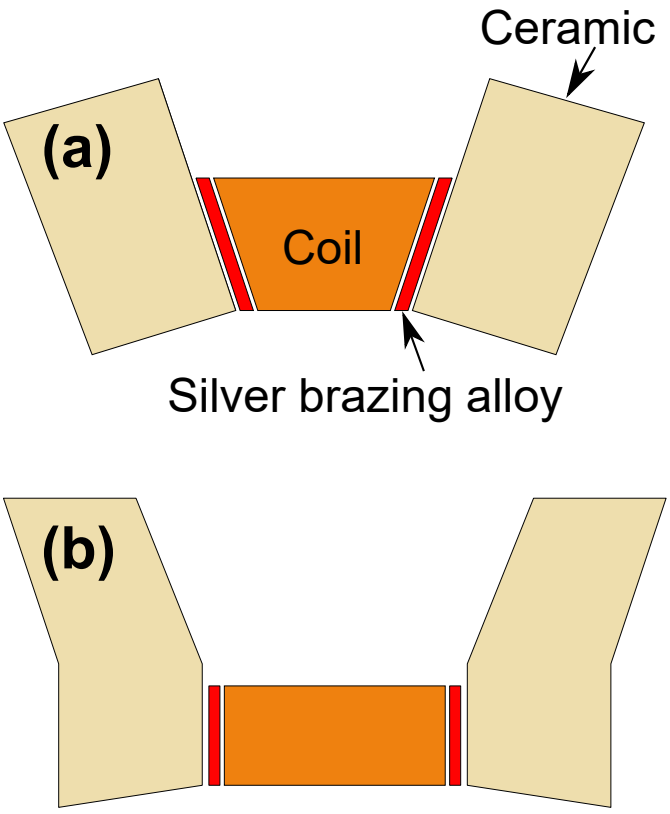


FIGURE 5.3: Cross-sectional views of the coil. (a) Sector shape. (b) Rectangular shape.

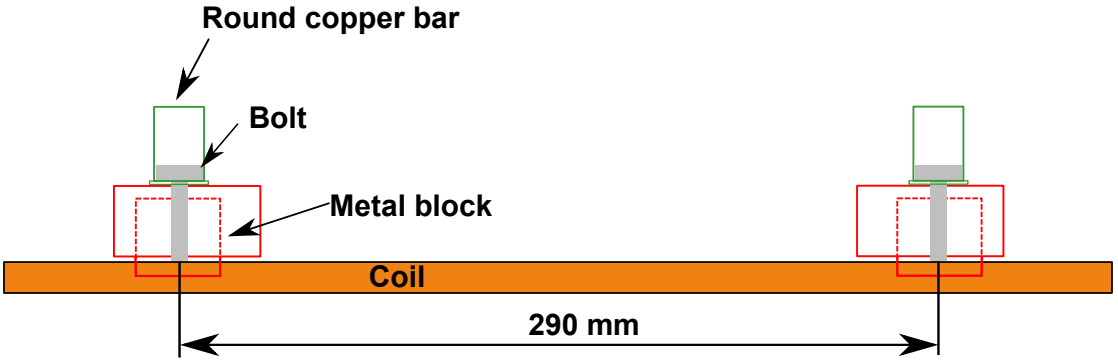


FIGURE 5.4: Schematic view of the CCiPM's joint for the lead wire.

that the effective length of the magnet is reduced. For the fabrication of the CCiPM, such a design is selected after long research and development process.

Another characteristic of CCiPM is that a novel titanium coating technology has been developed for the internal coating to reduce the eddy current effect. The coating shape is like a comb, which is shown in Fig. 5.5. There is a space between two pieces of the coating, whose minimum width is 1 mm.

If an external pulsed magnetic field penetrates the coating, several eddy current loops can be generated in each piece of the coating. As shown in Fig. 5.6, the eddy-current

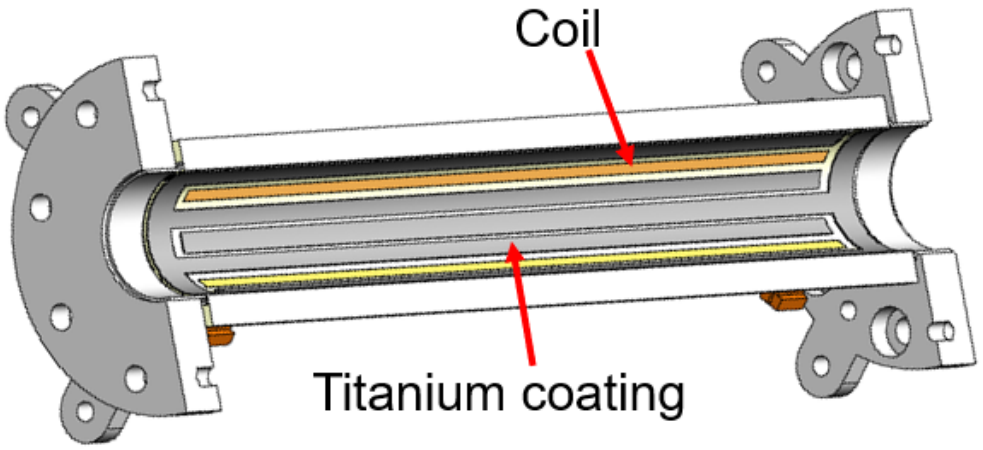


FIGURE 5.5: Comb titanium coating inside the chamber.

magnetic field in the loop is opposite to the external magnetic field. However, the direction of the eddy-current magnetic field in the gap is reverse. Due to the cancelling effect, the eddy current effect inside the chamber can be reduced.

In addition, because the stored beam keeps circulating in a ring, a wall current is present in beam pipe. The comb-shape coating is like a kind of capacitance structure and allows the wall current to flow through the chamber.

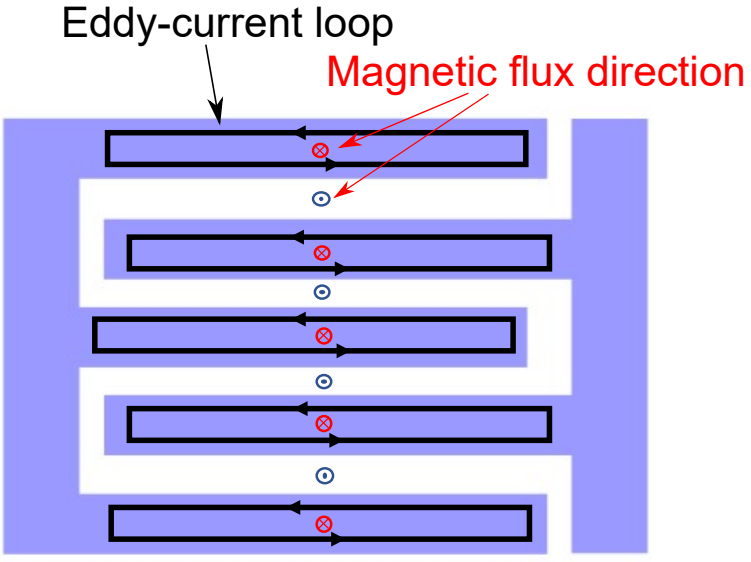


FIGURE 5.6: Section view of the comb coating with some eddy-current loops.

Some basic parameters of a CCiPM are summarized in Table 5.1.

TABLE 5.1: Basic parameters of a CCiPM .

| Item | Parameter |
|---|---|
| Total length | 399.4 mm |
| Length of the ceramic chamber | 357.0 mm |
| Thickness of the ceramic | 10.0 mm |
| Material of the ceramic | $Al_2O_3$ |
| Length of the coil embedded in the ceramic | 324.0 mm |
| Material of the coil | Oxygen-free copper |
| Weight | <6 kg |

## 5.2 Beam Test of Dipole CCiPM-D30 at PF-BT line

A prototype whose diameter of the bore is only 30 mm (CCiPM-D30) has been developed as a dipole pulsed kicker for the application in next generation light sources [52]. The cross-sectional view of CCiPM-D30 with magnetic flux is shown in Fig. 5.7. The current direction of each conductor is marked. For a dipole CCiPM, the included angle between the conductor and midplane is 30° for generating a dipole magnetic field. The experimental coordinate is marked to explain the measurement, and the origin is located at the center.

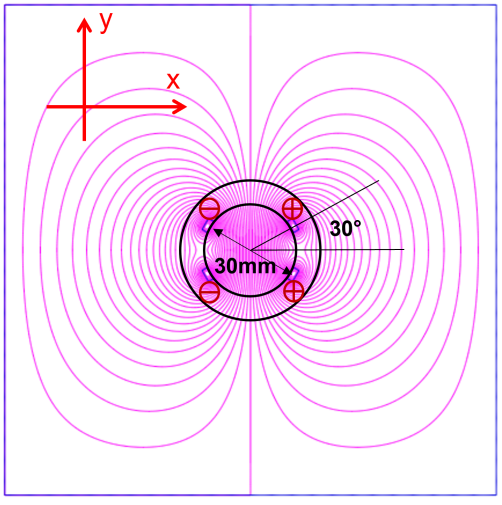


FIGURE 5.7: Cross-sectional view of CCiPM-D30 with magnetic flux.

To examine the performance of CCiPM-D30, some offline tests such as baking, current excitation test, and magnetic field measurement were conducted [53]. The vacuum reached to $3 \times 10^{-8}$ Pa, and any leakage did not occur. In the current excitation test,

the peak value of the pulsed current is 3180 A at a repetition rate of 10 Hz, and the pulse width is 3 µs. And there is no electric discharge in the experiment. The detail of the magnetic field measurement is introduced in Appendix D. Then CCiPM-D30 was installed at the BT-dump line of PF to evaluate the kick effect, which is shown in Fig. 5.8 [54]. The twisted cable was used to change the current flow direction and reduce the impedance of the whole model. From the measurement of LCR meter, the inductance of CCiPM-D30 is 1.33 µH, and the resistance is 0.51 Ω. It is noted that twisted cable is used to reduce the impedance of the circuit.

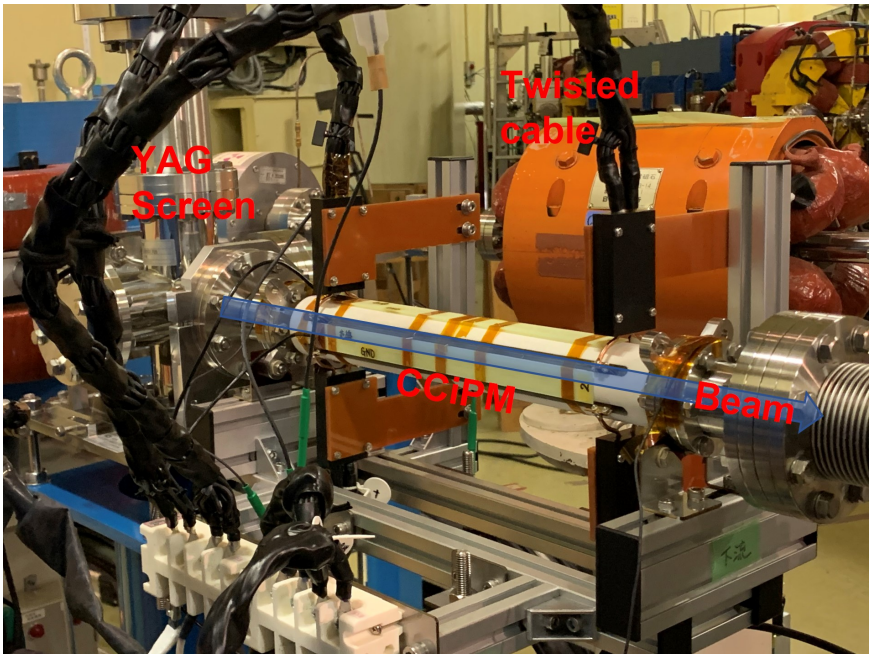


FIGURE 5.8: Installation of the CCiPM at the BT-dump line.

The layout of the BT-dump line at PF is shown in Fig. 5.9. In the beam test, the trajectory of the injection beam was adjusted by the strength of BH31, BH32, and BH41 (BH: bending magnet in horizontal direction) to be parallel with the CCiPM. Two Beam Position Monitors (BPM) were installed at the upstream and downstream of CCiPM-D30 to observe the beam profile. The BPMs were screen monitors using Yttrium Aluminum Garnet (YAG). In general, the resolution of YAG is 100 µm [55]. The horizontal and vertical emittances of the injection beam are both 120 nm · rad. If the beam has a Gaussian distribution, the beam size is expected to be 346 µm. Therefore, the YAG screen can satisfy the measurement requirement.

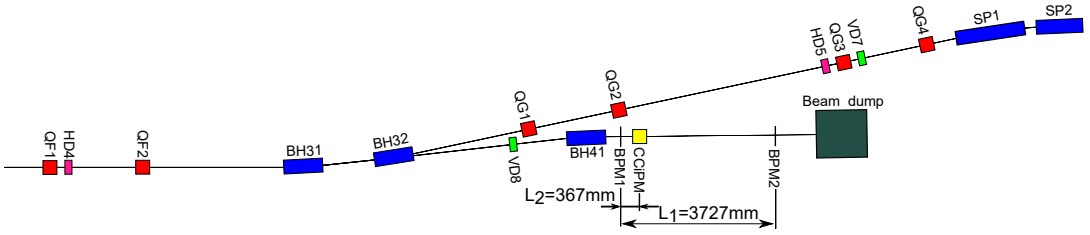


FIGURE 5.9: Layout of BT-dump line at PF.

The kick angle was estimated with the centroid of the beam profiles. The initial injection angle $\theta_0$ is calculated as

$$\theta_0 = \frac{x_2 - x_1}{L_1} \tag{5.1}$$

where $x_1$ is the beam centroid in BPM1, $x_2$ is the beam centroid in BPM2, and $L_1$ is the distance between two monitors. As shown in Fig. 5.10, the beam centroids measured by two monitors are almost the center of the screen. Therefore, the initial injection angle is almost zero.

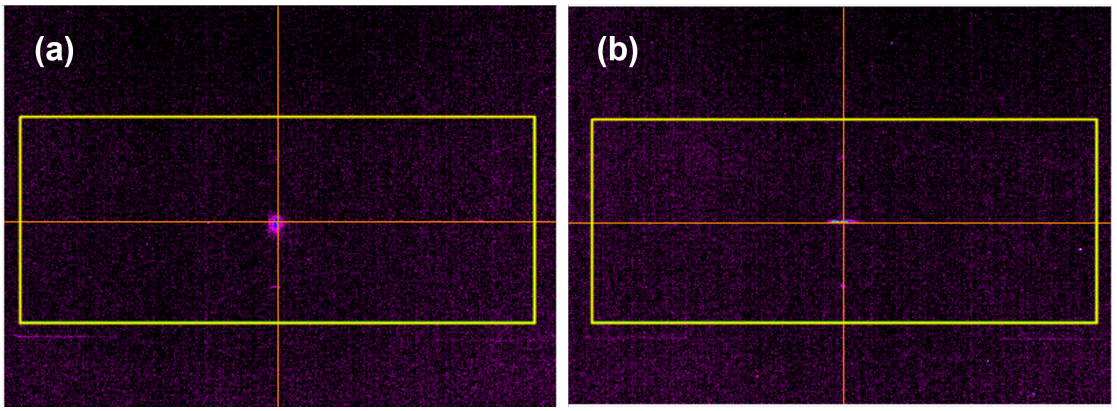


FIGURE 5.10: Beam profiles before kicking the beam. (a) BPM1. (b) BPM2.

After the excitation of the CCiPM, the beam had a deviation from the beam profile of the BPM2. A beam profile of BPM2 after the kick is shown in Fig. 5.11. Then the trigger timing was scanned to find a maximum variation compared with the initial position without kick, which corresponded to the kick at the peak value of the output current. Then the trigger timing was fixed. The angle $\theta_1$ after kick is calculated as

$$\theta_1 = \frac{X_2 - (x_1 + \theta_0 L_2)}{L_1 - L_2} \tag{5.2}$$

where $X_2$ is the beam centroid in BPM2 after kick, $L_2$ is the distance between BPM1 and the center of CCiPM-D30.

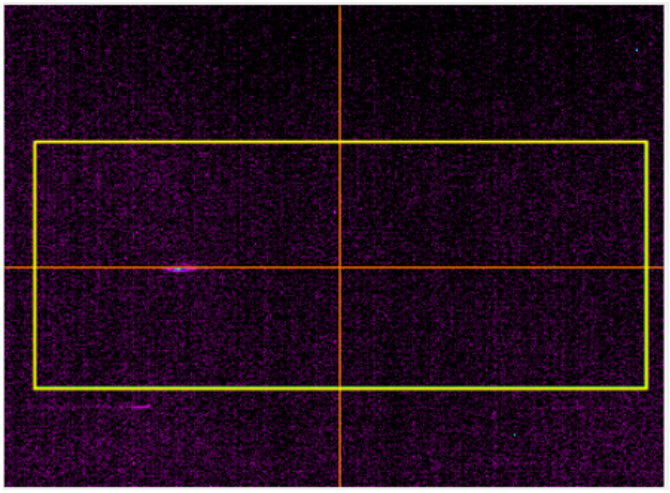

FIGURE 5.11: A beam profile of the monitor02 after kicking the beam.

It is assumed that the property of the injection beam is stable in the measurement. Finally, the kick effect of CCiPM is given by

$$\text{Kick Effect} = \frac{\theta_1 - \theta_0}{I} \tag{5.3}$$

where $I$ is the peak value of the output current monitored by a CT.

In the measurement, the repetition errors of two beam profiles were taken into the calculation. The fluctuation of the current value was also corrected by the CT. As for the beam jitter from the LINAC, it was observed by a beam position monitor in front of BPM1.

Comparison of the kick effect between the offline measurement and beam test is shown in Fig. 5.12. The beam test result has a good agreement with the offline measurement data which is calculated from the longitudinal magnetic field distribution of the CCiPM-D30. Fig. 5.13 shows the kick effect at the center that is 0.0014 mrad/A from the fitting curve. If the fitting error is taken into consideration, the difference of kick effect between beam test result and DC offline measurement is less than 3%.

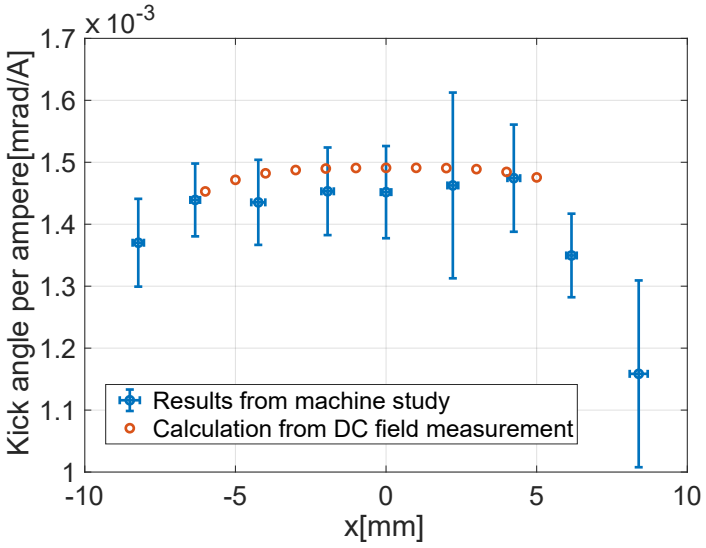


FIGURE 5.12: Kick effect survey of the CCiPM-D30.

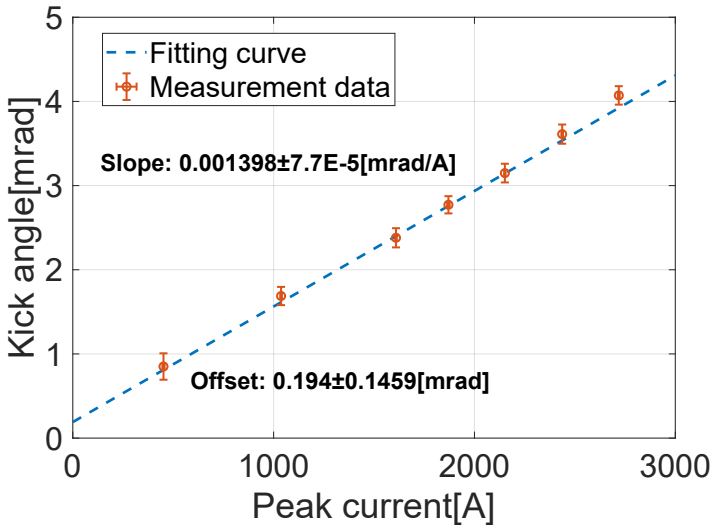


FIGURE 5.13: Kick effect at the center.

In the experiment, the current direction of CCiPM-D30 was also adjusted to generate a multipole magnetic field. If the current directions in four conductors are same, the CCiPM can generate a nearly quadrupole magnetic field. The cross-sectional view of the quadrupole CCiPM-D30 with magnetic flux is shown Fig. 5.14.

The horizontal survey for the quadrupole CCiPM-D30 was also conducted. Comparison of the kick effect between the simulation result and beam test is shown in Fig. 5.15. The result in beam test shows a clear distribution that is consistent with the simulation result. It encourages us that CCiPM may be used as a multipole pulsed magnet for

PMM injection. Because CCiPM has a flexibility of magnetic field generation, which can be explained by the design of air-core magnet.

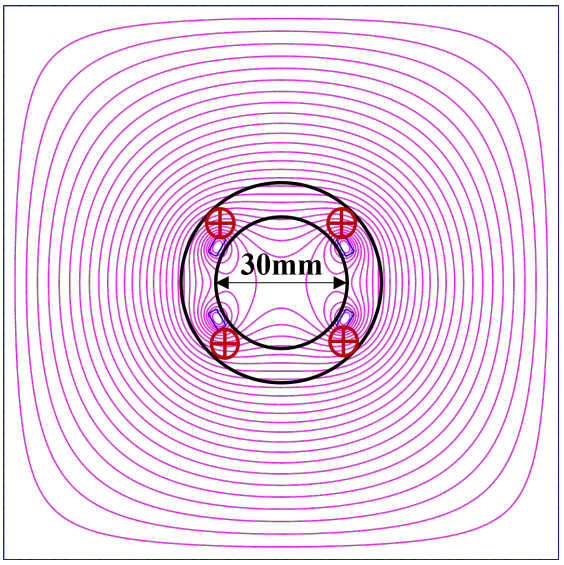


FIGURE 5.14: Cross-sectional view of the quadrupole CCiPM-D30 with magnetic flux.

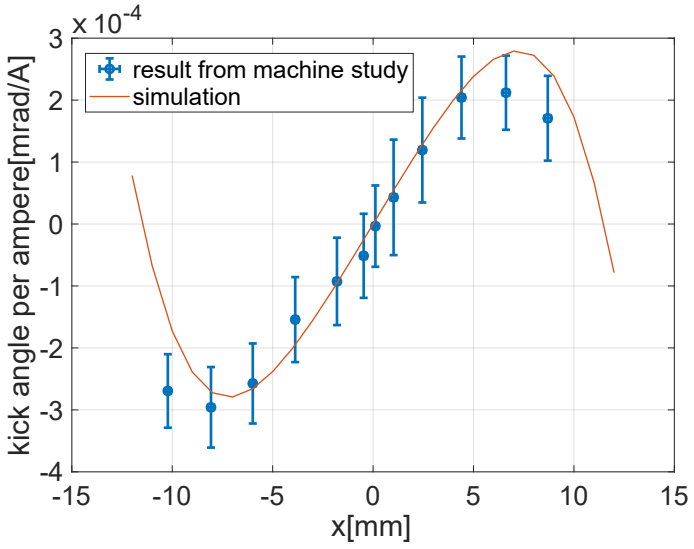


FIGURE 5.15: Quadrupole kick effect of the CCiPM.

## 5.3 Magnetic Field Generated by Air-core Magnet

In this section, the principle of the magnetic field in an air-core magnet is described, which is different from the content in Sec. 2.1. It is usually applied in superconducting magnet [56]. This section gives fundamental information of designing a CCiPM that can generate not only dipole magnetic field but also multipole magnetic field.

As for the magnetic field in an accelerator magnet, the expression of an ideal transverse magnetic field can be given by

$$\boldsymbol{B(z)} = \sum_{n=1}^{+\infty} \boldsymbol{C}_n \left(\frac{\boldsymbol{z}}{r_0}\right)^{n-1} \tag{5.4}$$

where $\boldsymbol{B} = B_y + iB_x$, $\boldsymbol{C}_n = B_n + iA_n$, $\boldsymbol{z} = x + iy$, $r_0$ is reference radius pf magnetic field. $B_n$ and $A_n$ represents the strength of magnetic field for different components. $B_n$ is normal component with $2n$ pole, and $A_n$ is skew component with $2n$ pole.

Assuming there is a infinite line current in a polar coordinate, which is show in Fig. 5.16.

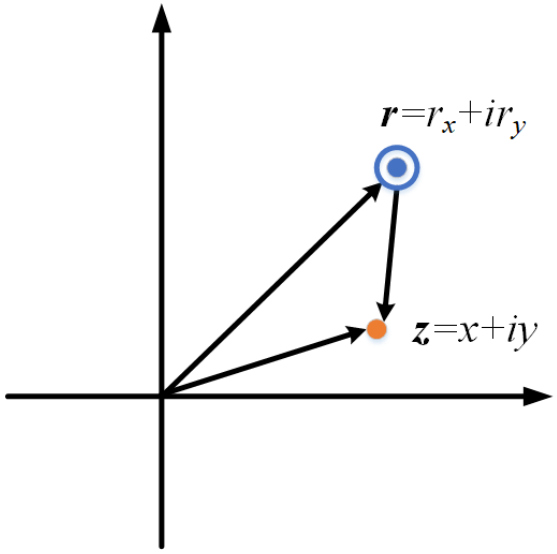


FIGURE 5.16: Infinite line current in polar coordinate.

According to Biot-Savart Law, the magnetic field at position $\boldsymbol{z}$ is given by

$$\boldsymbol{B(z)} = \frac{\mu_0 I}{2\pi(\boldsymbol{z}\text{-}\boldsymbol{r})} \tag{5.5}$$

where $\mu_0$ is the magnetic permeability in vacuum, $I$ is the current value. After applying Taylor expansion, a new equation is expressed as

$$\boldsymbol{B(z)} = \sum_{n=1}^{+\infty} -\frac{\mu_0 I}{2\pi \boldsymbol{r}} \left(\frac{\boldsymbol{z}}{\boldsymbol{r}}\right)^{n-1} \tag{5.6}$$

Comparing the new equation with Eq. 5.4, the magnetic field component $\boldsymbol{C}_n$ generated by the infinite line current is

$$\boldsymbol{C}_n = -\frac{\mu_0 I}{2\pi r_0}\left(\frac{r_0}{\boldsymbol{r}}\right)^n \tag{5.7}$$

In a curvilinear coordinate, $\boldsymbol{r} = re^{i\phi} = r(\cos\phi + i\sin\phi)$. If it is taken into Eq. 5.7, $\boldsymbol{C}_n$ is expressed as

$$\boldsymbol{C}_n = -\frac{\mu_0 I}{2\pi r_0}(\frac{r_0}{r})^n(\cos n\phi - i\sin n\phi) \tag{5.8}$$

According to Eq. 5.8, the magnetic field component generated by an infinite line current can be calculated easily. The reference radius $r_0$ is usually less than the radius of line current. If $r$ is much larger than $r_0$, the strength of high order magnetic field component will be weak. Besides, the normal component corresponds to the coefficient of $\cos n\phi$, and the skew component corresponds to the coefficient of $\sin n\phi$.

If there is a line current distribution $I = I_0\cos m\phi$ on a circle whose radius is $r$, the magnetic field component generated by the current distribution is calculated as

$$\boldsymbol{C}_n = -\int_{\phi=0}^{2\pi}\frac{\mu_0 I_0\cos m\phi}{2\pi r}\left(\frac{r_0}{r}\right)^2(\cos n\phi - i\sin n\phi)\mathrm{d}\phi \tag{5.9}$$

It is found that the integral is zero except for $n = m$. The magnetic field component is given by

$$\boldsymbol{C}_m = -\frac{\mu_0 I_0}{2r_0}\left(\frac{r_0}{r}\right)^n \tag{5.10}$$

Only a normal component exists, and the order is $2m$. Therefore, a line current distribution $I = I_0\cos m\phi$ can generate a pure normal magnetic field whose order is $2m$. Similarly, a line current distribution $I = I_0\sin m\phi$ can generate a pure skew magnetic field whose order is $2m$.

As shown in Fig. 5.17, dipole and quadrupole magnetic field can be generated inside of a $\cos m\phi$ current distribution. This principle is mainly applied to superconducting magnet. The magnetic field quality is highly related to the current distribution. Therefore, a superconducting magnet usually has several coil groups to have a desirable current distribution.

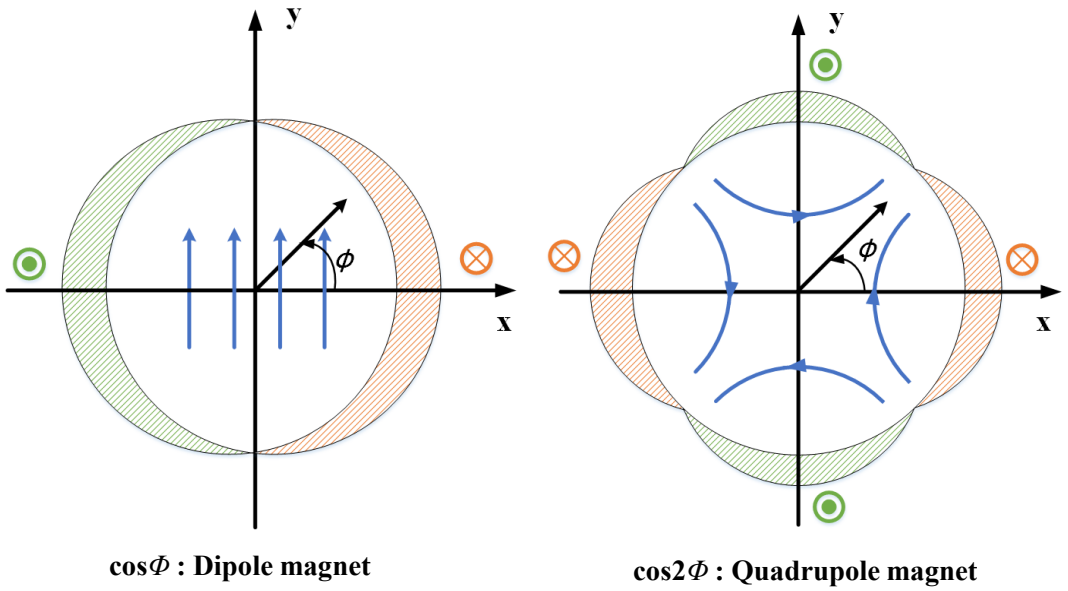


FIGURE 5.17: Dipole and quadrupole magnet from $I_0 \cos m\phi$ distributions.

## 5.4 An Octupole CCiPM for PMM Injection

The basic principle of air-core magnet reveals that CCiPM has a flexibility about the magnetic field order. The quadrupole CCiPM has been tested in the PF-BT line. Several cross-sectional views of CCiPM are shown in Fig. 5.18. Magnetic field with different order can be generated by specific current flow direction. It is noted that the magnetic field order is also related to the included angle between the conductor and midplane. In Fig. 5.18, the included angle is 45°, which is different from CCiPM-D30.

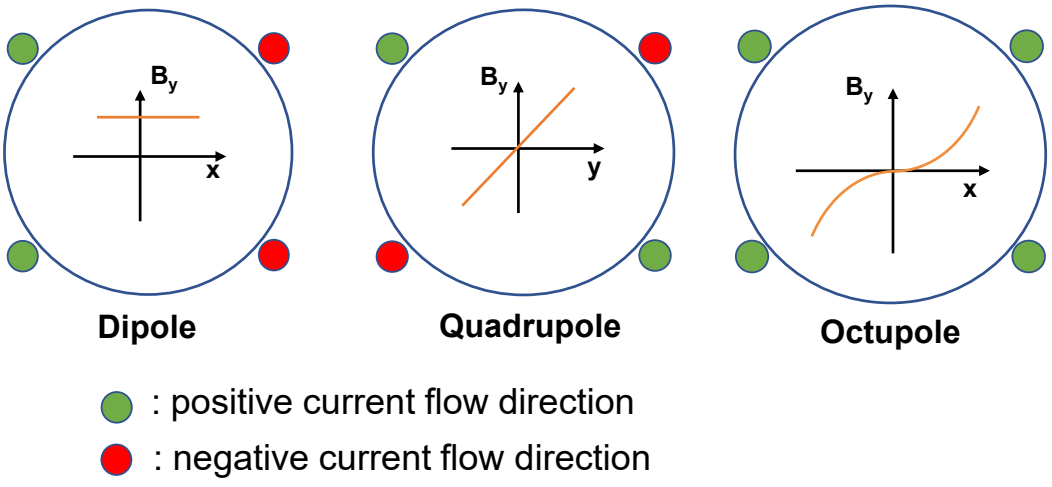


FIGURE 5.18: Different types of magnetic field generated by CCiPM.

If the current direction is same, a nearly octupole magnetic field can be generated, which indicates that CCiPM may be applied for PMM injection. The included angle between the conductor and the midplane is 45° which is most suitable for generating an octupole magnetic field. Although the current distribution is not consistent with the theoretical case that has a $I_0 \cos 4\phi$ distribution, an octupole magnetic field can be generated because of the narrow aperture.

If the bore diameter is small, the octupole CCiPM can have a strong off-axis magnetic field. However, the designed off-axis kick position is 15 mm. Therefore, an appropriate diameter of the octupole CCiPM is 40 mm to have a strong off-axis kick effect and avoid beam loss. Fig. 5.19 shows the cross-sectional view of the CCiPM with magnetic flux simulated with Poisson [57].

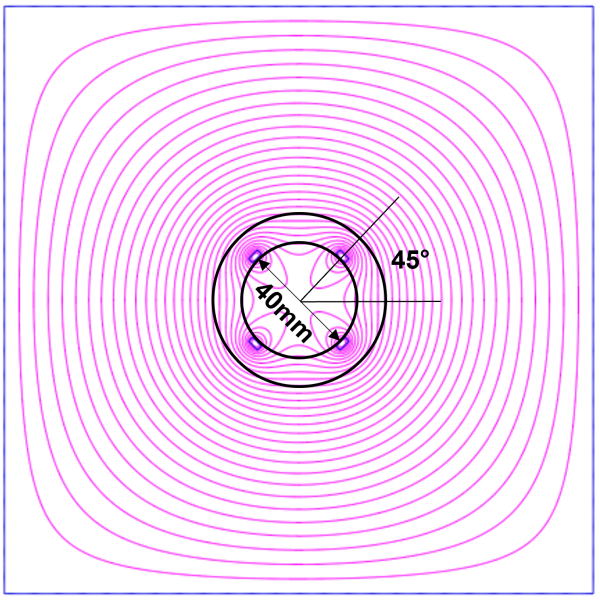


FIGURE 5.19: Cross-sectional view of the CCiPM with magnetic flux.

The transverse magnetic field in the midplane is compared with that generated by PSM1, which is shown in Fig. 5.20. The designed current of PSM1 is 3000 A and expected injection point is 15 mm. To achieve the similar kick effect of PSM1, the designed current of CCiPM should be 3750 A, which is 1.25 times larger than that of PSM1. Such a current can be supplied by a power source. As for the magnetic field around the center, the magnetic field of CCiPM is much smaller than that of PSM1, which indicates that perturbation on stored beam can be reduced. This is because of the nature of octupole magnetic field.

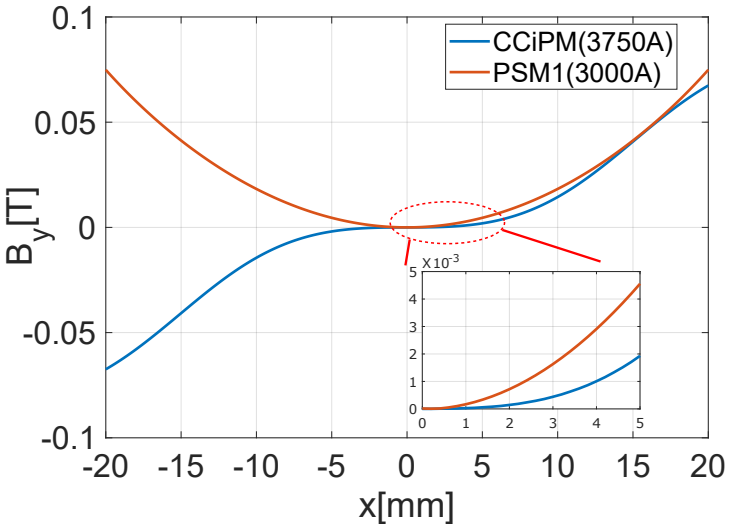


FIGURE 5.20: Comparison of transverse magnetic field between CCiPM and PSM1.

# Chapter 6

# Design and Optimization for an Octupole CCiPM

A prototype of the initial octupole CCiPM was tested. However, it had a large inductance. Power source is not capable of supplying a required current. This chapter mainly introduces the design and optimization of the CCiPM. The optimized CCiPM is expected to have a low inductance to perform PMM injection.

## 6.1 Problem and Optimization for the Octupole CCiPM

### 6.1.1 High Inductance in the Initial Design

A prototype of CCiPM whose bore diameter is 40 mm was made by Kyocera company. Fig. 6.1 (a) shows the fabrication of the octupole CCiPM. The cables connected to a terminal box to arrange the current flow direction. The schematic view of the circuit is shown in Fig. 6.1 (b). The total inductance measured with LCR meter is 11.15 μH, and the resistance is 0.40 Ω.

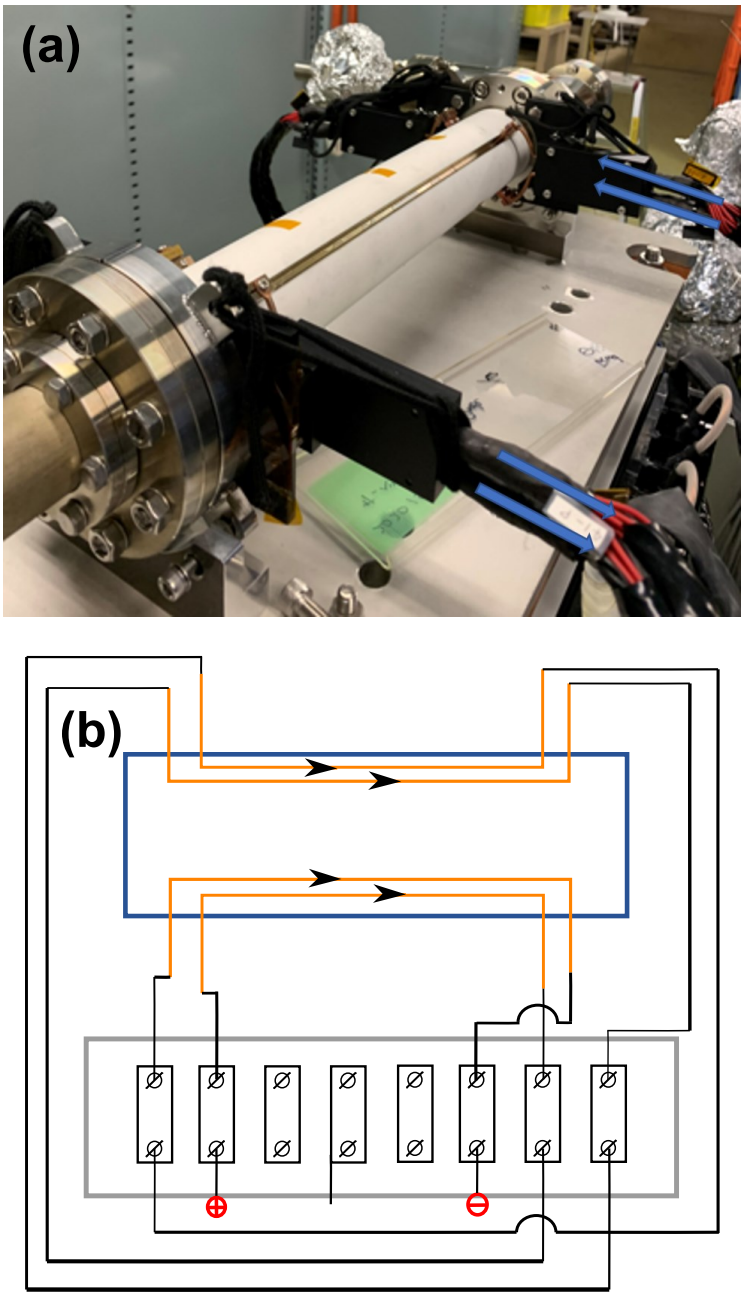


FIGURE 6.1: Construction of the initial octupole CCiPM. (a) Photograph. (b) Schematic view of the circuit.

If the one-turn kick injection is applied, the pulse width of a half-sine shape current is 1.2 µs, then the estimated impedance $Z$ is given by

$$Z = R + \mathrm{j}2\pi f L = 0.4 + \mathrm{j}29.2\Omega \tag{6.1}$$

where $R$ is the resistance, $f$ is the operation frequency, and $L$ is the inductance. If the output current reaches 3000 A, the peak pulsed voltage will be 90 kV. A pulsed power

source is incapable of supplying such a high voltage in the injection experiment.

The inductance part of this octupole CCiPM is much larger than the dipole CCiPM. There are mainly two reasons. One is that twisted cable does not work in the octupole CCiPM because of the parallel current. Therefore, the inductance of the cable cannot be ignored. The other reason is that the magnetic flux is full of the space, which is shown in Fig. 5.19. Hence, the stored energy is relatively large, which is related to the inductance directly. The relationship between the stored energy and inductance is approximately estimated by

$$W = \frac{1}{2}LI^2 \tag{6.2}$$

where $W$ is the stored energy, and $I$ is current value. The magnetic field simulation software Poisson can provide the stored energy of a 2D model. The result of the initial model in Fig. 5.19 is 0.25 J/cm with a 3000 A current. If the effective length of CCiPM is 0.29 m, the inductance will be 1.62 µH. This value is quite smaller than measured inductance, which indicates the cable is the dominant source of the high inductance.

### 6.1.2 Reduction of the Magnet's Inductance by Additional Conductors

To reduce the inductance, the length of the cable must be shortened. The terminal box is not an appropriate device to change the current flow direction. A more delicate method is required. Based on the design principle of air-core magnet, an optimized design of CCiPM was proposed. If four additional conductors are fixed on the surface of the ceramic chamber, The long cable will not be necessary anymore. The cross-sectional view of the optimized CCiPM in Poisson is shown in Fig. 6.2. The direction of the current in four additional conductors is reverse with that of the inner conductors. The radius of the additional conductor is 2 mm. From the distribution of the magnetic flux, the octupole magnetic field is remained around the center. To change the current flow direction, a small arc conductor can be used to connect the inner conductor to the additional conductor.

It can be seen that the magnetic flux is also restricted. The result of the new model in Fig. 6.2 is 0.17 J/cm with a 3000 A current. If the effective length is 0.29 m, the inductance will be 1.15 µH, which is smaller than that of the initial model. The inductance is reduced from the perspective of the stored energy.

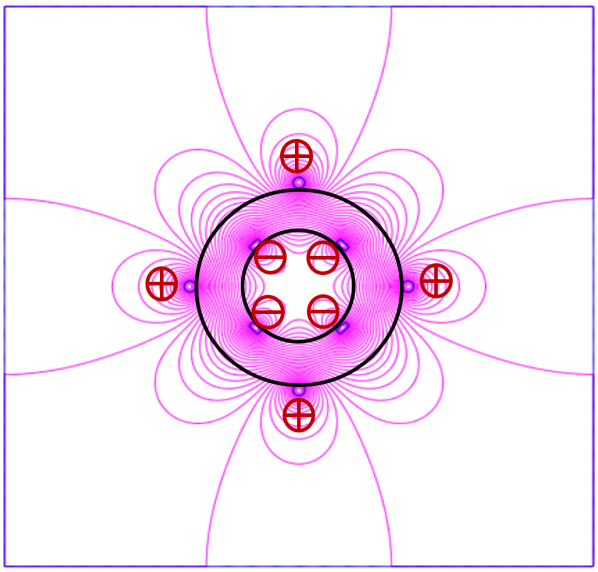

FIGURE 6.2: Cross-sectional view of the optimized CCiPM with magnetic flux.

Fig. 6.3 shows the comparison of the transverse magnetic fields between the initial and optimized CCiPM. The applied current is 3000 A. The off-axis magnetic field of the optimized model is enhanced a lot. At $x$=15 mm, the initial value is 0.033 T, but the value of the optimized model is 0.041T. It is because that the additional conductors can also generate an octupole magnetic field separately. In addition, the magnetic field strength of the optimized model hardly changes around the center.

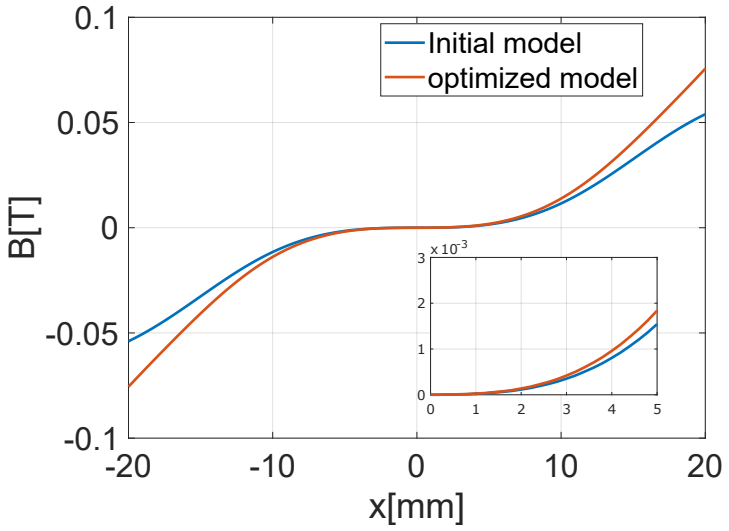


FIGURE 6.3: Comparison of transverse magnetic fields between the initial and optimized CCiPM.

Based on the 2D simulation result of Poisson, the optimized model has not only a low

inductance but also a stronger kick effect. Next, OPERA-3D [58] was used to perform a detailed design of the CCiPM and evaluate the magnetic field.

## 6.2 Design and Optimization of the Magnet Coil Structure

### 6.2.1 Design for a 3D Model

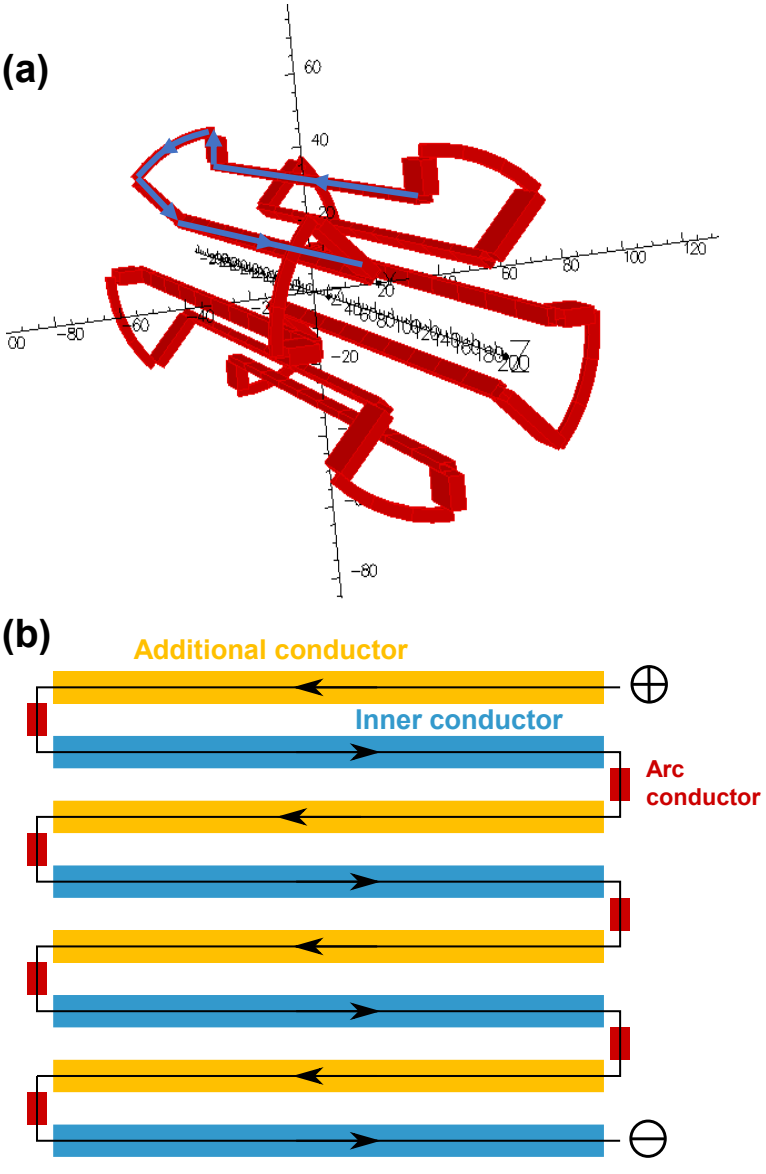


FIGURE 6.4: (a) A preliminary model of CCiPM in OPERA-3D. (b) Schematic view of the circuit of the optimized model.

A preliminary model of the octupole CCiPM was constructed in OPERA-3D, which is shown in Fig. 6.4 (a). In the simulation, the applied current is 3000 A. Because CCiPM

is an air-core pulsed magnet, only conductor models were constructed. The current direction is marked. It is noted that only a cube model can be used in the simulation. There is no cylinder model that can be simulated as a current flow in OPERA-3D. The conductor model in OPERA-3D was made as similar as a real model but cannot be same with a real model.

The length of the long conductor is 290 mm. An arc model was used to connect the inner conductor to the additional conductor. Fig. 6.4 (b) shows the schematic view of the circuit of the optimized model.

The magnetic field components at the center can be extracted from the $B_r$. Fig. 6.5 shows the magnetic field components ($r$=15 mm) at the middle of the model. $B_4$ represents the strength of the octupole magnetic field, and $B_n$ means another order term of the magnetic field. Obviously, the octupole magnetic field is dominant. It also shows that only a small dipole component exists for low order terms. However, there is a strong eighth order term that is opposite to the octupole magnetic field. Because the current distribution of CCiPM also satisfies a $\cos 8\theta$ distribution. As for the 12th order term, it is from the allowed error multipoles term [59] which satisfies:

$$N_{allowed} = n(2m + 1) \tag{6.3}$$

where $m = 1, 2, 3...$ and $n$ is the lowest order of magnetic field. For an octupole magnetic field, $n = 4$, the first allowed error multipole is 12th order.

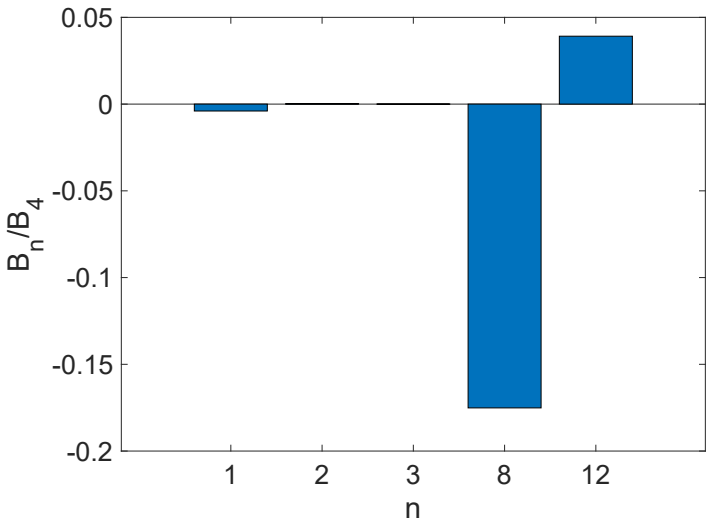


FIGURE 6.5: Magnetic field components ($r$=15 mm).

### 6.2.2 Optimization for the Busbar

According to the PSM measurement result, the bus structure breaks the symmetry of current flow and generates undesirable magnetic field along longitudinal center axis. The influence from the busbar structure should be as small as possible. Several designs have been discussed. The first design is to shorten the gap, which is shown in Fig. 6.6.

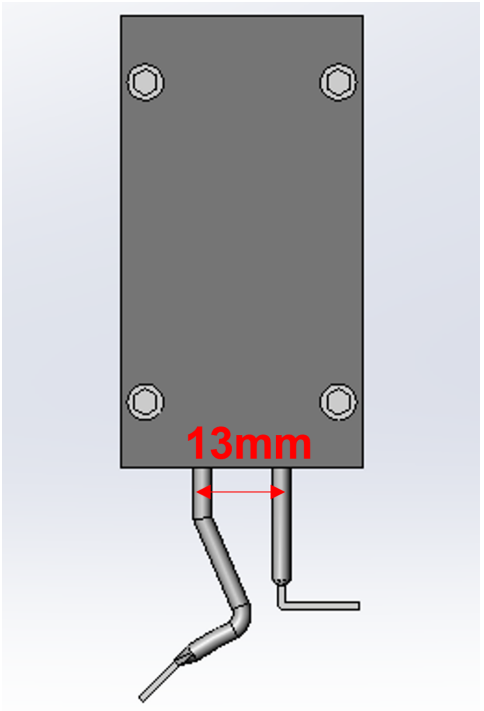


FIGURE 6.6: A busbar structure with a narrow gap.

The gap of the busbar is very narrow to generate a relatively small magnetic field along the longitudinal axis. Although there is a risk of electric discharge, the conductor can be insulated to raise the threshold.

The second design is to extend the length of the additional conductor in the longitudinal direction. The gap is almost closed in the front view, which is shown in Fig. 6.7. But the extended conductor may break the symmetry of the current flow.

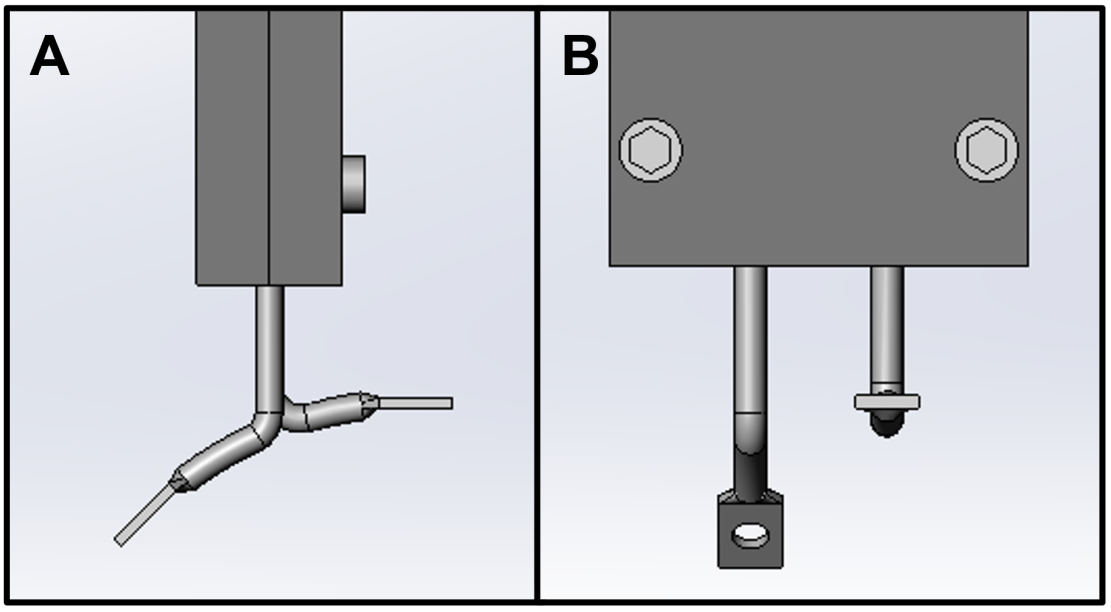


FIGURE 6.7: A possible busbar structure. (A) Front view, (B) Side view.

As for the third design, the concept is similar, and the model is shown in Fig. 6.8. It is a bended model to achieve a compensation of magnetic field. The gap is almost closed, and the length of the long conductor does not change. However, an electrical discharge can easily occur.

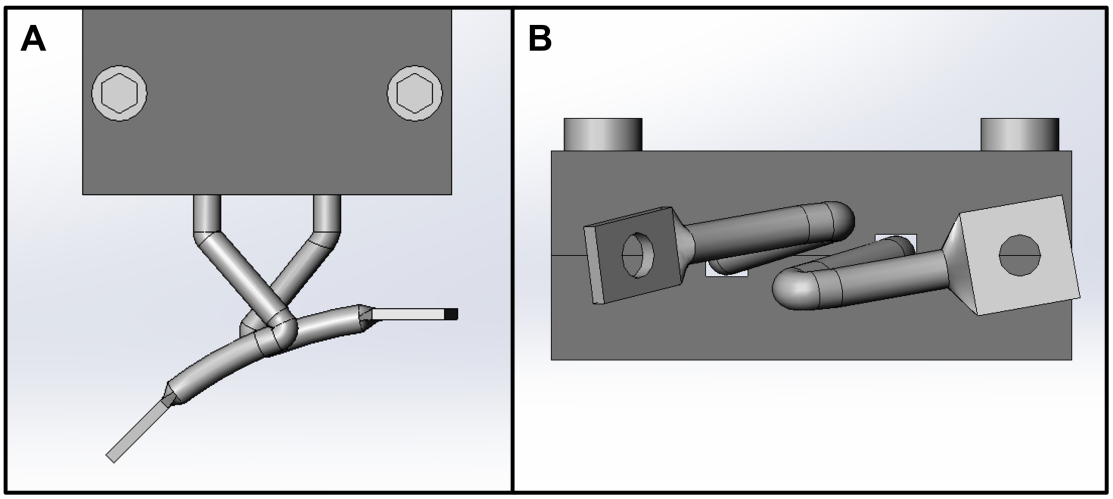


FIGURE 6.8: Another potential busbar structure. (A) Front view, (B) Upward view.

The three models of the CCiPM with the busbar were constructed in OPERA. The first model is shown in Fig. 6.9. It is noted that the current flow in a real model is much more complex than that in simulation. The three models were constructed carefully and simulated as accurately as possible. The current is 3000 A in the simulation.

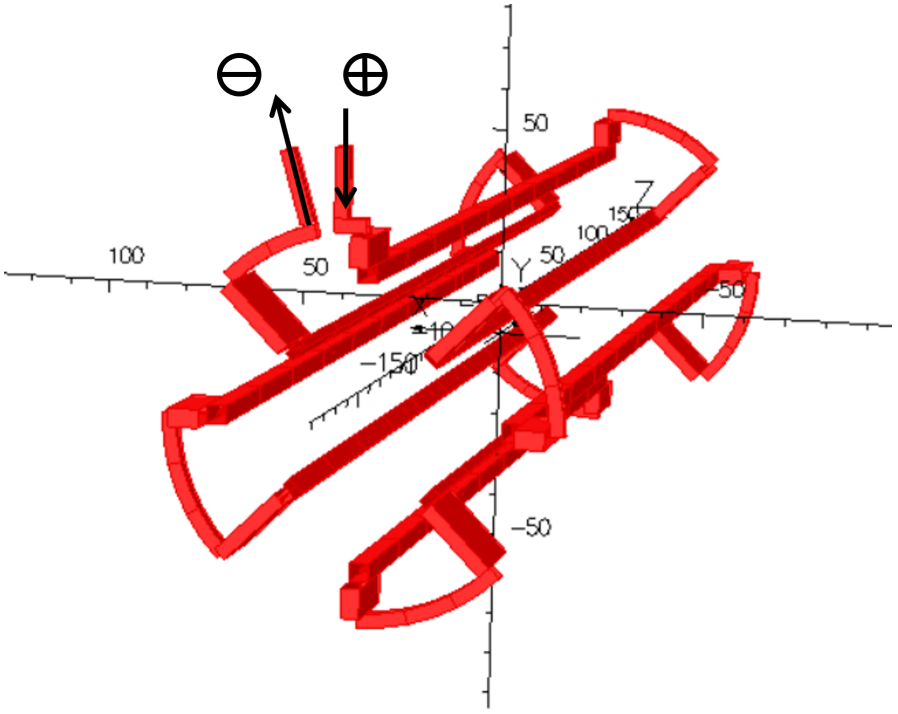


FIGURE 6.9: The first model of the CCiPM with busbar in OPERA-3D.

The longitudinal distributions of the $B_y$ and $B_x$ at $x$=0 mm ($y$=0 mm, $-400 \leq z \leq 400$ mm) of these three models are shown in Fig. 6.10. Table 6.1 gives the integrated fields of three model. As for the second and third model, the integrated fields of the $B_y$ is smaller than

the value of the first. They have a larger integrated field of the $B_x$, which can induce a vertical stored beam oscillation. Therefore, the magnetic field property of the first design is most superior, and the first model has been selected.

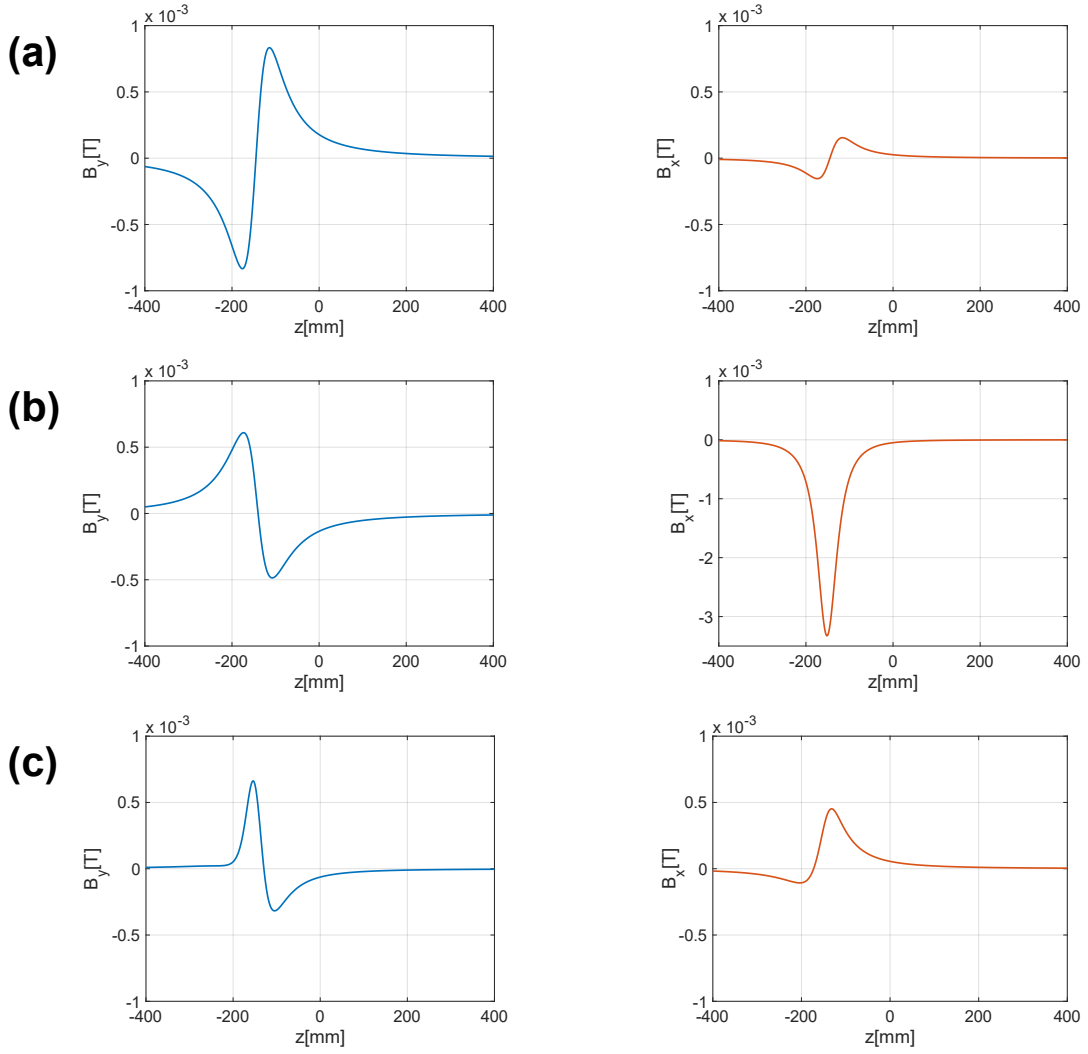


FIGURE 6.10: Longitudinal distributions of the $B_y$ and $B_x$ at $x$=0 mm. (a)1st design. (b)2nd design. (b)3rd design.

TABLE 6.1: Integrated magnetic fields of three models at $x$=0 mm.

| Model1 | Integrated magnetic field ($B_y$) [μT · m] | Integrated magnetic field ($B_x$) [μT · m] |
|---|---|---|
| 1 | 8.7 | 1.2 |
| 2 | 1.3 | 241.4 |
| 3 | 3.7 | 29.8 |

Then the integrated magnetic field at $x$= 15 mm ($y$=0 mm, $-400 \leq z \leq 400$ mm) was evaluated for the kick effect. The distribution is shown in Fig. 6.11. The integrated magnetic field is 11.1 mT · m, which is less than the designed value of PSM1 (12 mT · m). Compared with iron-core magnet, the strength of magnetic field is a shortcoming of air-core magnet. Generally, a higher current is required. Therefore, to inject the beam in PF ring, the applied current is expected to be 3240 A and is still feasible for a power source.

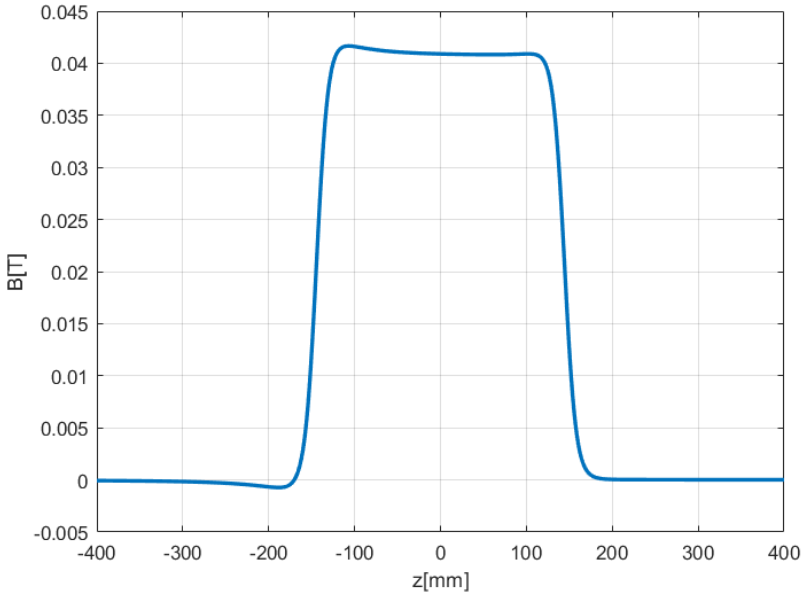


FIGURE 6.11: Longitudinal distribution of the $B_y$ at $x$=15 mm.

Based on the simulation results, the octupole CCiPM can have an off-axis kick effect that is almost same with that of PSM1. Table 6.2 gives the integrated field ($B_y$) results between PSM1 and CCiPM. The stored beam oscillation in the CCiPM injection is expected to be dramatically reduced.

TABLE 6.2: Integrated magnetic fields of PSM1 and CCiPM (I=3000 A)

| | PSM1 | CCiPM |
|---|---|---|
| Integrated field ($B_y$) at $x$=15 mm | 12.0 [mT · m] | 11.1 [mT · m] |
| Integrated field ($B_y$) at $x$=0 mm | 1170 [μT · m] | 8.7 [μT · m] |

## 6.3 Internal Coating

Section 4.1 introduced the comb-shape coating technology of CCiPM. However, it is found that the eddy current effect of a circular titanium coating is negligible from the previous research. In addition, the transverse magnetic field in the midplane is an octupole field. The eddy current effect of the coating is expected to be very small. Considering the impedance issue of the internal coating, a comb-shape coating with a wide width has been chosen as the internal coating inside the ceramic chamber.

An octupole CCiPM model was constructed in ELF/MAGIC, which is shown in Fig. 6.12. Because there is a risk of electrical discharge between the conductor and coating. A 5.0 mm wide gap is present between the conductor and coating to increase the threshold voltage of electrical discharge in vacuum.

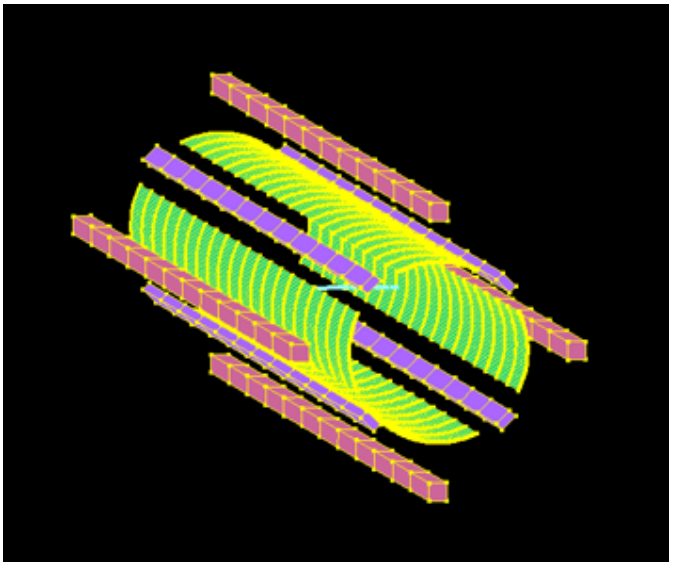

FIGURE 6.12: Octupole CCiPM with coating in ELF/MAGIC.

The eddy current effect of the coating is estimated by the same way in Section 4.2. The result is shown in Fig. 6.13, which is consistent with the expectation. The coating does not generate undesirable magnetic field at the center, and the off-axis attenuation ratio of the peak magnetic field is 99.2%.

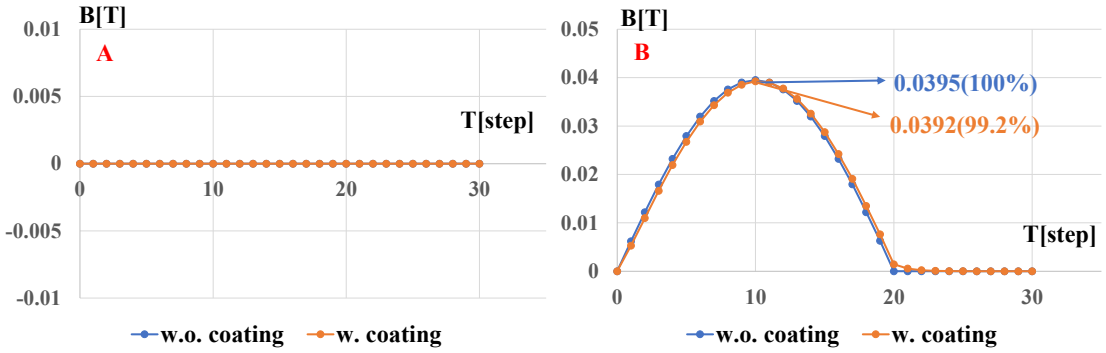


FIGURE 6.13: Time evolution of $B_y$ in the CCiPM at (A) $x$=0 mm and (B) $x$=15 mm.

The schematic view of the internal coating is show in Fig. 6.14. The comb shape is kept at the end of the chamber.

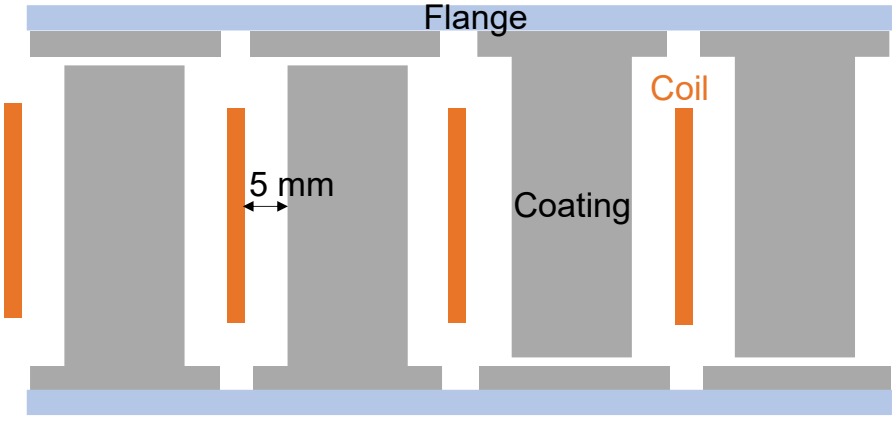


FIGURE 6.14: Schematic view of the internal coating.

## 6.4 Mechanical Design for the New Prototype

Finally, it is about the mechanical design of the optimized CCiPM. Fig. 6.15 shows the model of one additional conductor. Two metal blocks should be connected to the end of the long conductor by soldering. The length between the two blocks is 290 mm, which is consistent with the parameter of CCiPM.

To fasten the additional conductor precisely on the surface of the ceramic chamber, a special jig was designed. As shown in Fig. 6.16, the internal diameter is 60 mm, which is same with the external diameter of the octupole CCiPM. The white part is a small piece of PEEK block, which is stuck into the groove of the ceramic. The PEEK block

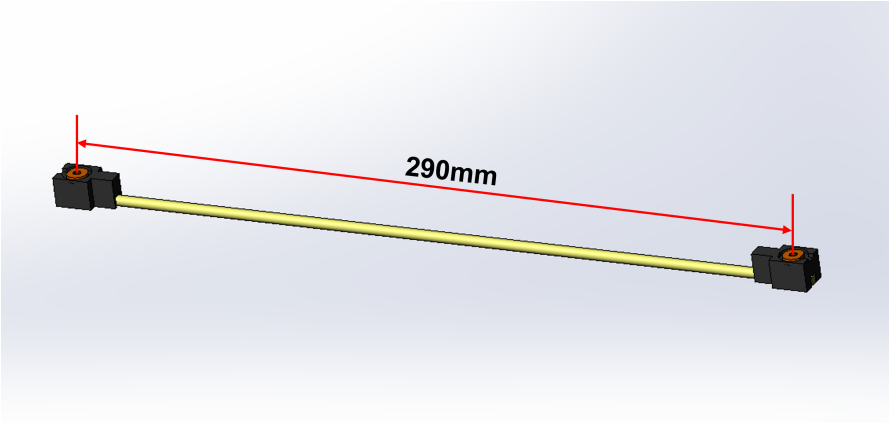


FIGURE 6.15: 3D model of one addition conductor.

can help fasten the additional conductor correctly by preventing the rotation error from the jig.

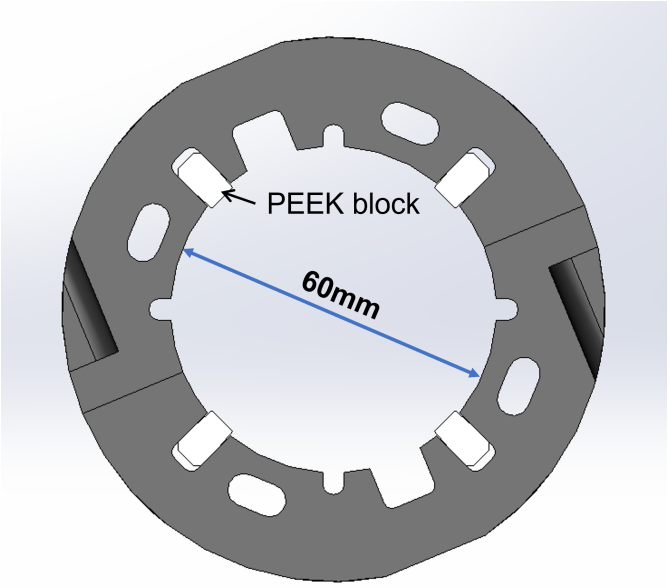


FIGURE 6.16: Design of the jig to fix the additional conductor.

To suppress the eddy current effect of the jig, the material should be non-magnetic and non-conductive. Plastic or resin is a suitable choice.

The 3D model of the octupole CCiPM is shown in Fig. 6.17. A stage for alignment in XYZ-direction is also included.

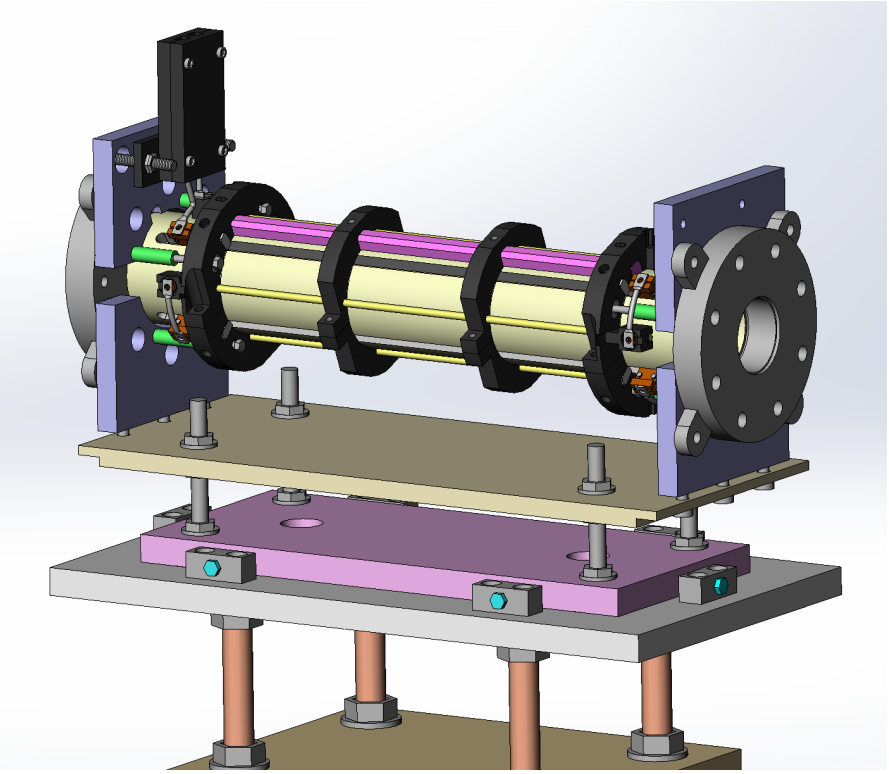

FIGURE 6.17: 3D model of the octupole CCiPM.

# Chapter 7

# Performance Test of the Octupole CCiPM

## 7.1 Assembly of the Octupole CCiPM

The photograph of CCiPM-D40 is shown in Fig. 7.1. Fig. 7.2 is the internal coating of CCiPM-D40. The additional conductor is shown in Fig. 7.3.

FIGURE 7.1: Prototype of CCiPM-D40.

FIGURE 7.2: Internal coating of CCiPM-D40

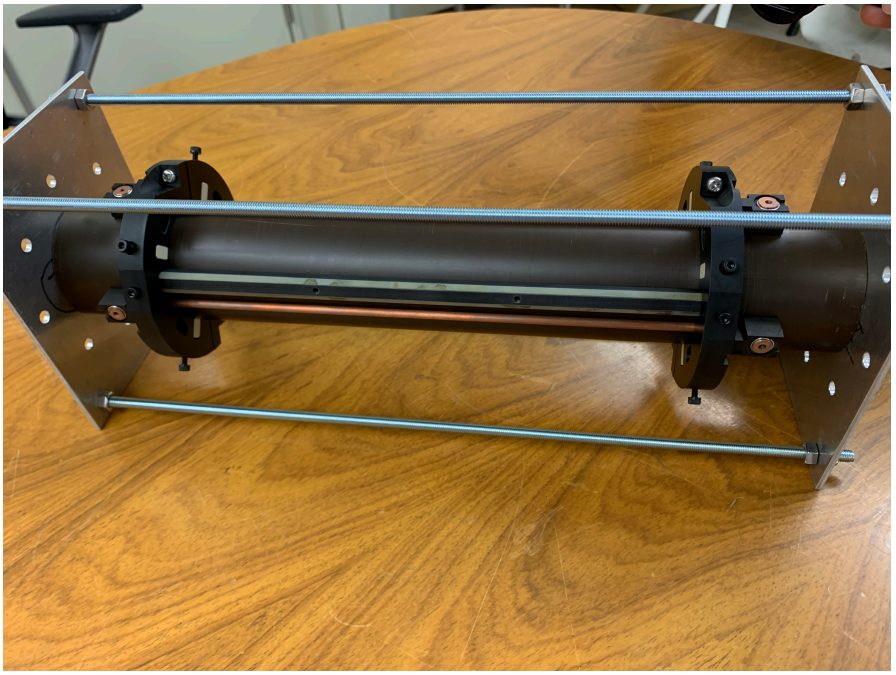

FIGURE 7.3: Photograph of the additional conductor.

As shown in Fig. 7.4, the octupole CCiPM was successfully assembled. The inductance of the whole CCiPM was measured with a LCR meter, which consists of the busbar structure. When the operating frequency is 500 kHz, the inductance is 1.45 µH and the resistance is 0.27 Ω. The inductance is reduced significantly compared with the initial design. In one-turn kick condition, the impedance of CCiPM is expected to be 3.80 Ω. If the peak value of the applied current is 3240 A, the necessary peak voltage is 12.31 kV. The electrical parameters of the initial and optimized CCiPM are shown in Table 7.1. It demonstrates that the PMM injection by the optimized CCiPM in one-turn kick is feasible.

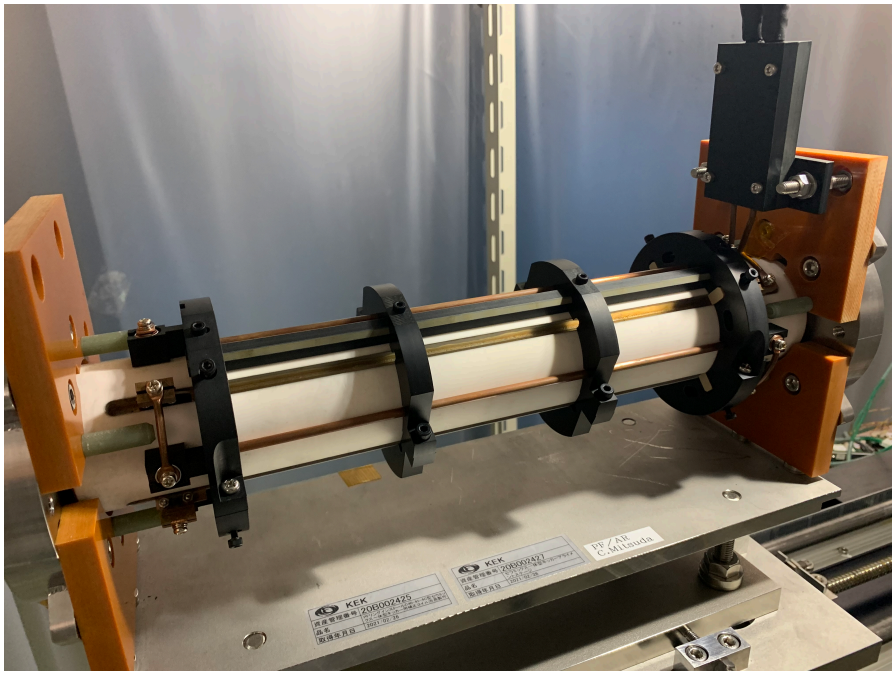

FIGURE 7.4: Assembly of the octupole CCiPM.

TABLE 7.1: Electrical parameters of the initial and optimized CCiPM.

| | Inductance[µH] | Impedance in one-turn kick [Ω] | Designed peak current[A] | Necessary peak voltage[kV] |
|---|---|---|---|---|
| Initial model | 11.15 | 29.20 | 3000 | 87.57 |
| Optimized model | 1.45 | 3.80 | 3240 | 12.31 |

## 7.2 Baking and Vacuum Extraction

After the assembly and measurement for the inductance, the vacuum tightness and heat durability of the CCiPM were tested next.

### 7.2.1 Construction for an Offline Test Bench

To examine the performance of CCiPM, an offline test bench for CCiPM was constructed. Fig. 7.5 shows CCiPM on the test bench. The upstream of CCiPM connected to an ionization gauge to measure vacuum pressure. The downstream connected to the Turbo Molecular Pump (TMP) and Scroll Pump (SP) for the vacuum extraction.

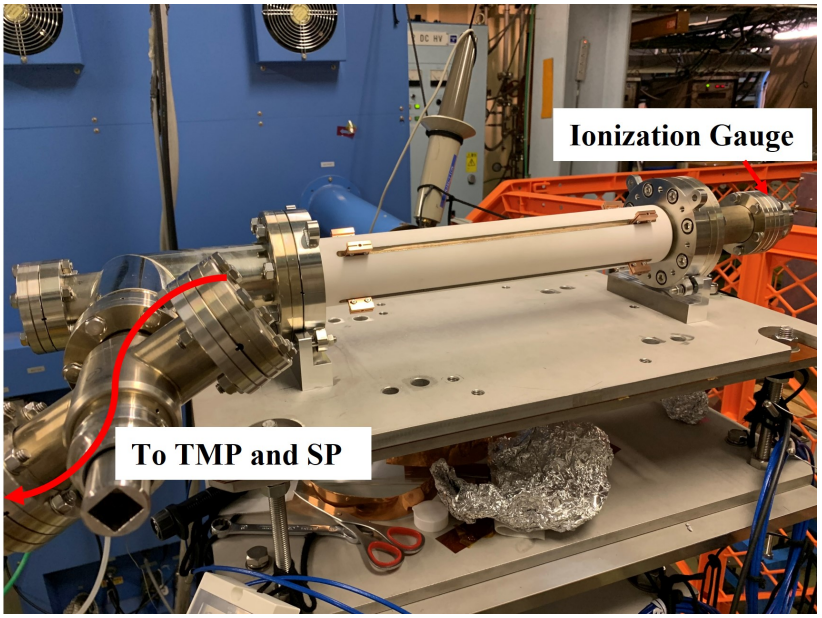


FIGURE 7.5: Construction of the test bench for the CCiPM.

The diagram of the vacuum system is shown in Fig. 7.6. Apart from one ionization gauge connected to the CCiPM, there are a cold cathode gauge installed around the TMP and a ionization gauge around the SP. A leak detector is connected to the end of the system to check whether there is a leakage in this system.

After the construction of the system, the vacuum extraction was carried out to reach a vacuum pressure lower than the order of $10^{-4}$ Pa. Then the leak detector was used and there was no leakage. The vacuum tightness of CCiPM was verified preliminarily. As shown in Fig. 7.7, then five thermocouples were pasted on the CCiPM to observe

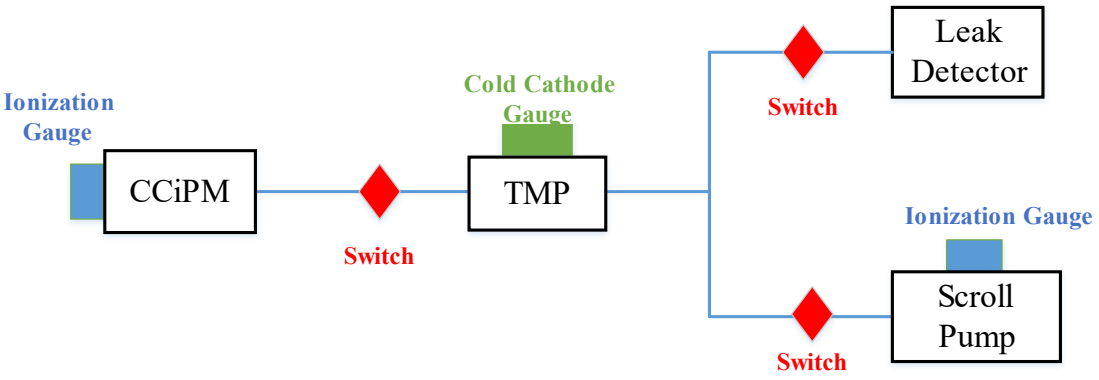


FIGURE 7.6: Diagram of the vacuum system.

temperature during baking, which were connected to a data recorder. The temperature around the pumps were also observed by two thermocouples in case.

After the preparations, several ribbon heaters were bound to the CCiPM and pipe. Finally, they were covered completely in the aluminum foil, which is shown in Fig. 7.8.

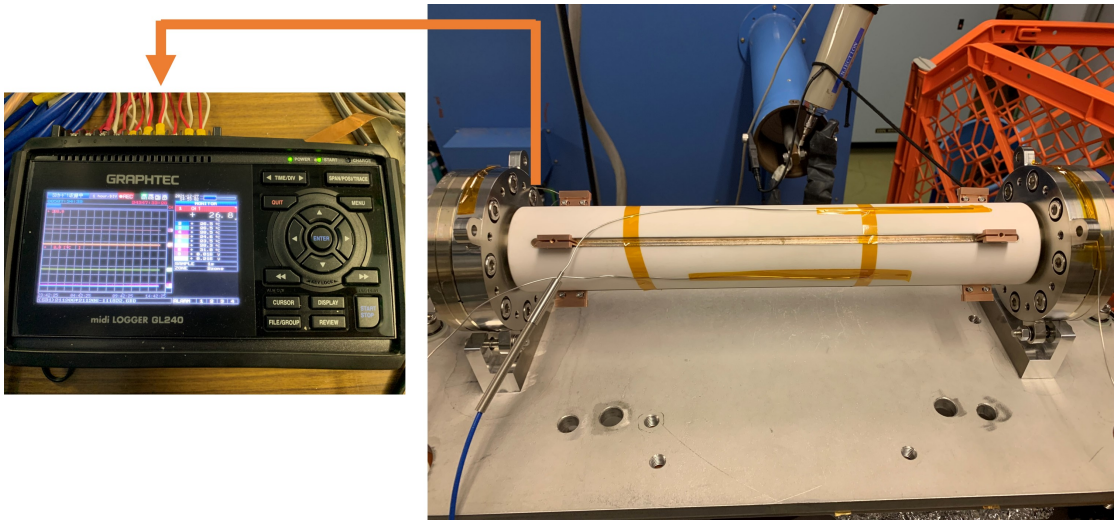


FIGURE 7.7: Thermocouples and data recorder for observing temperature.

The baking was continued for about one month. A continuous baking was performed for two weeks at first, the temperature of the CCiPM was around 130 °C. Then a heating-cycle baking for the CCiPM was applied, which was used as an accelerated aging test to simulate a severe situation assuming that the CCiPM is installed in a ring. One heating cycle starts at room temperature, ramps to around 120 °C and holds for 4 h, then cools down naturally for the other 4 h. The heating-cycle baking was controlled by an automatic timing device and continued for about two weeks.

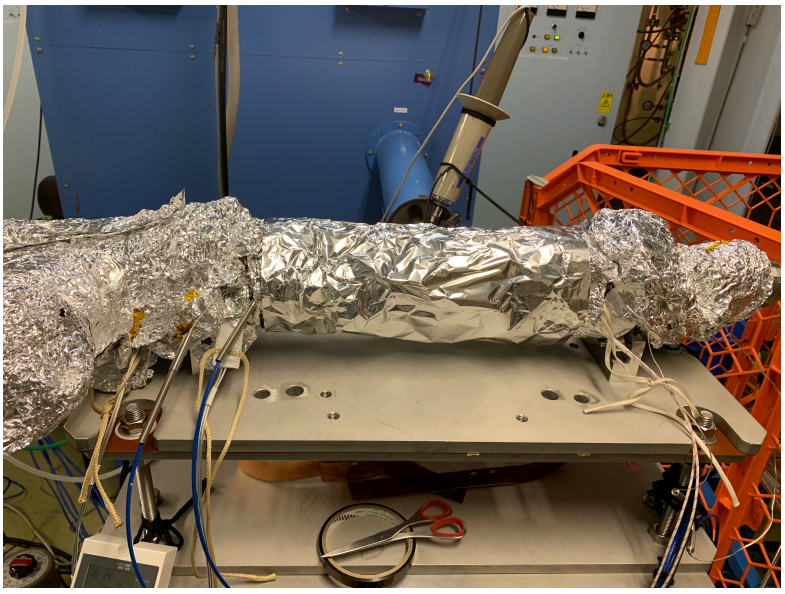

FIGURE 7.8: Photograph of the CCiPM during baking.

### 7.2.2 Experimental Results of the Vacuuming and Baking

The record of temperature during continuous baking is shown in Fig. 7.9. The results of Channel-01, Channel-02 and Channel-03 are from three thermocouples pasted on the CCiPM, and the results of Channel-04 and Channel-05 are from two thermocouples pasted on the flange. As shown in Fig. 7.10, the temperature changed regularly during the heating-cycle baking. There was no accident during the whole baking, which proved that the CCiPM has a good heat durability. After the baking was stopped, the vacuum reached to $1 \times 10^{-7}$ Pa indicating that the CCiPM can be installed in the PF ring.

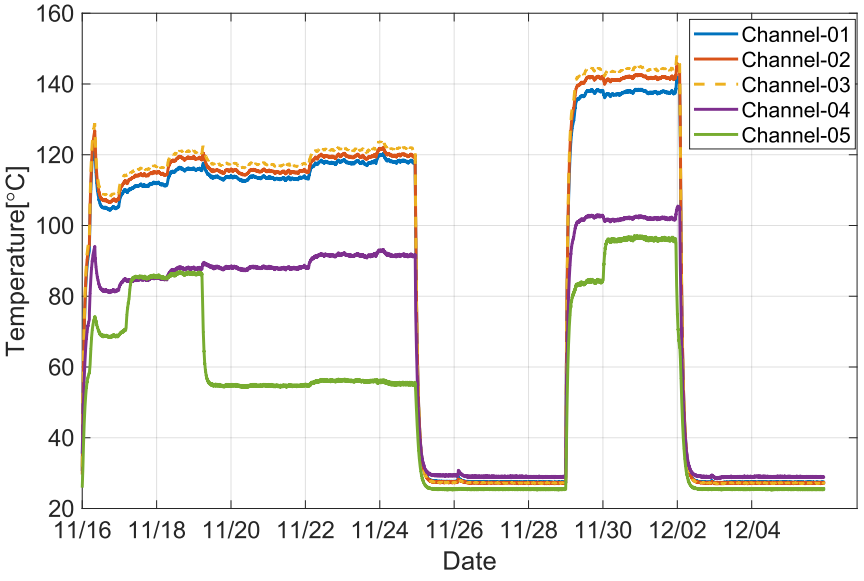


FIGURE 7.9: Record of the temperature during continuous baking.

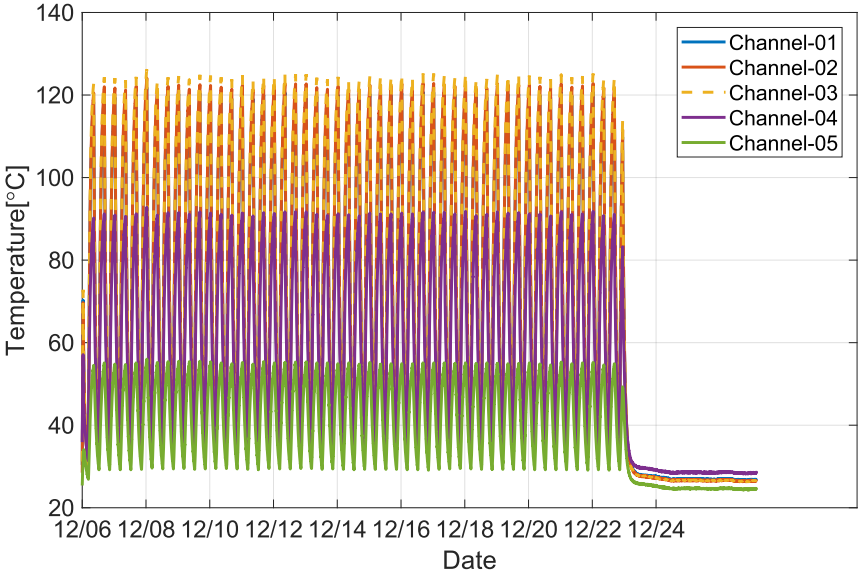


FIGURE 7.10: Record of the temperature during heating-cycle baking.

## 7.3 Current Excitation Test

A current excitation test was performed to examine whether the designed current can flow through the CCiPM. The current was measured with a CT. In addition, the voltage was measured with a high voltage probe (Tektronix P6015A), which is shown in Fig. 7.11. In the experiment, the repetition rate was 10 Hz to get a high voltage. Fig. 7.12 is the

screenshot of the oscilloscope, the lightblue signal is from the high voltage probe, and the black signal is from the CT. Owing to the performance of the power source, the pulse width of the current is 2.8 µs.

FIGURE 7.11: High voltage probe.

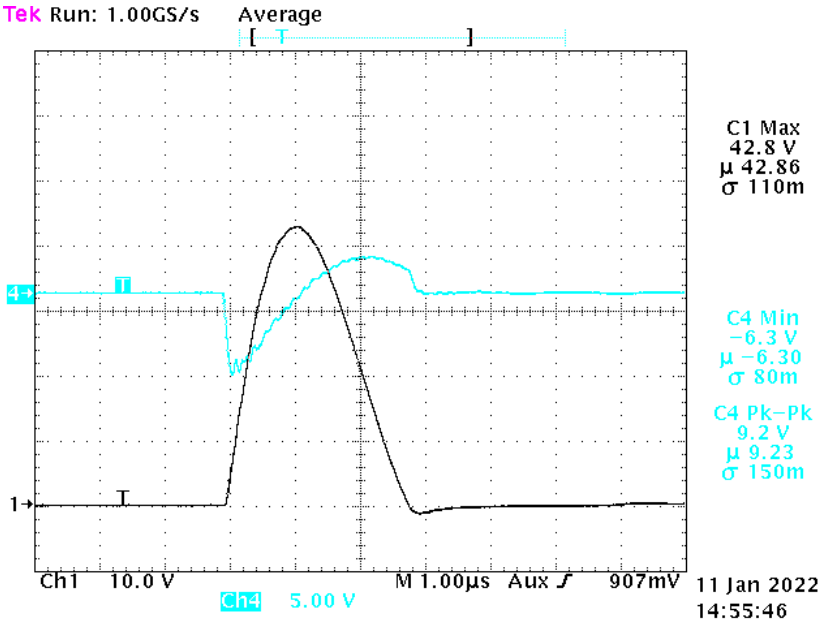


FIGURE 7.12: Screenshot of the oscilloscope in excitation test.

The experimental result is shown in Fig. 7.13. Because of the limitation of the power source, the DC charging voltage cannot be larger than 10 kV. The maximum peak current of the optimized model that has 8 conductors is 2800 A, which is close to the designed value. There was no electrical discharge during the experiment. However, for the initial model that has 4 conductors, the impedance is large, and the pulse width of the current is 6 µs. Electrical discharge was present when the DC output voltage was larger than 7 kV, and the current was only about 1000 A.

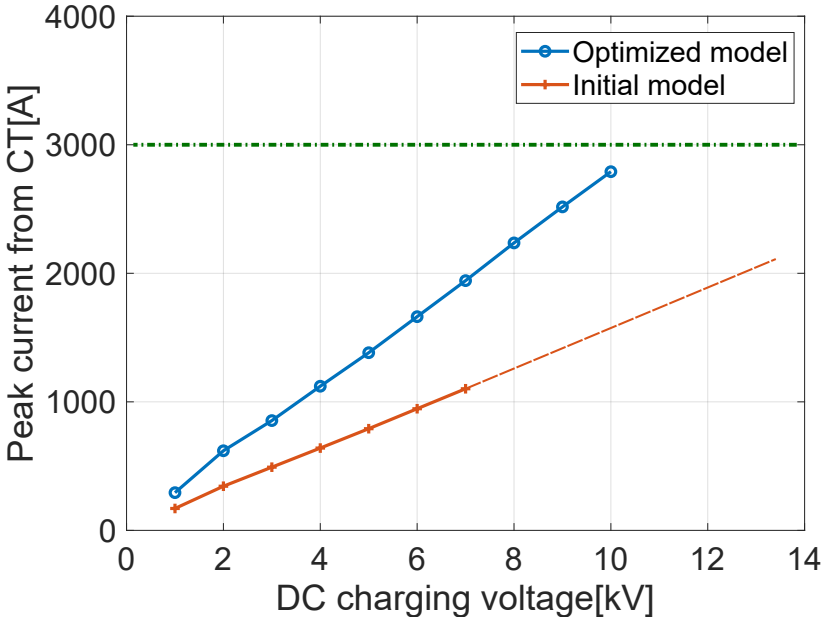


FIGURE 7.13: Experimental results in the current excitation test.

## 7.4 Magnetic field Measurement

The DC and pulsed magnetic fields were measured. The measurement results are compared with the simulation data to evaluate the performance of the CCiPM.

### 7.4.1 Measurement System

To measure the magnetic field, the measurement system for PSM1 was used again. The magnetic fields were measured by the Hall probe and pick-up probe. Fig. 7.13 shows the photograph of the pulsed magnetic field measurement of the CCiPM. The experimental coordinate is marked, and the origin is located at the center of the CCiPM. The flange of the CCiPM has alignment lines. The alignment in the vertical $y$ direction was performed by a wild N3. As for the longitudinal $z$ direction, it can be aligned by a theodolite directly, because the probe can move upon the CCiPM.

In the pulsed magnetic field measurement, the peak value of the current was 200 A, and the pulse width was 0.8 µs. As for the DC magnetic field measurement, the current was still 15 A.

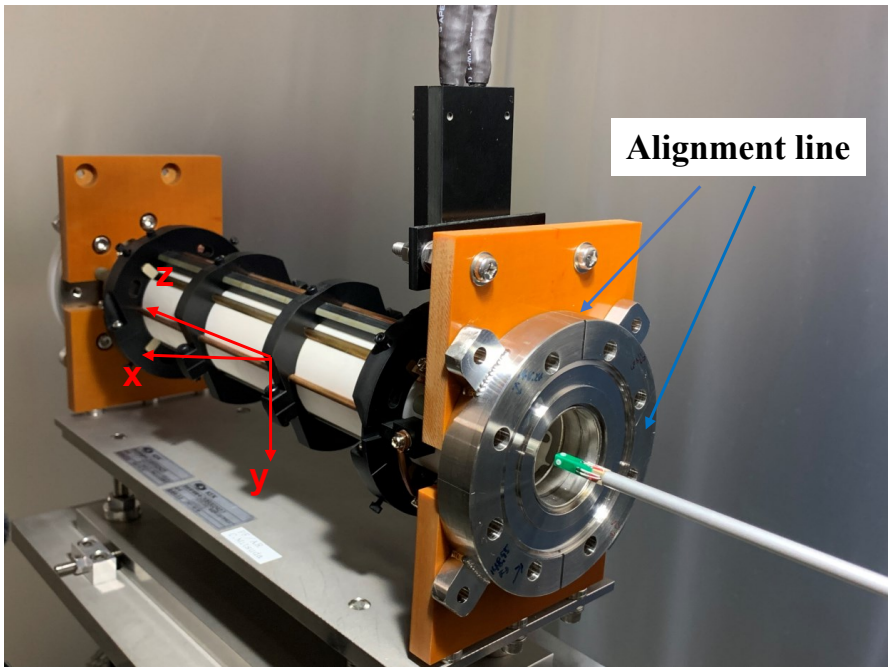


FIGURE 7.14: Photograph of pulsed magnetic field measurement of the CCiPM.

Because of the narrow bore of CCiPM, the measurement region was limited. Otherwise, the arm may hit the duct. It ranges ±12 mm in the horizontal $x$ direction, ±300 mm in the longitudinal $z$ direction.

### 7.4.2 Measurement Results

Some results are extracted from the measurement data to evaluate the performance of CCiPM. The DC and pulsed magnetic fields are normalized under the condition of a 3000 A current for comparison. The horizontal distributions of the simulation, normalized DC field, and normalized pulsed field at the center are shown in Fig. 7.15. The result of DC magnetic field is almost same with the simulation data. As for the pulsed magnetic field measurement, because the octupole magnetic field is bidirectional along horizontal axis, the integrated voltage signal is taken at a specific timing, which is same with the measurement in the PSM. If the magnetic field induces a strong voltage signal that has a half-sine wave shape, the peak value is taken at the specific timing. Obviously, it is a magnetic field distribution of an octupole magnet. However, the calculated peak magnetic field is 80% of the simulation value. It is noted that the error bar only includes the repetition error in the pulsed magnetic field measurement.

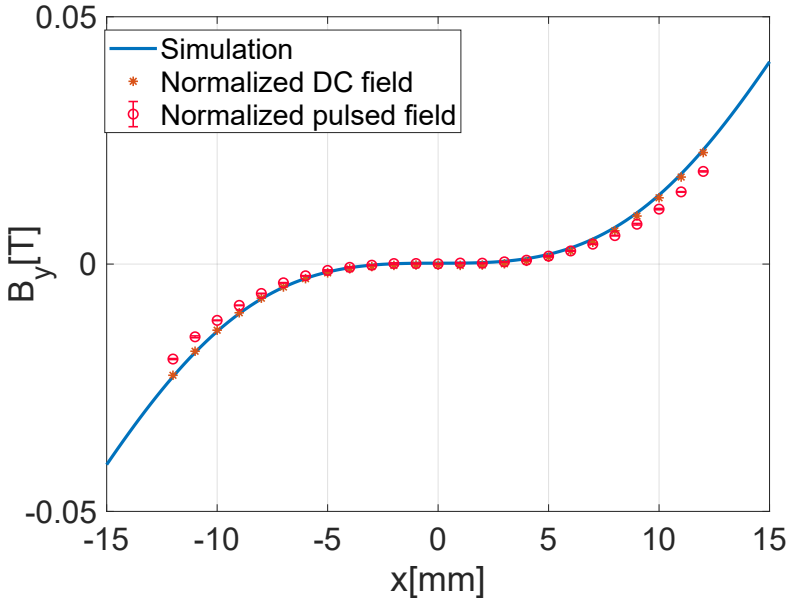


FIGURE 7.15: Horizontal magnetic field distributions at $z$=0 mm ($-12 \leq x \leq 12$ mm, $y$=0 mm).

Fig. 7.16 shows the longitudinal distributions of magnetic fields at $x$=10 mm ($y$=0 mm, $-300 \leq z \leq 300$ mm). The shape of the distribution DC magnetic field is almost same with the simulation. At the edge of flat field, the magnetic field property is not good. The issue is discussed in next subsection. As for the pulsed magnetic field, it is still less than the simulation. At $z$=0 mm, the simulation value, the normalized DC magnetic field, and the normalized pulsed magnetic field are 0.0140 T, 0.0138 T, 0.0114 T, respectively.

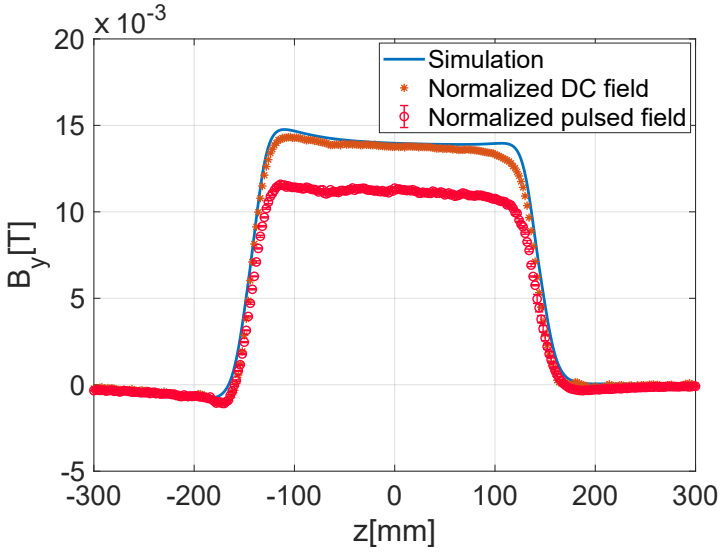


FIGURE 7.16: Longitudinal magnetic field distributions at $x$=10 mm ($y$=0 mm, $-300 \leq z \leq 300$mm).

Finally, the longitudinal distributions at $x$=0 mm ($y$=0 mm, $-300 \leq z \leq 300$ mm) are

shown in Fig. 7.17. Compared with the simulation, two spikes in the DC magnetic field distribution appears around $z$=±150 mm. It indicates that some undesirable magnetic components may present in the prototype. As for the pulsed field, there is a problem about the electromagnetic noise which cannot be removed totally in the circuit. This issue has been explained in the PSM measurement. At $z$=300 mm outside the CCiPM, the DC magnetic field is zero, but the integrated voltage signal is a noise signal with an amplitude of 1.2 nV · s. After the transformation, the normalized pulsed field is $4.4 \times 10^{-4}$ T. Because the magnetic field is too weak at the center of the CCiPM, a clear integrated voltage signal with a half-sine wave shape was not measured at the center. The minimum value of the integrated voltage signal is taken to calculate the strength of the peak pulsed magnetic field. Although the measurement result has a systematic error, the distribution of the normalized pulsed magnetic field is similar with that of the normalized DC maghnetic field. Two spikes also appear around $z$=±150 mm, which can prove the presence of an irregular magnetic field.

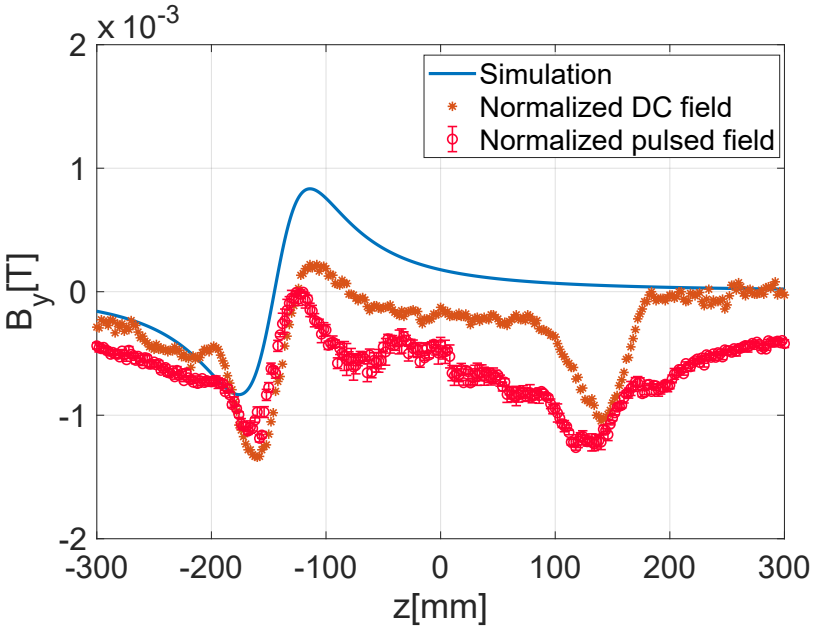


FIGURE 7.17: Longitudinal magnetic field distributions at $x$=0 mm ($y$=0 mm, $-300 \leq z \leq 300$ mm).

### 7.4.3 Investigation and Analysis

There are some problems in both DC and pulsed magnetic field measurement, and they should be discussed separately.

Two issues should be investigated in the DC magnetic field measurement. One is the spike in the longitudinal distribution around $z$=±150 mm. The other one is that

In the simulation, the magnetic field is only generated from the current in the coil. There is no magnetic component in the simulation model. Although the joint between the flange and ceramic is made from Kovar, which is a magnetic material. The effect of the Kovar was not taken into consideration during the design, because the magnetic field is almost negligible around Kovar. It has been examined by the $B_x$ measurement of the PSM with the chamber installed in Fig. 3.26.

To examine whether the spike is related to the Kovar or not, the longitudinal distribution of $B_x$ was measured. Because the $B_x$ is even much smaller than the $B_y$. The effect of the Kovar should be negligible. The measurement result is shown in Fig. 7.18. Two spikes are still present around $z$=±150 mm. The peak value of the $B_x$ is about $-8 \times 10^{-4}$ T that is close to the result of the $B_y$. And the Kovar is located around $z$=±180 mm. Therefore, the spike is not caused by the Kovar.

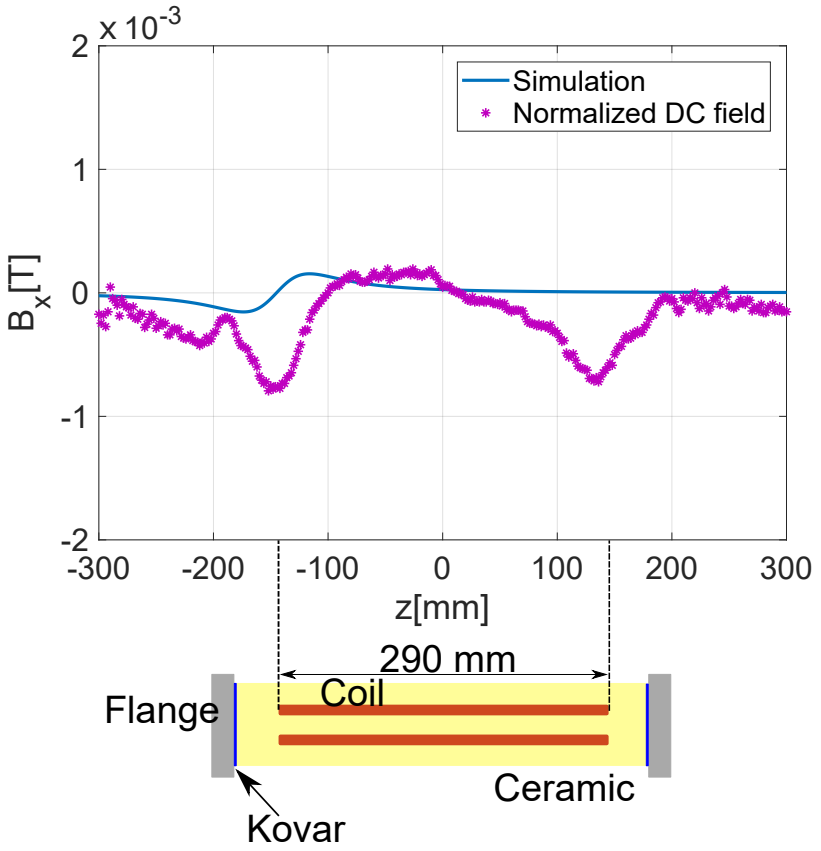


FIGURE 7.18: Longitudinal distributions of the $B_x$ at $x$=0 mm ($y$=0 mm, $-300 \leq z \leq 300$ mm).

The effective length of the coil is 290 mm. The end of the coil is very close the position of the spike. In fact, the joint between the coil and metal block is also a critical element. In the simulation, the current density is assumed to be uniform in the metal block. However, in a real model, the direction of the current flow and current density depend on the quality of the brazing. Therefore, the uniformity of the magnetic field may be influenced by the joint.

Another element that may have an effect on the magnetic field around $z$=±150 mm is the arc conductor, which is used to change the current direction. In the fabrication, the alignment about the position of the additional conductor was conducted by a laser level, which is shown in Fig. 7.19. The arc conductor has a manufacturing error. Therefore, the current flow in the arc conductor is not symmetric, and the magnetic field cannot be compensated perfectly at the center.

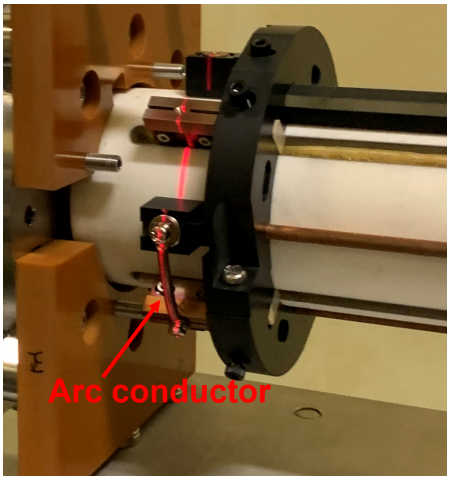


FIGURE 7.19: Alignment of the arc conductor by laser level.

Some elements that may be related to the spike in the DC magnetic field distribution has been discussed. The Kovar is not related to this issue from the $B_x$ measurement. As for the arc conductor, it is not likely to generate such a magnetic field within manufacturing error. The joint between the coil and metal block is supposed to be closely related to this issue. However, a concrete reason cannot be provided now. The joint will be studied carefully in the future.

The pulsed magnetic field measurement also has two issues to be solved. The longitudinal distribution of $B_y$ at the center is not accurate, and the off-axis pulsed magnetic field after calculation is only 80% of the simulation value.

The former problem is related to the resolution power of the pick-up probe and weak magnetic field at the CCiPM's center. It has been mentioned that the noise level of the normalized pulsed field is $4.4 \times 10^{-4}$ T outside the CCiPM. Therefore, if the measuring magnetic field is not greater than the noise level, the measurement result contains a large systematic error. Because the magnetic field of the CCiPM is weak at the center, the difficulty of measuring the field at the center increases a lot compared with the previous measurement result of PSM1 in Fig. 3.19. The magnetic field result of PSM1 is also normalized under a condition of 3000 A current and compared with the result of the CCiPM, which is shown in Fig. 7.20.

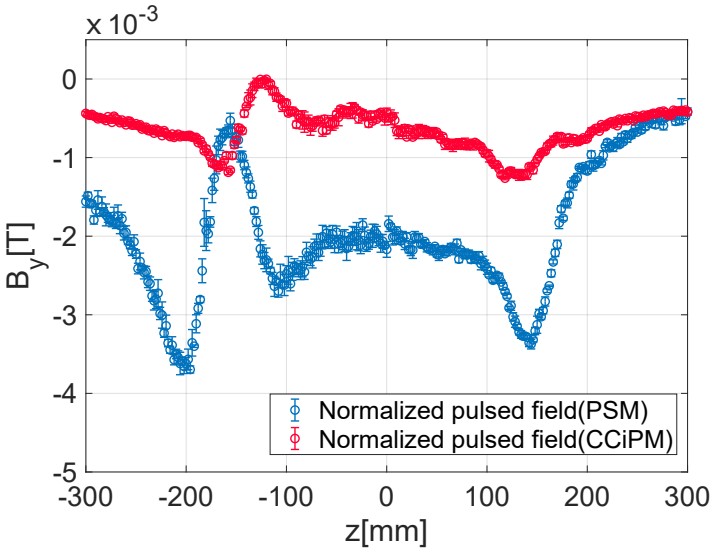


FIGURE 7.20: Longitudinal pulsed magnetic field distribution of PSM1 and CCiPM at $x$=0 mm.

The other problem is that the off-axis pulsed magnetic field is only 80% of the simulation data and DC magnetic field. Based on the previous research, the eddy current effect of the coating should be almost zero. As for the electromagnetic noise, the noise level has small influence on the off-axis measurement, because the amplitude of the integrated voltage signal is much larger than the amplitude of the noise. For example, in Fig. 7.15, at $x$=12 mm, the peak value of the integrated voltage signal is 50.8 nV $\cdot$ s; at $x$=0 mm, the amplitude of the integrated voltage signal that is mainly induced by the noise whose amplitude is 2.0 nV $\cdot$ s, the error ratio is only 4.0%. Therefore, the electromagnetic noise does not have a large effect on the off-axis pulsed magnetic field measurement.

The magnetic field gradient may also influence the pulsed magnetic field measurement. It is assumed that the magnetic field is uniform in the measuring area of the main coil.

Owing to the nature of a multipole magnet, there is still a variation of the magnetic field. The influence on the measurement circuit cannot be evaluated properly. The gradient of an octupole magnetic field is larger than a sextupole magnetic field, which may reduce the accuracy of the measurement. Fig. 7.15 gives the horizontal magnetic field (simulation) distributions of the PSM1 and CCiPM. Because the width of the coil is 3.2 mm, if the center of the probe is located at $x$=10 mm, the magnetic field gradients of the PSM1 and CCiPM across the coil are 3.66 T/m and 3.92 T/m, respectively. The gradient of the CCiPM is 1.07 times larger than that of the CCiPM, which is not a big difference. Therefore, it is supposed that the issue of pulsed magnetic field measurement is not related to the magnetic field gradient of the CCiPM.

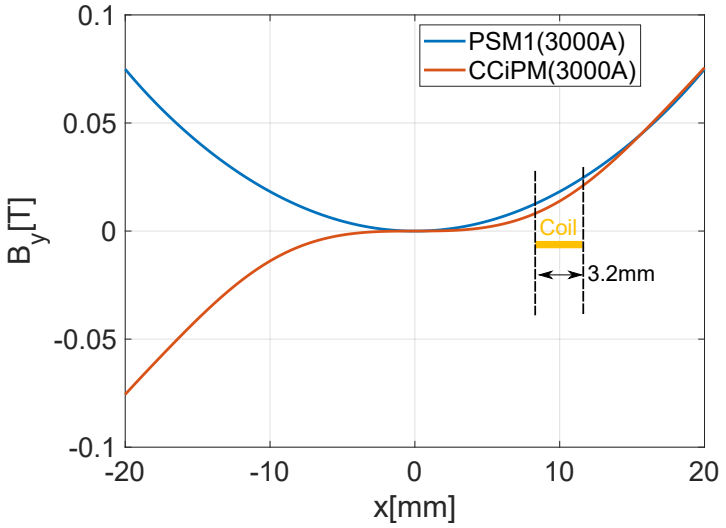


FIGURE 7.21: Horizontal magnetic field distribution (simulation) of PSM1 and CCiPM at $z$=0 mm.

Finally, the integrated voltage signal is compared with the current signal of CT, which is shown in Fig. 7.22. The CT signal is not identical to the integrated voltage signal. Compared with the result in the PSM1 measurement (Fig. 3.9), the ringing of the current signal becomes severe. Because the small inductance of the CCiPM, the pulse width is 0.8 µs which is narrow than that in the PSM1 measurement. Owing to the performance of the power source, the output current is not a half-sine wave shape, it represents that the pulsed magnetic field is not a half-sine wave shape. Therefore, the calculation of the peak magnetic field is badly affected. The result also shows that the pick-up probe is not capable of reconstructing a signal induced by an external pulsed magnetic field whose pulse width is smaller than 1 µs. Consequently, the ringing of the current signal is

the most likely cause of the problem in the off-axis pulsed magnetic field measurement. To suppress the ringing of the current signal, an impedance load should be added in the circuit to match the power source.

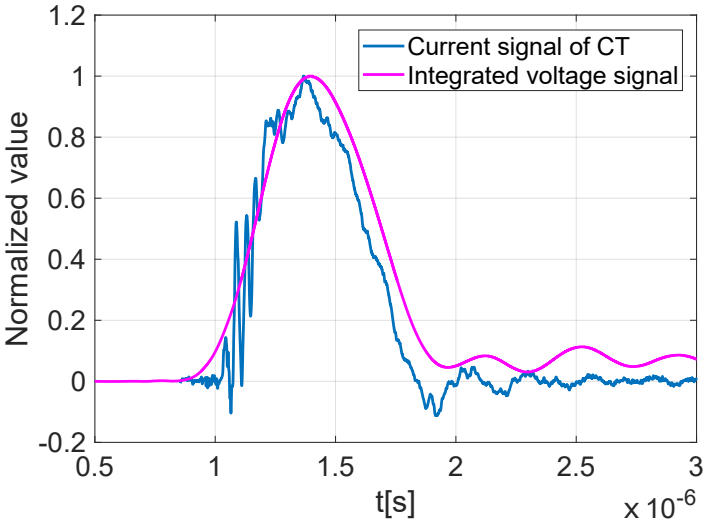


FIGURE 7.22: Comparison between the CT signal and integrated voltage signal in the CCiPM measurement ($x$=12 mm, $y$=0 mm, $z$=0 mm).

## 7.5 Installation and Beam Test in the Ring.

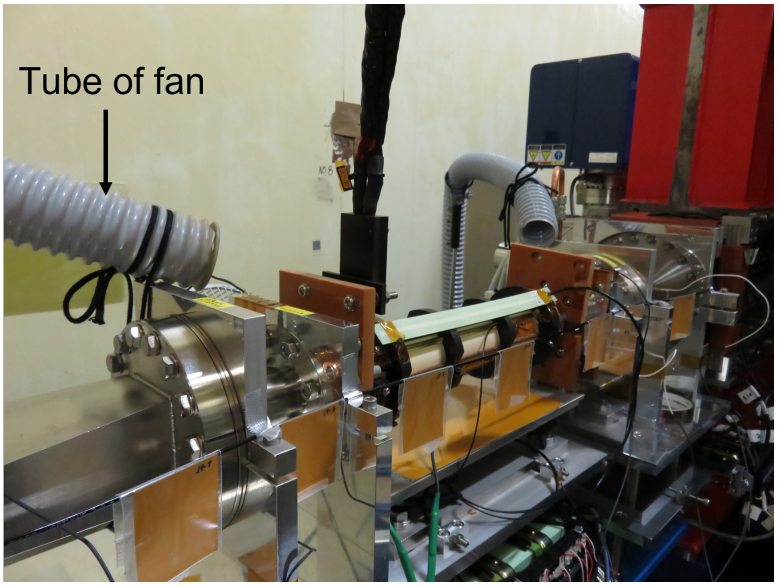


FIGURE 7.23: Photograph of the CCiPM in the PF ring.

Although some issues should be solved in the magnetic field measurement, the mechanical performance test allows the CCiPM to be installed in a storage ring. Fig. 7.23 shows the CCiPM installed in the PF ring. There was no leakage during the operation.

The fan is used to prevent the CCiPM overheating during the operation. The temperature of the chamber was less than 60 °C in the multi-bunch operation. In hybrid mode: a multi-bunch train (420 mA) + one single bunch(30 mA), the temperature increased to 80 °C. After turning on the fan, the temperature was lower than 60 °C.

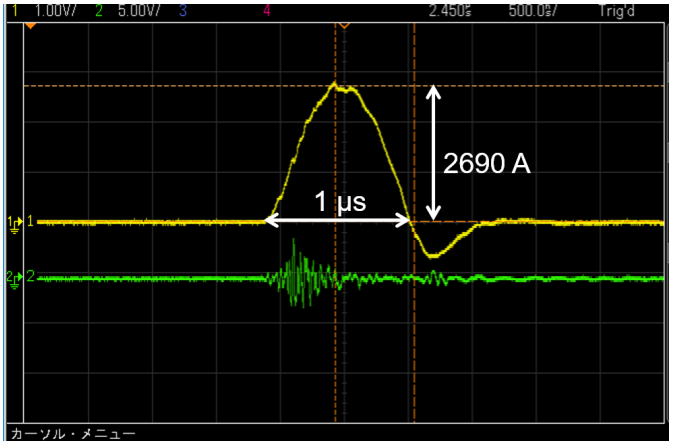


FIGURE 7.24: Screenshot of the oscilloscope in the current excitation test with a 1 µs pulse width.

The current excitation test with a 1 µs pulse width was also conducted. Fig. 7.24 shows the screenshot of the oscilloscope of the CT signal in the current excitation test. The peak current reached to 2690 A, and electrical discharge did not occur. Because there is a limitation of the power source, the peak current cannot be higher than 2700 A. In the future, a power source will be updated to supply a peak current more than 3000 A.

# Chapter 8

# Conclusion and Prospects

## 8.1 Conclusion

A new pick-up probe was developed to measure pulsed magnetic field precisely as a supportive technique for PMM injection. The subtraction method is simple and reliable for measuring a pulsed magnetic field with a 3.2 mm × 5.8 mm coil when the pulse width of the current is 1 µs. To figure out the problems of the PSM injection in PF ring, the pulsed magnetic field of PSM1 was measured with the probe. The signal of the eddy-current magnetic field generated by the lamination steel was observed in the experiment. The eddy current effect of the circular coating is negligible. Based on the measurement and simulation results, it is concluded that the eddy-current magnetic field generated by the iron-core induced the stored beam oscillation in the PSM1 injection experiment. It is also found that the eddy current effect of the coating is not only associated with the shape but also with the order of magnetic field.

To apply PMM injection in next generation light source, it is necessary to develop an air-core pulsed multipole magnet. Based on the current research of CCiPM which was developed for a dipole fast kicker, a CCiPM can be designed as an octupole pulsed magnet for beam injection. The first target is to produce a prototype that has a similar

off-axis kick effect compared with PSM1. However, the inductance of the initial prototype is 11.15 µH. To reduce the inductance, an optimized design was proposed by adding four additional conductors on the chamber. After the optimization of the busbar, the integrated field strength is expected to be less than 10 µT · m at the center.

The prototype of the octupole CCiPM was fabricated successfully. Several offline tests have been performed, which showed that it has 1.45 µH inductance, good vacuum tightness and heat durability. The DC and pulsed magnetic fields were measured, and some challenges appeared. The DC magnetic field is almost consistent with the simulation. However, there is a small irregular magnetic field in the longitudinal distribution at the center. It is highly possible that the problem is caused by the joint between the coil and metal block. In the pulsed magnetic field measurement, the resolution power of the probe is not enough for measuring the magnetic field at the center. In addition, the ringing of the output current signal disturbs the measurement circuit to obtain an accurate off-axis magnetic field. These issues should be optimized to improve the magnetic field property.

## 8.2 Prospects

### 8.2.1 Improvement for the Magnetic Field Measurement

For the DC magnetic field, it is important to investigate the effect of the joint between the coil and metal block on the DC magnetic field of CCiPM.

According to the analysis in Sec. 7.4, several plans are considered to improve the pulsed magnetic field measurement.

1. Use a pulsed power source whose output current has a several microseconds pulse duration to improve the S/N. The main field signal is expected to be increased at the center.

2. To measure the off-axis pulsed magnetic field correctly, the ringing of the current signal should be suppressed. An impedance load can be added in the circuit to match the power source.

### 8.2.2 Development of Insulation Components

The insulation is very important for the performance of CCiPM. To reduce the magnetic field deformation generated by the busbar structure, the gap of the busbar is quite narrow. Therefore, there is a risk of electrical discharge. The surface of the busbar should be insulated well. In addition, the internal coating of CCiPM also has a risk of electrical discharge, though there is a gap between the conductor and coating. The kick effect of CCiPM is limited if the current is expected to be more than 4000 A. A feasible plan is that an insulated coating is added between the titanium coating and the ceramic. This is very meaningful but full of challenge.

### 8.2.3 Injection Experiment

If there is a power source that can supply a current that meets our requirement, the injection experiment should be conducted to examine the kick effect of the CCiPM. In addition, the perturbation on the stored beam can be estimated from the oscillation.

# Appendix A

# Computation of Beam Envelope in a Ring

Let $v = (x, p_x, y, p_y, z, \delta)$ be the six-dimensional variable describing the location of a particle in phase space. It is assumed that designed particle motion is $(0, 0, 0, 0, 0, 0)$. In a linear Hamiltonian system, the final coordinates $v^f$ are given by

$$v^f = Mv^i \tag{A.1}$$

where $M$ is a $6 \times 6$ matrix. M also satisfies the sympletic condition

$$M^T S M = S \tag{A.2}$$

where $M^T$ is the transpose of $M$ and $S$ is a $6 \times 6$ symplectic matrix.

Consider a discrete distribution of $N$ particles. The quadratic moments of particle distribution are given by

$$\langle v_a v_b \rangle = \frac{1}{N} \sum_{i=1}^{N} (v_a^{(i)} v_b^{(i)}) \tag{A.3}$$

At the end of beamline, it becomes

$$(\langle v_a v_b \rangle)^f = \frac{1}{N} \sum_{i=1}^{N} \sum_{c,d} (M_{ac} v_c^{(i)} M_{bd} v_d^{(i)}) \tag{A.4}$$

It can be written in a vector expression as follows:

$$(\langle \boldsymbol{v}\boldsymbol{v}^T \rangle)^f = M \langle \boldsymbol{v}\boldsymbol{v}^T \rangle M^T \tag{A.5}$$

or

$$\Sigma^f = M \Sigma_0 M^T \tag{A.6}$$

where $\Sigma_0$ is initial beam distribution matrix, and $\Sigma^f$ is beam distribution in the end.

In a ring, the beam distribution keeps same at a specific position due to the periodic condition. Because there is a closed orbit distortion, rigorously, the beam distribution matrix is given by

$$\begin{aligned} \Sigma &= \langle \boldsymbol{u}\boldsymbol{u}^T \rangle \\ \boldsymbol{u} &= \boldsymbol{v} - \boldsymbol{v}_0 \end{aligned} \tag{A.7}$$

where $\boldsymbol{v}_0$ is the particle motion at closed orbit.

However, Eq. A.6 still cannot be applied directly. The particle's energy undergoes a small fluctuation $\delta$ especially when it passes a bending magnet. If the quantum fluctuation happens at the end of beamline, Eq. A.6 can be replaced by

$$\Sigma^f = M \Sigma_0 M^T + dB \tag{A.8}$$

where $dB$ is the matrix that influences the final beam distribution. Because the transverse motion is conserved during this process, $dB_{66} = \langle \delta^2 \rangle$ is the only nonzero component.

$$dB = \begin{bmatrix} 0 & \cdots & 0 \\ \vdots & \ddots & \vdots \\ 0 & \cdots & \langle \delta^2 \rangle \end{bmatrix} \tag{A.9}$$

According to quantum mechanics, $dB_{66}$ is calculated as

$$\begin{aligned} dB_{66} &= K'(1+\delta)^4 |\frac{B_y}{B_0}|^3 \frac{\partial H}{\partial \delta} ds \\ K' &= 4.132097 \times 10^{-7} E_0^5 \end{aligned} \tag{A.10}$$

where $B_0$ is the designed magnetic field of bending magnet, $H$ is the Hamiltonian motion of particle, and $E_0$ is the designed particle energy in GeV unit.

Therefore, if the fluctuation happens at position 1, such an equation is obtained.

$$\Sigma_1 = M_{01}\Sigma_0 M_{01}^T + dB_1 \tag{A.11}$$

where $M_{01}$ is the transfer matrix from initial position to position 1.

At next position 2, a new equation is written as

$$\begin{aligned} \Sigma_2 =& M_{12}\Sigma_1 M_{12}^T + M_{12} dB_1 M_{12}^T \\ =& M_{12}(M_{01}\Sigma_0 M_{01}^T + dB_1) M_{12}^T + dB_2 \\ =& M_{02}\Sigma_0 M_{02}^T + dB_2 \end{aligned} \tag{A.12}$$

Repeat this calculation after one turn, it becomes

$$\Sigma = M\Sigma M^T + B \tag{A.13}$$

# Appendix B

# Decouple Matrix

Define $M$ is a random transfer matrix. $M$ satisfies the stable condition in accelerator that the eigenvalue is a complex number. $f(z)$ is a function, and the number of variables of $z$ is same with the dimension of $M$. Because the transformation of $M$ is linear, such an equation is obtained

$$\mathscr{M} f(z) = f(Mz) \tag{B.1}$$

where $\mathscr{M}$ is a map acting on the function. Usually, this type of map is represented by a Lie operator.

In accelerator physics, invariant $\varepsilon$ can be expressed by a polynomial constructed by motions of particle in a linear Hamiltonian system. It's clear that any invariant obeys

$$\mathscr{M}\varepsilon = \varepsilon \circ M = \varepsilon \tag{B.2}$$

where symbol $\circ$ means substitution. It is because that particle's motions are transformed by the matrix $M$, the invariant value is still preserved.

Then $\mathscr{M}$ acts on a linear function without any constant part. For simplicity, the function $f$ is only one degree of freedom, which can be given by

$$f(z) = v_1 z_1 + v_2 z_2. \tag{B.3}$$

According to Eq. B.1, the transformation on $f$ can be written as:

$$\begin{aligned}(\mathscr{M}f)(z) = f(Mz) = \sum_{i=1,2}\Big(v_1 M_{1i} z_i + v_2 M_{2i} z_i\Big) \\ =(M^T v)_1 z_1 + (M^T v)_2 z_2\end{aligned} \tag{B.4}$$

Combing Eq. B.3 and Eq. B.4, if the array $v$ are components of $f$, a new equation is given by

$$\mathscr{M}(v) = M^T v \tag{B.5}$$

Thus, the search for the linear eigenfunctions of $\mathscr{M}$ is equivalent to the search of the eigenvectors of $M^T$. As for $M^T$, it satisfies

$$M^T w = \lambda w, \qquad w = w_r + i w_i \tag{B.6}$$

where $w$ is the eigenvector of $M^T$, it has real part $w_r$ and imaginary part $w_i$, and $\lambda$ is the eigenvalue.

Based on the value of eigenvector, the following functions are constructed:

$$\begin{aligned} g_1(z) &= \frac{w_r \cdot z}{|[w_r \cdot z, w_i \cdot z]|^{1/2}} \\ g_2(z) &= \frac{w_i \cdot z}{\sigma|[w_r \cdot z, w_i \cdot z]|^{1/2}} \\ \text{where } \sigma &= sgn[w_r \cdot z, w_i \cdot z] \end{aligned} \tag{B.7}$$

The $\sigma$ is sign function, if $\sigma = -1$, it will exchange the eigenvector and eigenvalue $\{\lambda, w\}$ to $\{\lambda^*, w^*\}$. The denominator part is a square root of a Poisson bracket, which is important for a canonical transformation. In fact, these functions give new canonical variable after transformation. For example , the new variable in one degree of freedom is given by

$$\begin{aligned} Z_1 &= g_1(z_1) + g_1(z_2) \\ Z_2 &= g_2(z_1) + g_2(z_2) \\ Z_1^2 + Z_2^2 &= \varepsilon \end{aligned} \tag{B.8}$$

where $Z_1$ and $Z_2$ are new canonical variables in a normalized plane after transformation.

To prove this, firstly, based on Eq. B.4, Eq. B.5, and Eq. B.6, the following relationship is obtained:

$$(\mathscr{M} f)(z) = \lambda(w_r + iw_i) \tag{B.9}$$

The eigenfunction of $\mathscr{M}$ is constructed by:

$$\begin{aligned} f_{\pm}(z) &= g_1(z) \pm ig_2(z) \\ \mathscr{M} f_{\pm} &= \exp(\mp i\mu_0) f_{\pm} \end{aligned} \tag{B.10}$$

where $\exp(\mp i\mu_0)$ are the eigenvalues of $M^T$. $\exp(-i\mu_0)$ is related to the eigenvector $f_+(z)$ and $\exp(+i\mu_0)$ is associated with the eigenvector $f_-(z)$.

Then it is trivial to prove that the invariant is given by

$$Z_1^2 + Z_2^2 = (f_+ f_-)(z) \tag{B.11}$$

If a matrix $M$ acts on the initial motion $z$, the right part of Eq. B.11 becomes

$$\begin{aligned} (f_+ f_-)(Mz) =& (\mathscr{M} f_+ f_-)(z) \\ =& (\{\mathscr{M} f_+\}\{\mathscr{M} f_-\})(z) \\ =& (\{\exp(-i\mu_0) f_+\}\{\exp(+i\mu_0) f_-\})(z) \\ =& (f_+ f_-)(z) \end{aligned} \tag{B.12}$$

It means that the value is preserved after a matrix transformation, which is an invariant.

It has been proved that $Z_1$ and $Z_2$ are new variables in a normalized plane after canonical transformation. In a higher dimension, the treatment of decoupling matrix is similar. Calculate the eigenvectors of $M^T$, then construct a decoupling matrix $A^{-1}$ by the eigenvectors, finally the rotation matrix $R$ related to the tune is given by

$$R = A^{-1} M A \tag{B.13}$$

# Appendix C

# Perturbation on Stored Beam by Different Pulsed Magnet

If the PMM injection is a one-turn kick, the perturbation from the pulsed magnet will only influence the stored beam at the first turn.

The optics parameters and layout around injection part of the PF ring are shown in Fig. C.1. In the physical design, the electron beam is injected from the BT line. The off-axis position is 15 mm where it passes by PSM. The designed integrated magnetic field is 0.12 mT $\cdot$ m at the kick position.

The strength parameter of normal sextupole magnet defined in SAD is

$$K_2 = \frac{B'' L}{B_0 \rho} = \frac{0.3}{P[\mathrm{GeV/c}]} B''[\mathrm{T/m^2}] L[\mathrm{m}] \tag{C.1}$$

where $B_0\rho$ is the magnetic rigidity, $P$ is the momentum of the particle, $L$ is the length of the magnet, and $B''$ is the second derivative of magnetic field expanded from center. According to the designed integrated magnetic field, the $K_2$ is 13 $\mathrm{m}^{-2}$.

The PSM injection has been conducted successfully. In fact, a PQM and POM can also perform injection if they provide a same kick effect at the kick position. However, the

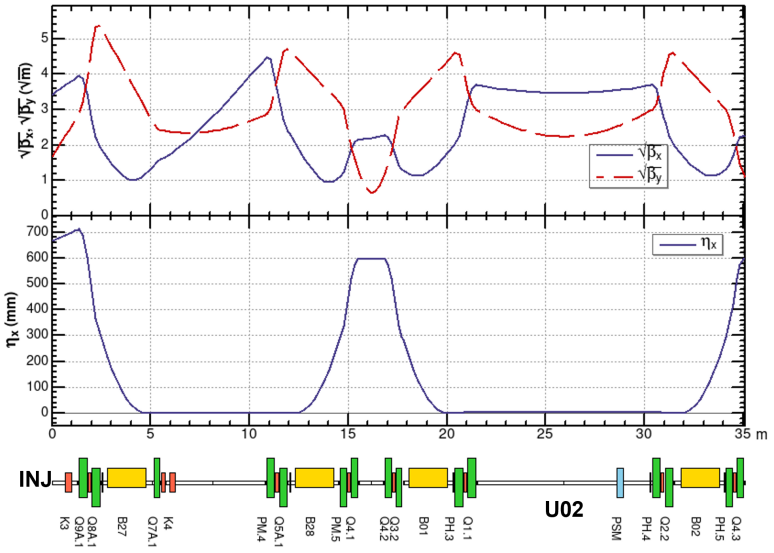


FIGURE C.1: Optics parameters and layout around injection part of the PF ring.

perturbation experienced by the stored beam depends on the type of magnet. Parameters of different magnet that has same off-axis kick effect are summarized in Table C.1.

TABLE C.1: Parameters of the PQM, PSM, and POM

| Magnet | Expression of $B_y$ in the midplane | Strength parameter in SAD |
|---|---|---|
| PQM | $B^{'}x$ | $K_1 = 0.096[\mathrm{m}^{-1}]$ |
| PSM | $\frac{1}{2}B^{''}x^2$ | $K_2 = 13[\mathrm{m}^{-2}]$ |
| POM | $\frac{1}{6}B^{'''}x^3$ | $K_3 = 2560[\mathrm{m}^{-3}]$ |

The natural bunch was tracked and received the kick from the pulsed multipole magnets at the first turn. The beam profile was observed until 50th turn at Undulator02. The stored beam size oscillation and beam centroid were checked in the tracking, which were calculated as

$$\sigma_x = \sqrt{\frac{\sum(x_i - x_0)^2}{N}} \qquad \bar{x} = \frac{\sum(x_i - x_0)}{N} \tag{C.2}$$

where $x_0$ is the closed orbit at Undulator-2, $x_i$ is the position of one single particle, and $N$ is the particle number.

Fig. C.2 shows the stored beam size oscillation induced by different pulsed magnets. In the PQM's condition, there is a large beam size oscillation, which is almost 0.8 mm and similar with the PQM injection at PF-AR. Because quadrupole magnet cannot provide

a nearly zero magnetic field region around the center. As for the PSM and POM, the stored beam size stayed stable in tracking.

The beam centroid oscillation is shown in Fig. C.3. Although, the PQM induced a large beam size oscillation, the beam centroid oscillation is less than 10 µm. The PSM has a maximum oscillation amplitude that is about 40 µm. As for the condition of POM, the oscillation amplitude is almost zero, which is the most superior.

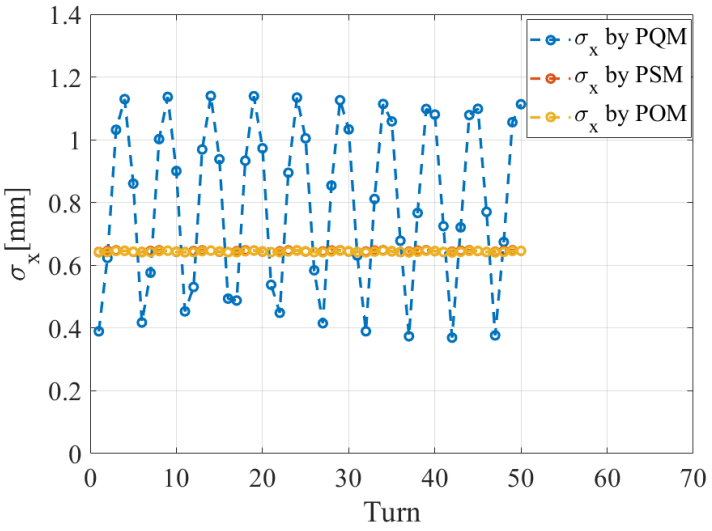


FIGURE C.2: Beam size oscillation in tracking.

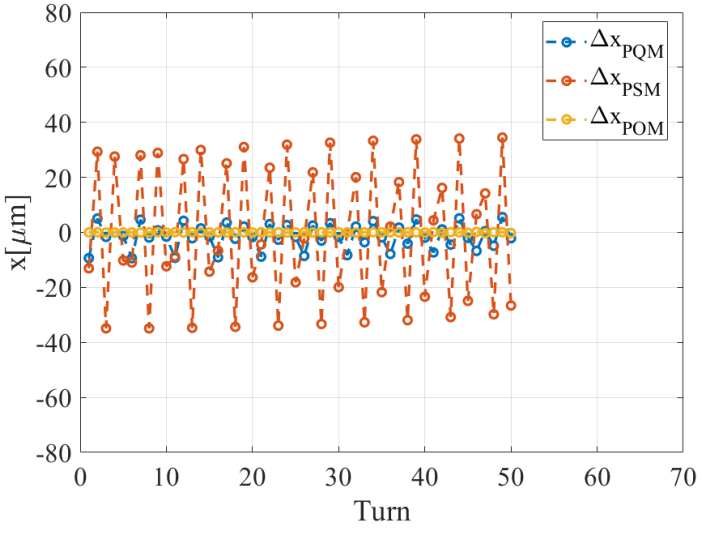


FIGURE C.3: Beam centroid oscillation in tracking.

Although some issues like field errors, misalignment, and stored beam instability can influence the stored beam properties in reality. From the analysis above, it is concluded that POM is the most suitable choice to realize a transparent beam injection.

# Appendix D

# Magnetic field measurement of CCiPM-D30

Fig. D.1 shows the picture of the DC magnetic field measurement. The experimental coordinate is marked, and origin is located at the center of the CCiPM. The measurement system is same with the PSM measurement system.

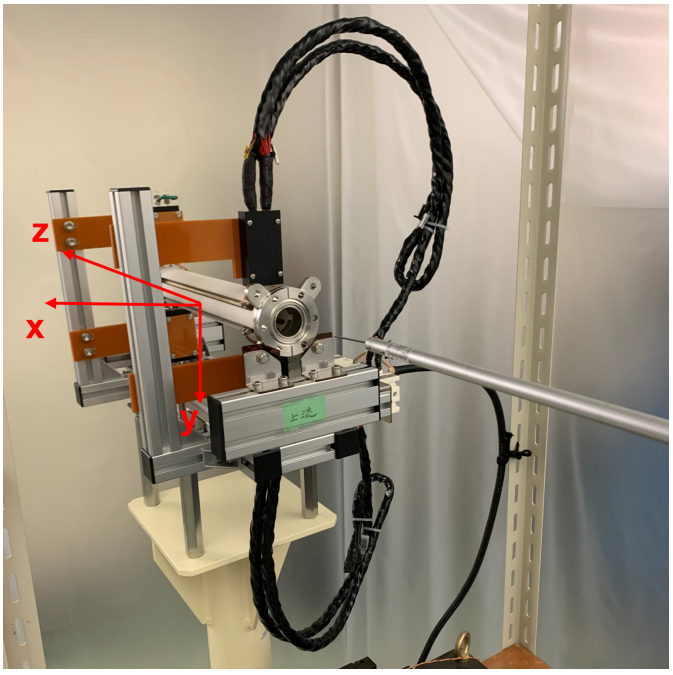


FIGURE D.1: Picture of the DC magnetic field measurement.

In order to get a detailed magnetic field distribution of CCiPM-D30, the DC and pulsed magnetic field mapping were both performed. The measurement region was limited. Otherwise, the probe may hit the chamber. The results of the DC magnetic field mapping ($-6 \leq x \leq 5$ mm, $y$=0 mm, $-290 \leq z \leq 160$ mm) and pulsed magnetic field mapping ($-5 \leq x \leq 5$ mm, $y$=0 mm, $-240 \leq z \leq 200$ mm) are shown in Fig. D.2 and Fig. D.3, respectively. In the DC magnetic field measurement, the supplied current was 15A. In the pulsed magnetic field measurement, the peak value of the supplied current was 150 A. All data is normalized under the condition of a 3000 A current.

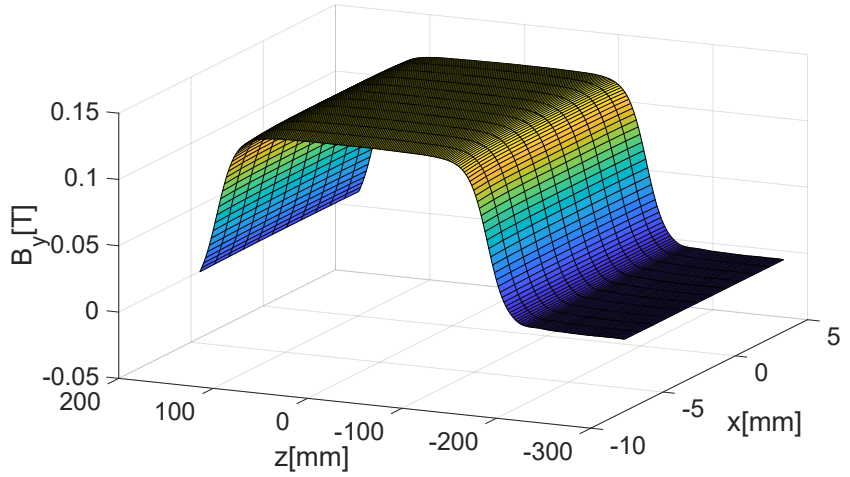


FIGURE D.2: Result of the DC magnetic field mapping.

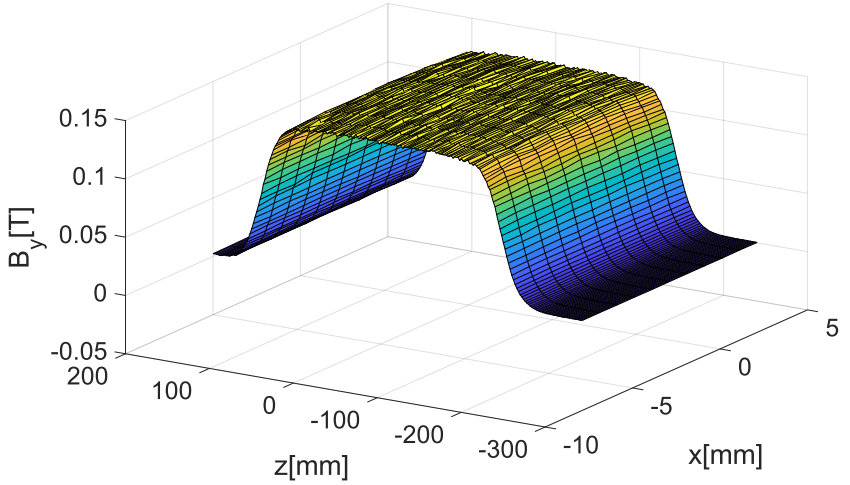


FIGURE D.3: Result of the pulsed magnetic field mapping.

Fig. D.1 shows the longitudinal distributions of $B_x$ at $x$=0 mm. The distribution of the normalized pulsed magnetic field is well consistent with the distribution of the normalized DC magnetic field. The results of the integrated magnetic field are used to calculate the kick effect of CCiPM-D30 shown in Fig. D.5.

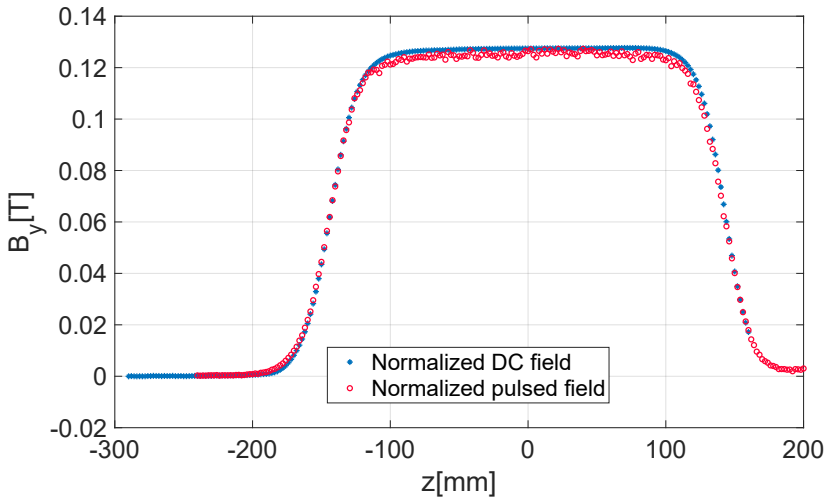


FIGURE D.4: Longitudinal distributions of the $B_y$ at $x$=0 mm.

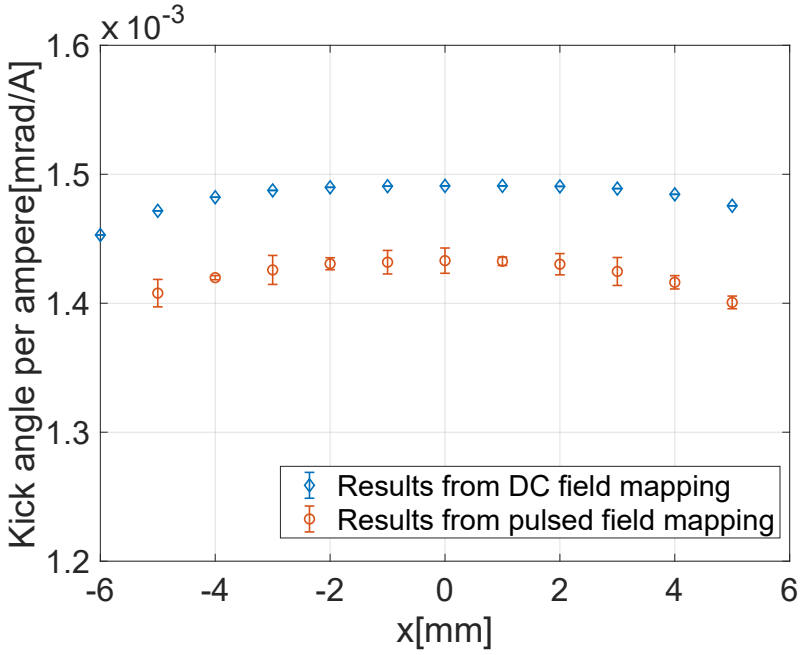


FIGURE D.5: Kick effect of CCiPM-D30 calculated from the DC and pulsed magnetic field mapping data.

# Bibliography


[1] K.-J. Kim, Characteristics of synchrotron radiation, in: AIP Conf Proc. 184, 565 (1989).
URL https://aip.scitation.org/doi/pdf/10.1063/1.38046

[2] S. Nakamura, et al., Present Status of the 1 GeV Synchrotron Radiation Source at SORTEC, in: Proceedings of EPAC08, pp. 472–474.
URL https://accelconf.web.cern.ch/e90/PDF/EPAC1990_0472.PDF

[3] L. Emery, M. Borland, Upgrade Opportunities at the Advanced Photon Source Made Possible by Top-Up Operations, in: Proceedings of EPAC 2002, 2002, pp. 218–220.
URL http://accelconf.web.cern.ch/e02/PAPERS/TUALA003.pdf

[4] H. Ohkuma, Top-Up Operation in Light Sources, in: Proceedings of EPAC08, pp. 36–40.
URL http://accelconf.web.cern.ch/e08/papers/mozcg01.pdf

[5] S. Y. Lee, Accelerator physics, 2nd Edition, World Scientific, Hackensack, N.J, 2004.

[6] H. Tanaka, et al., Suppression of injection bump leakage caused by sextupole magnets within a bump orbit, Nucl. Instrum. Methods Phys. Res., Sect. A 539 (3) (2005) 547–557.
URL https://linkinghub.elsevier.com/retrieve/pii/S0168900204023617

[7] Weihua Jiang, et al., Compact solid-State switched pulsed power and its applications, Proc. IEEE 92 (7) (2004) 1180–1196.
URL http://ieeexplore.ieee.org/document/1306686/

[8] C. Mitsuda, K. Kobayashi, K. Soutome, Suppression of stored beam oscillation at injection in the SPring-8 storage ring, in: Proceedings of the 11th Annual Meeting

of Particle Accelerator Society of Japan, 2014.
URL https://www.pasj.jp/web_publish/pasj2014/proceedings/PDF/MOOM/MOOM10.pdf

[9] Y.-G. Son, et al., Suppression of stored-beam oscillation and observation of flux improvement during top-up injection, Phys. Rev. Accel. Beams 20 (8) (2017) 082803.
URL https://link.aps.org/doi/10.1103/PhysRevAccelBeams.20.082803

[10] Z. Duan, Survey of Injection Schemes for Next-generation Light Source Rings, in: 60th ICFA Advanced Beam Dynamics Workshop on Future Light Sources, 2018.
URL https://accelconf.web.cern.ch/fls2018/talks/tua1wb01_talk.pdf

[11] D. Einfeld, M. Plesko, J. Schaper, First multi-bend achromat lattice consideration, Journal of Synchrotron Radiation 21 (5) (2014) 856–861.
URL https://doi.org/10.1107/S160057751401193X

[12] M. Paraliev, et al., Development of Fast and Super-Fast Kicker System for SLS 2.0 Injection, in: Proceedings of the 12th International Particle Accelerator Conference, Vol. IPAC2021, 2021, pp. 2889–2892.
URL https://jacow.org/ipac2021/doi/JACoW-IPAC2021-WEPAB122.html

[13] G. C. Pappas, et al., Fast Kicker Systems for ALS-U, in: Proceedings of the 5th Int. Particle Accelerator Conf., 2014.
URL https://accelconf.web.cern.ch/IPAC2014/papers/mopme083.pdf

[14] L. Wang, et al., A 300 mm Long Prototype Strip-Line Kicker for the Heps Injection System, in: Proceedings of the 10th Int. Particle Accelerator Conf., Vol. IPAC2019, 2019.
URL http://jacow.org/ipac2019/doi/JACoW-IPAC2019-THPRB026.html

[15] W. Liu, et al., Development of a stripline kicker for the Hefei Advanced Light Facility, Nucl. Instrum. Methods Phys. Res., Sect. A 961 (2020) 163670.
URL https://linkinghub.elsevier.com/retrieve/pii/S0168900220302382

[16] K. Tsuchiya, et al., Present Status of the KEK PF-Ring and PF-AR, in: Proceedings of the 4th Int. Particle Accelerator Conf., 2013.
URL http://jacow.org/ipac2019/doi/JACoW-IPAC2019-THPRB026.html

[17] K. Harada, et al., New injection scheme using a pulsed quadrupole magnet in electron storage rings, Phys. Rev. ST Accel. Beams 10 (12) (2007) 123501.
URL https://link.aps.org/doi/10.1103/PhysRevSTAB.10.123501

[18] H. Takaki, et al., Beam injection with a pulsed sextupole magnet in an electron storage ring, Phys. Rev. ST Accel. Beams 13 (2) (2010) 020705.
URL https://link.aps.org/doi/10.1103/PhysRevSTAB.13.020705

[19] H. Takaki, Development of injection system by a pulsed sextupole magnet in electrong storage ring, Ph.D. thesis, The Graduate University for Advanced Studies (2010).

[20] S. C. Leemann, Pulsed sextupole injection for Sweden's new light source MAX IV, Phys. Rev. ST Accel. Beams 15 (5) (2012) 050705.
URL https://link.aps.org/doi/10.1103/PhysRevSTAB.15.050705

[21] S. White, et al., Transparent Injection for ESRF-EBS, in: Proceedings of the 10th Int. Particle Accelerator Conf., Vol. IPAC2019, 2019.
URL http://jacow.org/ipac2019/doi/JACoW-IPAC2019-MOPGW008.html

[22] X. R. Resende, et al., Study of a Pulsed Sextupole Magnet Injection System for LNLS, in: Proceedings of the 2nd Int. Particle Accelerator Conf., 2011.
URL https://accelconf.web.cern.ch/ipac2011/papers/thpc139.pdf

[23] C. Sun, et al., PULSED MULTIPOLE INJECTION FOR ALS UPGRADE, in: Proceedings of the 1st Int. Particle Accelerator Conf.
URL https://accelconf.web.cern.ch/IPAC10/papers/wepea068.pdf

[24] A. Saá Hernández, M. Aiba, Investigation of the Injection Scheme for SLS 2.0, in: Proceedings of the 6th Int. Particle Accelerator Conf., Vol. IPAC2015, 2015.
URL http://jacow.org/ipac2015/doi/JACoW-IPAC2015-TUPJE046.html

[25] Y. Jiao, G. Xu, Pulsed sextupole injection for Beijing Advanced Photon Source with ultralow emittance, Chinese Phys. C 37 (11) (2013) 117005.
URL https://iopscience.iop.org/article/10.1088/1674-1137/37/11/117005

[26] N. Yamamoto, et al., Beam injection with pulsed multipole magnet at UVSOR-III, Nucl. Instrum. Methods Phys. Res., Sect. A 767 (2014) 26–33.
URL https://linkinghub.elsevier.com/retrieve/pii/S0168900214009176

[27] N. Yamamoto, et al., Design Study of Pulsed Multipole Injection for Aichi SR, in: Proceedings of the 5th Int. Particle Accelerator Conf., 2014, pp. 1962–1964.
URL https://accelconf.web.cern.ch/IPAC2014/papers/wepro011.pdf

[28] A. Mochihashi, et al., Perturbation to Stored Beam by Pulse Sextupole Magnet and Disturbance of the Sextupole Magnetic Field in Aichi Synchrotron Radiation Center, in: Proceedings of the 9th Int. Particle Accelerator Conf., 2018, pp. 4232–4234.
URL https://accelconf.web.cern.ch/ipac2018/papers/thpmf069.pdf

[29] O. Dressler, et al., Development of a Non-Linear Kicker System to Facilitate a New Injection Scheme for the BESSY II Storage Ring, in: Proceedings of the 2nd Int. Particle Accelerator Conf., 2011, pp. 3394–3396.
URL https://accelconf.web.cern.ch/ipac2011/papers/thpo024.pdf

[30] P. Alexandre, et al., Transparent top-up injection into a fourth-generation storage ring, Nucl. Instrum. Methods Phys. Res., Sect. A 986 (2021) 164739. doi:10.1016/j.nima.2020.164739.
URL https://linkinghub.elsevier.com/retrieve/pii/S0168900220311360

[31] C. Sun, et al., Optimizations of nonlinear kicker injection for synchrotron light sources, Phys. Rev. Accel. Beams 23 (1) (2020) 010702. doi:10.1103/PhysRevAccelBeams.23.010702.
URL https://link.aps.org/doi/10.1103/PhysRevAccelBeams.23.010702

[32] L. Liu, et al., Injection Dynamics for Sirius Using a Nonlinear Kicker, in: Proceedings of the 7th Int. Particle Accelerator Conf., 2016.
URL https://accelconf.web.cern.ch/ipac2016/papers/thpmr011.pdf

[33] Wikipedia (Electrical steel).
URL https://en.wikipedia.org/wiki/Electrical_steel

[34] R. H. Bishop (Ed.), The mechatronics handbook, CRC Press, Boca Raton, Fla, 2002.

[35] M. Buzio, Fabrication and calibration of search coils (2011).
URL https://arxiv.org/abs/1104.0803

[36] J. DiMarco, et al., A Fast-Sampling, Fixed Coil Array for Measuring the AC Field of Fermilab Booster Corrector Magnets, IEEE Trans. Appl. Supercond. 18 (2) (2008) 1633–1636.
URL http://ieeexplore.ieee.org/document/4520236/

[37] H. Liang, et al., Design of the Integral Field Measurement System of Dipole Magnets, IEEE Trans. Appl. Supercond. 28 (3) (Apr. 2018).
URL http://ieeexplore.ieee.org/document/8272447/

[38] P. Chengcheng, et al., Measurement system for SSRF pulsed magnets, Nuclear Science and Techniques 18 (6) (2007) 321–325.
URL https://linkinghub.elsevier.com/retrieve/pii/S1001804208600019

[39] T. Takayanagi, et al., Improvement of the Shift Bump Magnetic Field for a Closed Bump Orbit of the 3-GeV RCS in J-PARC, IEEE Trans. Appl. Supercond. 18 (2) (2008) 306–309.
URL http://ieeexplore.ieee.org/document/4512959/

[40] Introduction to Accelerators II (Normal-conducting Magnet) in SOKENDAI.
URL https://www2.kek.jp/accl/sokendai/corecurriculum/corecurri20/corecurri20_2.html

[41] Datasheets of F.W. Bell's fourth generation gaussmeter probes.
URL https://www.atecorp.com/atecorp/media/pdfs/data-sheets/fw-bell-9000_datasheet.pdf

[42] KEYSIGHT TECHNOLOGIES, https://www.keysight.com/jp/ja/home.html.
URL https://www.keysight.com/jp/ja/home.html

[43] G. Moritz, Eddy currents in accelerator magnets, Tech. Rep. CERN-2010-004, pp. 103-140 (Jun. 2009).
URL https://cds.cern.ch/record/1335027/files/103.pdf

[44] Y. Chung, J. Galayda, Effect of eddy current in the laminations on the magnet field, Tech. Rep. LS–200, 89553 (Apr. 1992).
URL http://www.osti.gov/servlets/purl/89553-dQmBok/webviewable/

[45] Strategic Accelerator Design (SAD).
URL https://acc-physics.kek.jp/SAD/

[46] K. Ohmi, K. Hirata, K. Oide, From the beam-envelope matrix to synchrotron-radiation integrals, Phys. Rev. E 49 (1) (1994) 751–765.
URL https://link.aps.org/doi/10.1103/PhysRevE.49.751

[47] E. Forest, From Tracking Code to Analysis, Springer Japan, 2016.

[48] D. A. Edwards, L. C. Teng, Parametrization of Linear Coupled Motion in Periodic Systems, IEEE Trans. Nucl. Sci. 20 (3) (1973) 885–888.
URL http://ieeexplore.ieee.org/document/4327279/

[49] ELF Corperation, http://www.elf.co.jp/.
URL http://www.elf.co.jp/

[50] C. Mitsuda, et al., Development of the Ceramic Chamber Integrated Pulsed Magnet Fitting for a Narrow Gap, in: Proceedings of the 6th Int. Particle Accelerator Conf., Vol. IPAC2015, 2015.
URL http://jacow.org/ipac2015/doi/JACoW-IPAC2015-WEPMA049.html

[51] C. Mitsuda, Development of the ceramic chamber integrated pulsed-magnet with super narrow bore, Tech. rep. (2016).
URL http://www.jasri.jp/content/files/takumi_report/T27-1.pdf

[52] C. Mitsuda, et al., Newly Development of Ceramics Chamber with Integrated Pulsed Magnet for Super-Narrow Bore in KEK-PF, in: Proceedings of the 12th International Particle Accelerator Conference, Vol. IPAC2021.
URL https://jacow.org/ipac2021/doi/JACoW-IPAC2021-FRXB04.html

[53] Y. Lu, et al., Magnetic Field Measurement and Beam Performance Test of Ceramics Chamber with Integrated Pulsed Magnet at KEK-PF, in: Proceedings of the 12th International Particle Accelerator Conference, Vol. IPAC2021, 2021, pp. 2352–2355.
URL https://jacow.org/ipac2021/doi/JACoW-IPAC2021-TUPAB359.html

[54] C. Mitsuda, et al., Accelerator Implementing Development of Ceramics Chamber with Integrated Pulsed Magnet for Beam Test, in: Proceedings of the 10th Int. Particle Accelerator Conf., 2019.
URL http://jacow.org/ipac2019/doi/JACoW-IPAC2019-THPTS027.html

[55] A. Alexander, Beam Diagnostics and Radiation Detection System, in: KEK-OHO TEXT, 2011.
URL http://accwww2.kek.jp/oho/oho20/F/lecture/20_09_06_Beam_dignostics_Aryshev.pdf

[56] T. Ogitsu, Superconducting Accelerator Magnets, in: KEK-OHO TEXT (Japanese), 2011.
URL http://accwww2.kek.jp/oho/OHO%20text%20archives%202005-2011/OHO11%20web%20final/OHO11%20ogitsu%2020110906.pdf

[57] Poisson Superfish.
URL https://laacg.lanl.gov/laacg/services/download_sf.phtml

[58] Opera Simulation Software.
URL https://www.operafea.com

[59] L. Mauricio, Multipoles, Conformal Mapping, Pole tip design, in: Lecture at U. S. Particle Accelerator School.
URL https://uspas.fnal.gov/materials/16Austin/lecture02.pdf